EXPERIMENTAL INVESTIGATION OF GAS PHASE AND SURFACE PHENOMENA IN A SEEDED PLASMA

Thesis by

Alfred Cyril Pinchak

In Partial Fulfillment of the Requirements

For the Degree of

Doctor of Philosophy

California Institute of Technology

Pasadena, California

1963

ACKNOWLEDGMENTS

The author wishes to express his sincere gratitude to Professor E. E. Zukoski of the California Institute of Technology for his most excellent guidance and ceaseless encouragement during the course of the investigation. Special thanks are also due to Professor J. L. Kerrebrock, now at the Massachusetts Institute of Technology, for his initiation of the project at the California Institute of Technology and his subsequent enlightening discussions concerning the work.

Thanks are also extended to Mr. T. A. Cool for his aid in conducting the experiments and evaluating the results. Mr. F. T. Linton is thanked for his drawings of the figures as well as for the fabrication of most of the test equipment and aid in obtaining the experimental data.

The author also wishes to thank Mrs. Roberta Duffy and Mrs. Madeline Fagergren for their efforts related to the preparation of the manuscript.

Acknowledgment is also rendered to the Bendix Corporation, Union Carbide Corporation, and the Garrett Corporation for their financial assistance to the author in the form of fellowships.

ABSTRACT

This thesis deals with some recent experiments conducted with low-temperature seeded plasmas at atmospheric pressure. A simple arc jet was utilized to heat a steady flow of argon gas which was subsequently mixed with a small amount of potassium vapor. The resulting mixture was then channeled through a suitable electrode configuration.

Results of the experiments indicated two modes of steady, stable current conduction between the electrodes. The data indicated that thermionic emission was sufficient to provide the observed currents during both modes of operation. In the first, or normal, mode, the effect of gas phase phenomena predominated in fixing the current.

Under certain conditions, a transition to a second mode of operation occurred. In this mode, the current was found to be thermionically limited, and thus was determined solely by electrode surface effects. A quantitative comparison between the observed voltage-current characteristics and two current conduction theories is presented.

The aforementioned comparison, along with a quantitative examination of the experimentally observed elevated electron temperatures, indicated that both Joule heating and some non-equilibrium process must be considered in order to obtain a satisfactory understanding of the current conduction phenomena.

Electrode heat transfer was studied by observing variation of the electrode temperatures with magnitude and polarity of the current. Analysis of the data indicated that an important heat transfer mechanism was the penetration of the surface work function barrier as electrons entered or left the surface.

SUMMARY

This thesis describes and discusses some experiments conducted with low-temperature, seeded plasmas. The objectives of these experiments were: (1) the study of the mechanism of current conduction in seeded plasmas; (2) the investigation of electrode surface phenomena in the presence of the aforementioned plasmas; and (3) the determination of the effect of current conduction on the electrode heat transfer rates.

A simple arc jet was utilized to heat a main flow of argon gas. This main flow was mixed with a small, secondary flow of argon which had been passed through a potassium boiler, and thus contained a known concentration of potassium. After the mixed flow passed through an "equilibration" chamber, the resulting seeded plasma was ducted through an appropriate electrode test section.

At the entrance to the test section, the plasma pressure was maintained at one atmosphere, with a total mass flow of approximately 2.5 grams/sec. The plasma temperature was varied between 1400°K and 2500°K, and the potassium seed concentration was set between the limits 0 - 1.3 mole per cent, which produced an electron density on the order of 10^{14} per cm^3 under normal operating conditions.

A coaxial electrode configuration was employed in most of the experiments to insure that the current conduction occurred through the plasma rather than along spurious shorting paths which may be developed on the insulator surfaces of other electrode geometries. Two other electrode systems were also utilized in some of the tests; they were designated by geometry as "double wire" and "axial" test sections. The characteristic axial and radial dimensions of the electrode test section were on the order of one centimeter. During the course of the

experiments, data were taken to determine the following quantities: gas enthalpy, potassium seed fraction, electrode voltage, current, and temperature.

Results of the experiments indicated two modes of steady, stable current conduction. In the first or "normal" mode, the effect of gas phase phenomena predominated in the determination of the current magnitude. Under certain conditions, a transition to a second mode of operation occurred. The experimental data indicated that electron emission from the cathode was by the thermionic process in both modes of operation. In the second mode, the current was found to be thermionically limited, and thus was determined solely by electrode surface effects.

With operation in the normal mode, a voltage - current characteristic was obtained in which dv/di steadily decreased with increasing current until a small limiting value was reached. The effects observed when the electrode surface area and the potassium seed concentration were changed, and the fact that values of the measured and theoretical conductivity agree approximately for small currents, indicate that the voltage - current characteristics of the normal mode are dominated by gas phase phenomena.

Two theories were considered with the purpose of explaining the curvature of these voltage - current characteristics. The first theory assumes the conductivity to be a function of the local gas temperature, and thus attributes the varying slope of the V-I curve to ordinary Joule heating. The second theory is that of non-equilibrium conduction (due to Kerrebrock). In this theory, the conductivity is a function of the current density, and this is purported to be the dominant factor in

determining the V-I characteristic. A quantitative comparison between the two theories and the experimental results indicates that both Joule heating and some non-equilibrium process must be taken into account to explain the high conductivity values and the elevated electron temperature which were observed.

During the transition from the normal mode to the current limited mode, a decrease in the current and an increase in the electrode voltage were always observed. A physical mechanism for this transition is proposed and discussed. One of the basic assumptions is that the maximum normal mode current obtained just prior to transition is the thermionically emitted current. Any additional increase in the electrode voltage then appears as an increased potential drop across the cathode sheath. The emitted electrons are accelerated by the sheath potential and then thermalized near the cathode surface by collisions with gas atoms. Heat transfer from the thermalization region back to the electrode produces an increase in the electrode temperature. The increase in electrode temperature produces a decrease in the fractional coverage of adsorbed potassium atoms on the electrode surface, and this in turn causes the large decrease in current observed at transition. The variation of normal mode current at transition with seed fraction and electrode surface area was found to be in agreement with previous work on electron emission from metals with surface adsorption of alkali metals.

In the second mode of current conduction, the V-I curve had a vertical slope, indicating a thermionically limited current. The magnitude of the current in this mode indicated that the electrode surface was still appreciably coated with potassium. As was expected, increas-

ing the seed fraction in this case produced an increase in the thermionically limited current, and a simple experiment in which the electrode surface area was decreased produced a linearly proportional decrease in the total current.

Electrode heat transfer was studied by observing variation of the electrode temperatures with magnitude and polarity of the current. With electrons being emitted from the center electrode, the electrode temperature tended to steadily decrease with increasing current (normal mode conduction). With the polarity reversed, the electrode temperature rapidly increased with the current. With the test section of these experiments, the cooling was chiefly by radiation, and thus a comparatively small change in electrode temperature was indicative of a large change in electrode heat transfer. Analyses of the data indicated that an important heat transfer mechanism was the penetration of the surface work function barrier as electrons entered or left the surface. This effect was sufficient to cool the electrode in the case mentioned above, even though Joule heating in the boundary layer, free stream, and in the electrode itself all were contributing toward raising the electrode temperature.

TABLE OF CONTENTS

I. INTRODUCTION

In recent years, a number of devices have been proposed which utilize the interaction of electromagnetic forces with an ionized gas. A number of these devices are concerned with one of two problems: (1) acceleration of the gas with a view to producing a propulsive thrust, and (2) the direct conversion of thermal energy to an electrical form. One of the chief applications of these devices is in the realm of interplanetary space missions. The simplest procedure suggests a system with two electrodes between which an electric field is applied. Perpendicular to the electric field, a magnetic field is set up and the fluid is subjected to a body force in the direction of $\vec{E} \times \vec{B}$. Depending upon the relative directions of the flow velocity and $\vec{E} \times \vec{B}$, this device may act either as an accelerator or as an electrical generator. Both of the aforementioned applications require that the final apparatus be capable of operating for long periods of time, such as several months, or even several years.

In order that either of these devices operate efficiently, it is necessary that the gas have a high electrical conductivity. Since the gases proposed for use in such devices are usually products of combustion (of hydrocarbon air mixtures) or noble gases, it is evident that very high working temperatures are necessary to insure the degree of ionization required to achieve a high conductivity. Such high temperatures are often incompatible with the long operational lifetimes also required. Thus, the fabricating materials impose an upper limit to the operating temperatures of the proposed accelerators and/or generators.

In order to reduce the gas temperature and yet maintain an adequate electrical conductivity, the gas is often "seeded" by injecting a small amount of some material such as cesium or potassium. Such materials ionize readily at relatively low temperatures, and thus can be used to give high conductivity at temperatures as low as 2000°K. However, in addition to changing the properties of the bulk of the gas, conditions at the electrode surfaces are also affected since these materials tend to coat the electrodes.

A large number of factors, both at the electrode surface and in the bulk of the gas, interact simultaneously to complicate any analyses of such devices. The presence of potassium in the gas causes a certain fraction of the electrode surface to become coated with potassium. This usually has the favorable effect of increasing the electron emission from the surface. In addition, the ions produced at the surface, along with the ions in the free stream, partially neutralize negative space charges, which results in larger electrode currents.

In view of the complexity of the general problem, a series of experiments were conducted to study various surface and gas-phase processes which have important influences on the performance of generators or accelerators using a seeded plasma as the working fluid. The problems investigated include current conduction through the plasma proper, several surface phenomena associated with the adsorption of potassium on the electrodes, the emission of currents from hot electrodes, and heat transfer rates to the electrodes. The chief difficulty which arose here was the process of properly interpreting the data and sorting out the various effects by viewing the behavior of several readily-measured experimental quantities.

II. EXPERIMENTAL METHOD OF INVESTIGATION

A simple, steady-state experiment was set up to study some of the aforementioned effects associated with current conduction and surface phenomena in a seeded plasma. The plasma used was composed of a mixture of argon gas and potassium vapor, and in order to simplify the experiments, no magnetic field was applied.

The plasma ranged in temperature from approximately 1200°K to 2700°K with a total static pressure of one atmosphere in all cases. Values of the seed concentration, n_k/n_a, ranged between zero and 1.2×10^{-2}, and thus, under typical operating conditions the electron density was on the order of 10^{14} electrons/cm^3.

A conventional arc jet was used to heat argon, and potassium seed material was injected by passing a small flow of argon through a bath of liquid potassium and mixing this with the main, heated argon stream. This mixture then passed through a chamber in which the flow equilibrated to a more or less uniform, homogeneous fluid. Finally, the resulting "seeded plasma" passed through an appropriate test section. A schematic diagram of the apparatus is depicted in Fig. 1, and a detailed description is given in Appendix E.

Figures 2, 3, and 4 show several of the test sections which were employed in these experiments. At first, a rectangular geometry similar to that of Ref. 1 was employed. This configuration consisted of two rectangular electrodes with insulating side walls. However, the potassium was able to diffuse into the various thin joining cracks and apparently into the insulating side walls, and thus produced shorting paths for the current. In order to avoid this difficulty, the coaxial

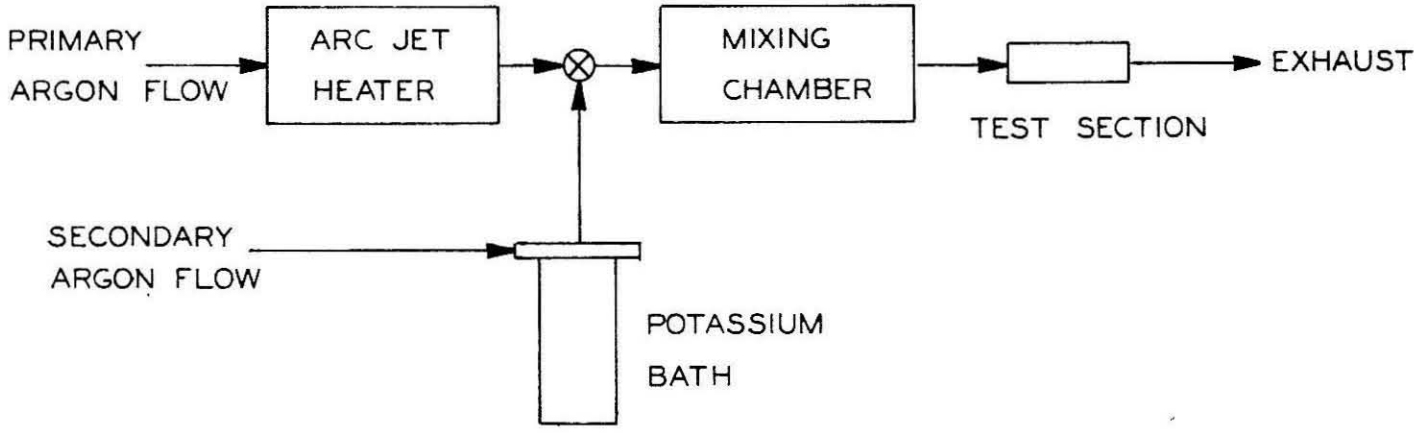

Figure 1. Schematic Diagram of the Experimental Apparatus.

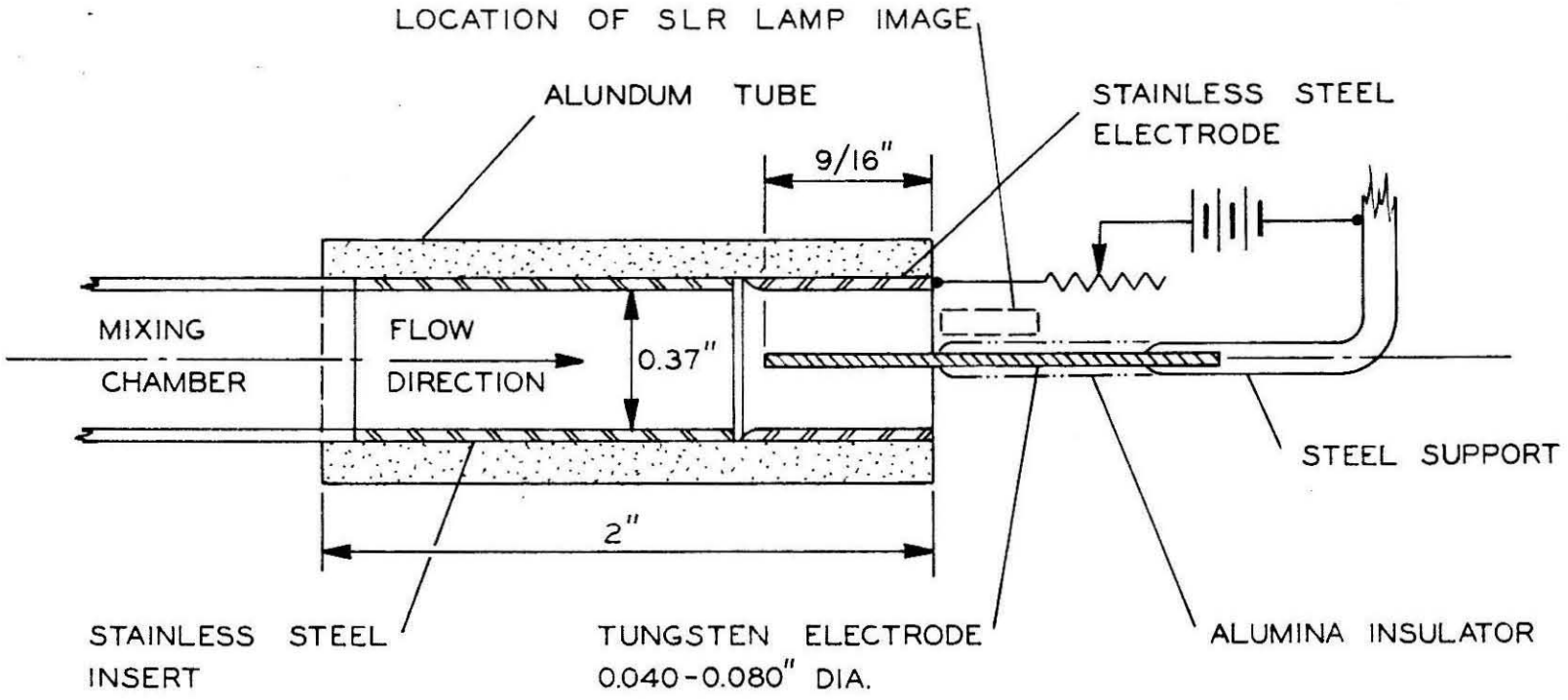

Figure 2. Coaxial Electrode Test Section.

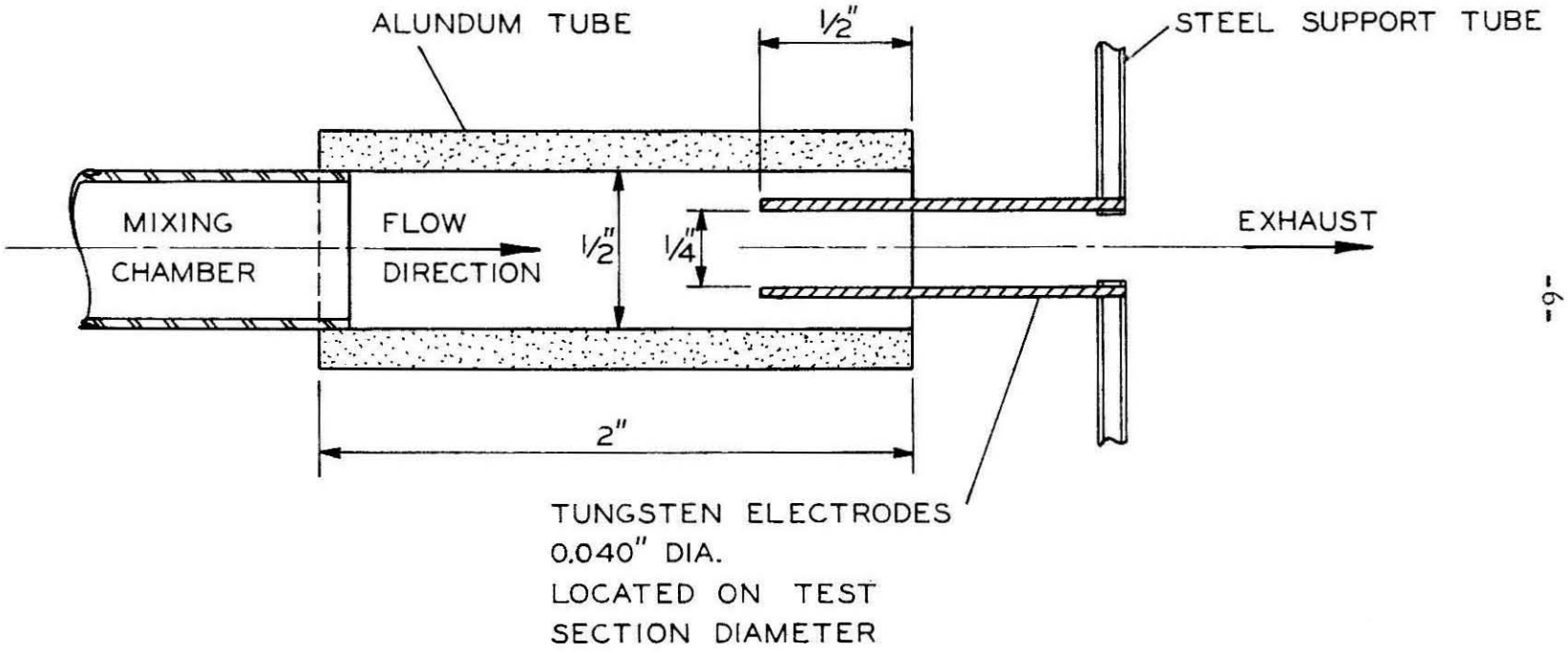

Figure 3. Double Wire Electrode Test Section.

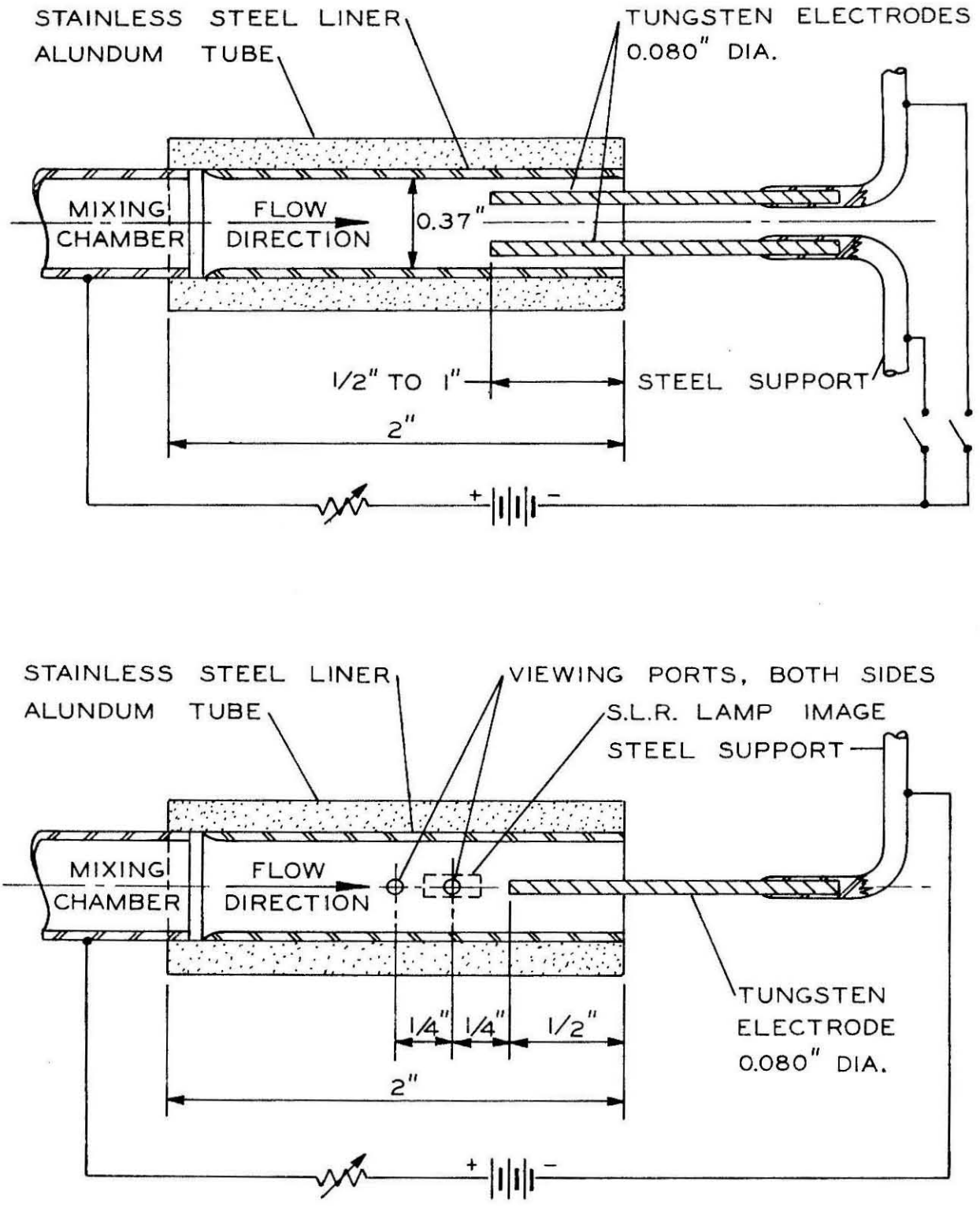

Figure 4. Axial Geometry Test Section.

electrode geometry illustrated in Fig. 2 was devised. In this configuration, the current must pass through the plasma, and thus it is assured that the observed conduction is through the gas rather than through some combination of gas conduction and shorting paths. This electrode configuration was used in most of the tests , and unless otherwise stated, this is the type of test section geometry which is under consideration. The "double wire" set-up (Fig. 3) was utilized to give a considerably different conduction geometry and thus provide some insight in separating the surface phenomena from effects in the bulk of the gas. Finally, the "axial" flow geometry (Fig. 4) provided a geometry in which the current paths were parallel to the gas flow velocity. Such a situation proves more amenable to mathematical analysis. Utilization of twin cathodes in the axial geometry with individual switching provided some very simple, yet very effective, methods for separating surface phenomena from gas phase phenomena.

A special argon heating system was installed for use with conductivity maxima experiments. The total secondary argon flow which ordinarily passed through the potassium pot was divided into two parts. Depending upon the amount of seeding material desired, a given flow rate of argon was directed through the pot. The remainder of the argon was passed through a heating coil which was maintained at the same temperature as the potassium pot. This method permitted a fixed value for the secondary argon flow independent of the seed concentration and this resulted in a constant plasma temperature at the mixer exit.

The physical measurements which were obtained during the test runs included the following: voltage and current passing through the

arc jet, temperature rise in the arc-jet cooling water, argon flow rates, test section voltage, current and electrode temperatures. Table I lists the magnitudes of some of the operating parameters of the complete system.

TABLE I

Arc Jet and Test Section Operating Conditions

Parameter	Arc Jet	Test Section'
Main argon flow rate	2.23 g/sec	2.23 g/sec
Potassium pot argon flow rate	-	0 - 0.5 g/sec
Potassium flow rate	-	0 - 0.03 g/sec
Voltage	60 - 90 volts	0 - $\pm$ 24 volts
Current	30 - 120 amps	0 - $\pm$ 50 amps
Arc power	2.7 - 8.0 kw	-
Mean argon temperature	1200 - 2700°K	1200 - 2700°K
Argon pressure	1 atm	1 atm
Potassium pressure	-	0 - .013 atm
Potassium pot temperature	-	475 - 520°C
Mean flow velocity	O* (400 fps)	O (400 fps)
Mach number	O (0.1)	O (0.1)
Wall temperature	330 - 700°C	750 - 1100°C
Electrode temperature	-	1000 - 2500°C
Mean flow stay time	O (1.2×10^{-3} sec)	O (10^{-4} sec)
Electron-electron equilibration time	O (10^{-10} sec)	O (10^{-10} sec)

(continued)

Electron-neutral equilibration time	O (10^{-6} sec)	O (10^{-6} sec)
Electrode drift time (electrons)	-	10^{-6} sec
Viscous Reynolds number (L ≅ 1 cm)	-	O (10^{4})

* "O" implies "on the order of".

III. EXPERIMENTAL RESULTS

A complete selection of typical experimental results is compiled in this section for ease of reference and to provide an overall picture of the various phenomena observed during the investigation. The data will be presented here unaccompanied by any attempt at explanation, and discussion of the implications of these results will follow in subsequent sections.

A. General Characteristics of the Observed Phenomena

Figures 5, 6, 7, and 8 show typical voltage-current data obtained from the coaxial, double wire, and axial geometries as indicated on the graphs. Two different modes of operation were found to exist for steady current conduction and are indicated in these figures. As indicated in Fig. 5, these two modes will be referred to as the normal mode and the current limited mode. An unstable transition phenomenon was found to occur temporarily when the test section passed from one mode of operation to the other.

In the normal mode, the current is a monotonic function of the applied voltage. As the applied voltage is increased, the current increases slowly at first and then more rapidly as larger voltages are reached. At high currents, the V-I curves have rather small slopes, and in some cases are almost flat (see Fig. 5). With the center electrode operating as the anode (reversed polarity), the curves have the same general features, and the shapes of the positive and negative branches of the V-I characteristic are quite similar. Transition to the second mode of operation produces a condition in which the current is substantially independent of the applied voltage.

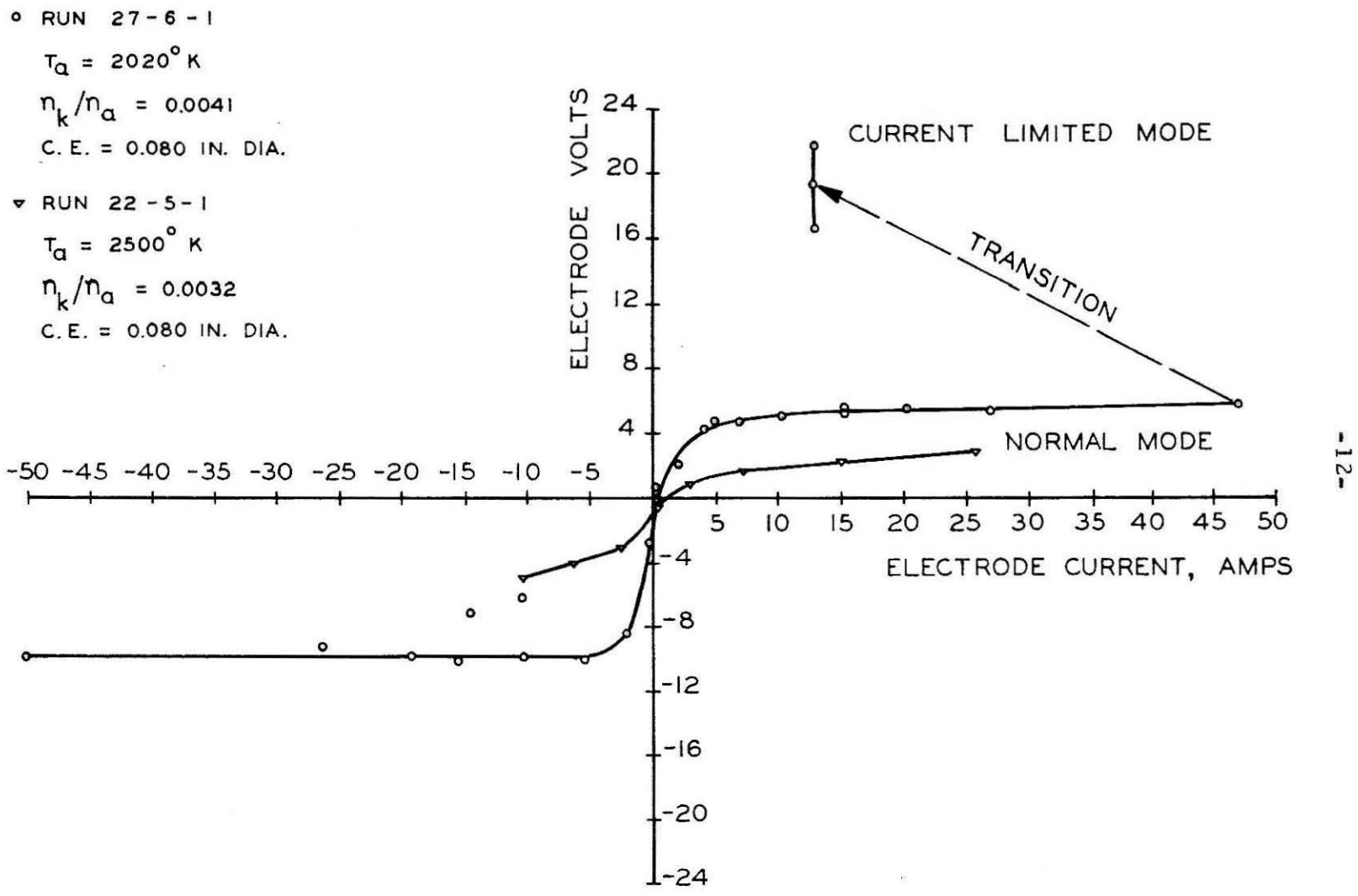

Figure 5. Voltage-Current Characteristics (Coaxial Geometry).

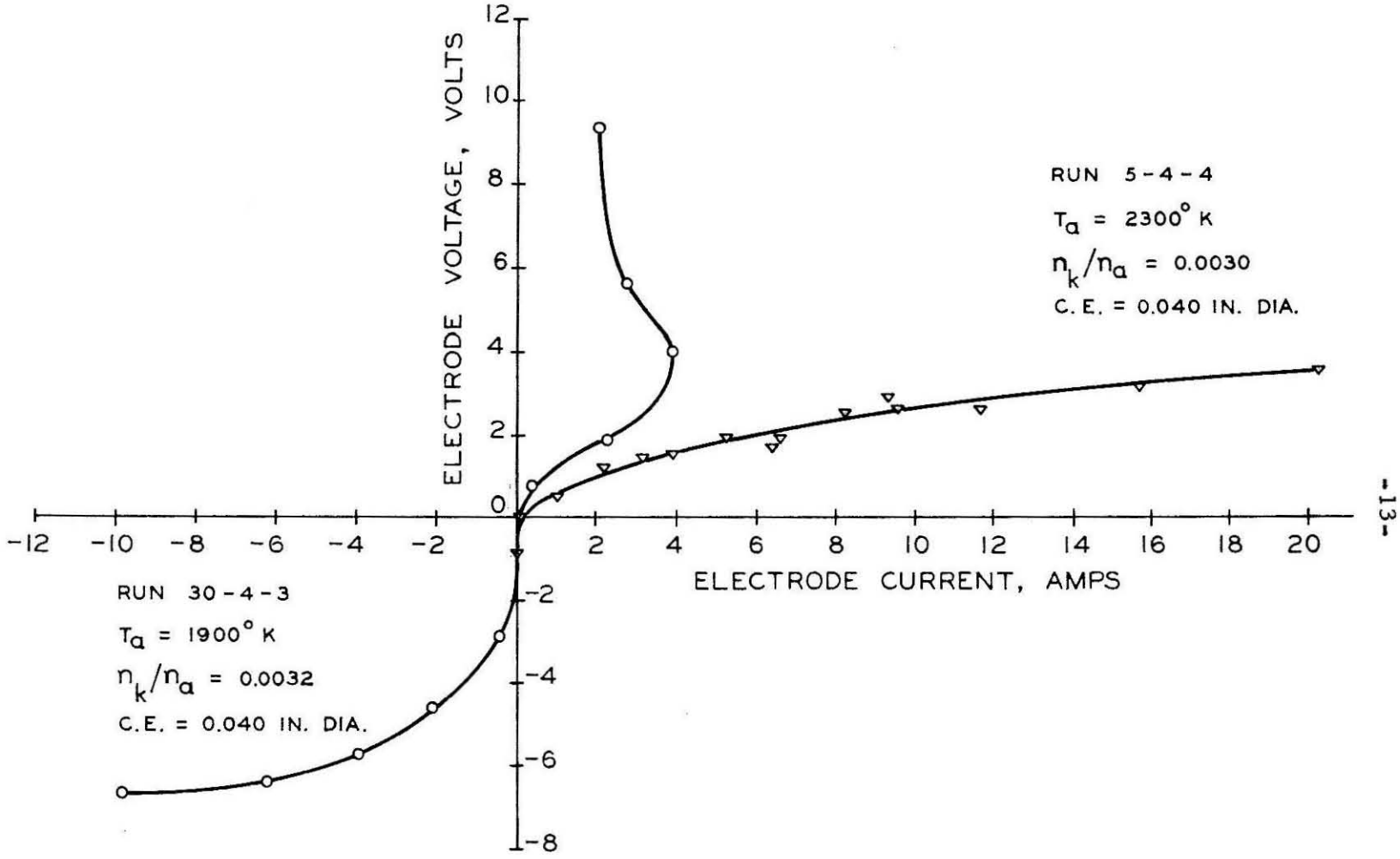

Figure 6. Voltage-Current Characteristics (Coaxial Geometry).

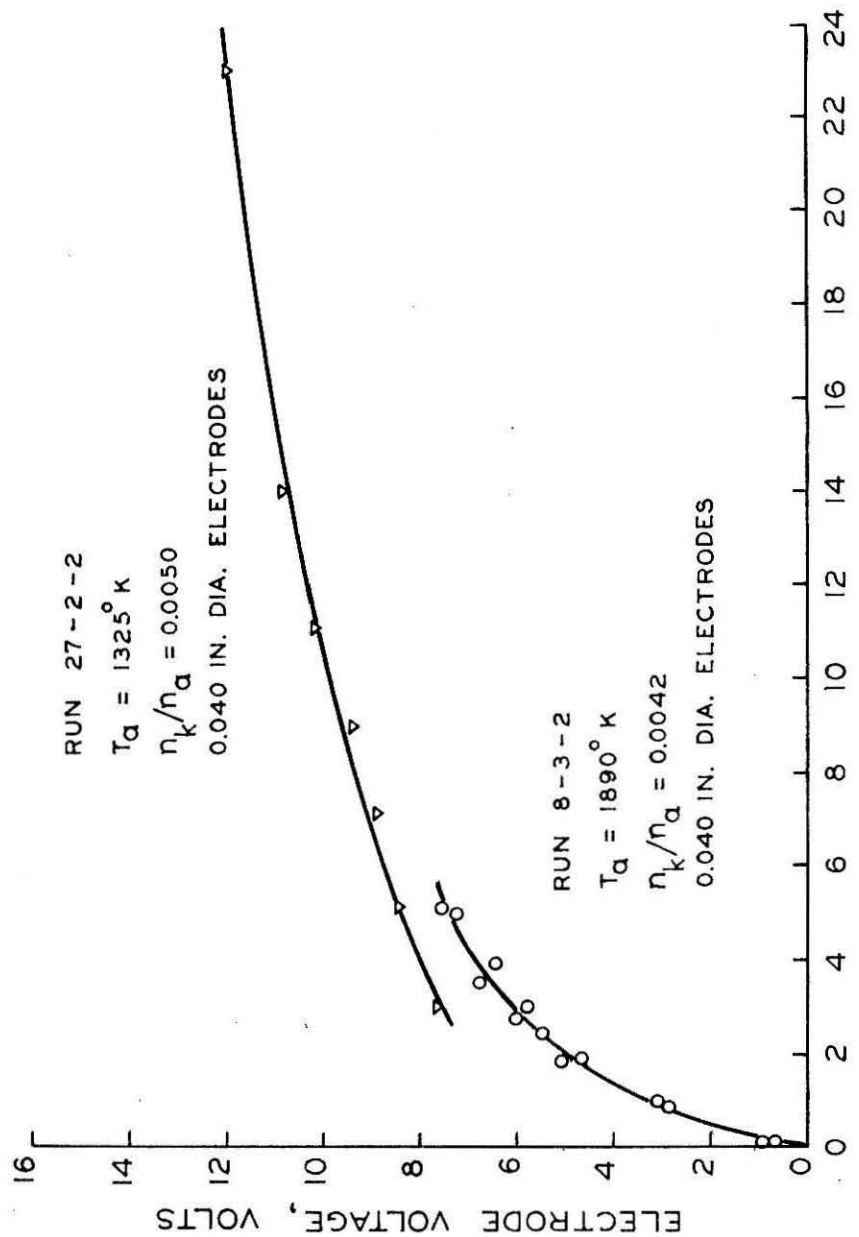

Figure 7. Voltage-Current Characteristics (Double Wire Geometry).

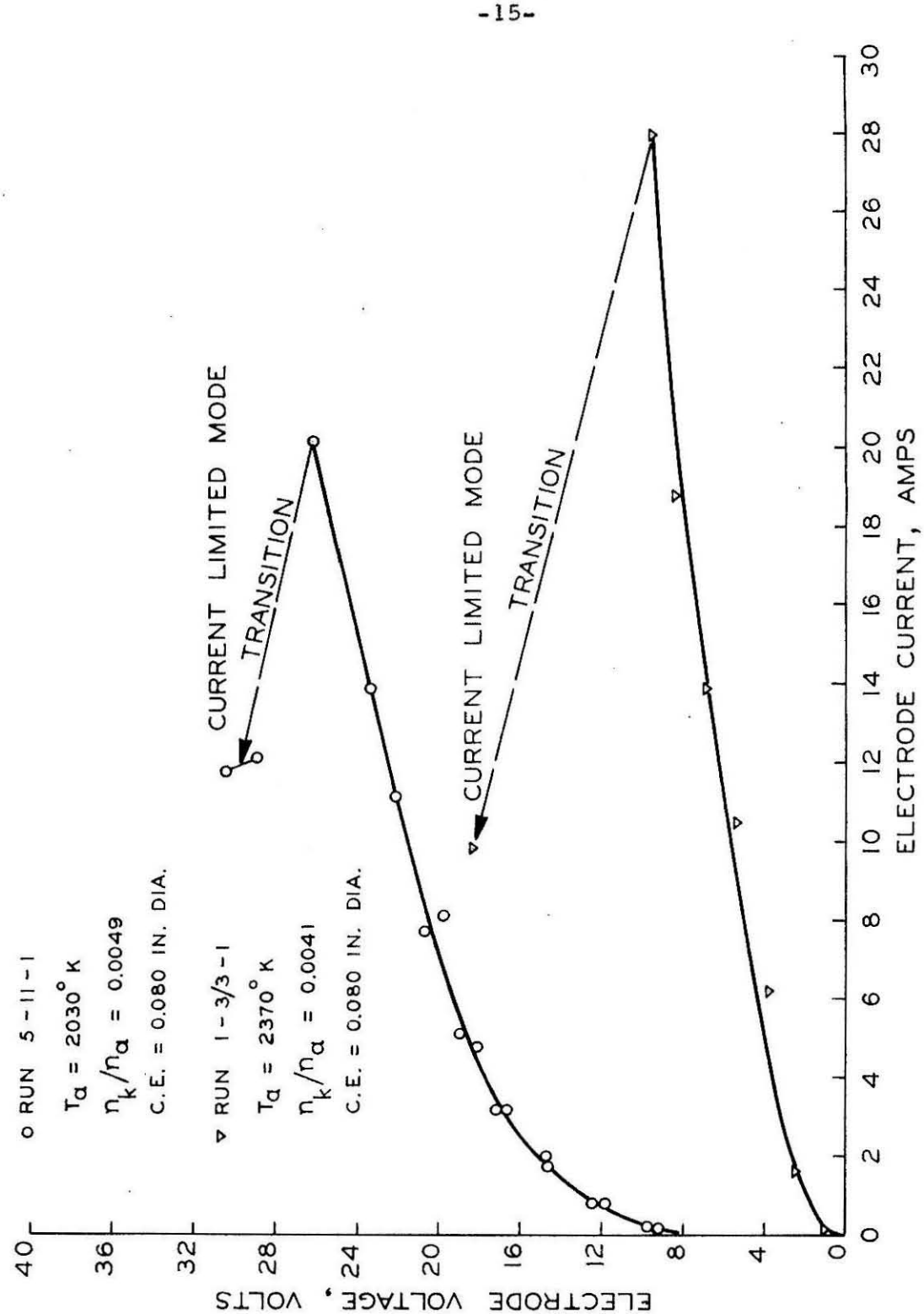

Figure 8. Voltage-Current Characteristic (Axial Geometry).

Figures 9 and 10 indicate the change in center electrode temperature for both the normal mode and the current limited mode. With positive voltages the center electrode temperature decreases slightly with increasing current, and then may increase again as the maximum normal mode current is reached. Upon transition to the current limited mode, the electrode temperature increases by a large amount (up to 700°C in some cases). With reversed polarity, the electrode temperature continuously increases with increasing current. At sufficiently high reversed currents, the wire temperature may even exceed the initial bulk temperature of the gas.

In the following presentation, the details of the experimental results will be considered separately for the two aforementioned modes of operation. Before proceeding to these considerations, brief mention will be made of some qualitative visual observations made during normal and abnormal operating conditions.

Visual observation of the normal mode revealed a reddish glow in the region of expected current conduction through the plasma. As the current was increased, the intensity of this glow also increased. However, as transition occurred, the glow suddenly vanished. In the current limited mode, the glow was not observed for any values of the voltage and/or current.

On a number of occasions, during the transition process, a layer of surface material (presumably adsorbed potassium) was seen to "peel off" in a spiral fashion beginning at the leading tip of the electrode and continuing in the downstream direction. (The arc jet heater provides a large initial swirl velocity to the flow which may be sustained through the mixing chamber and test sections.)

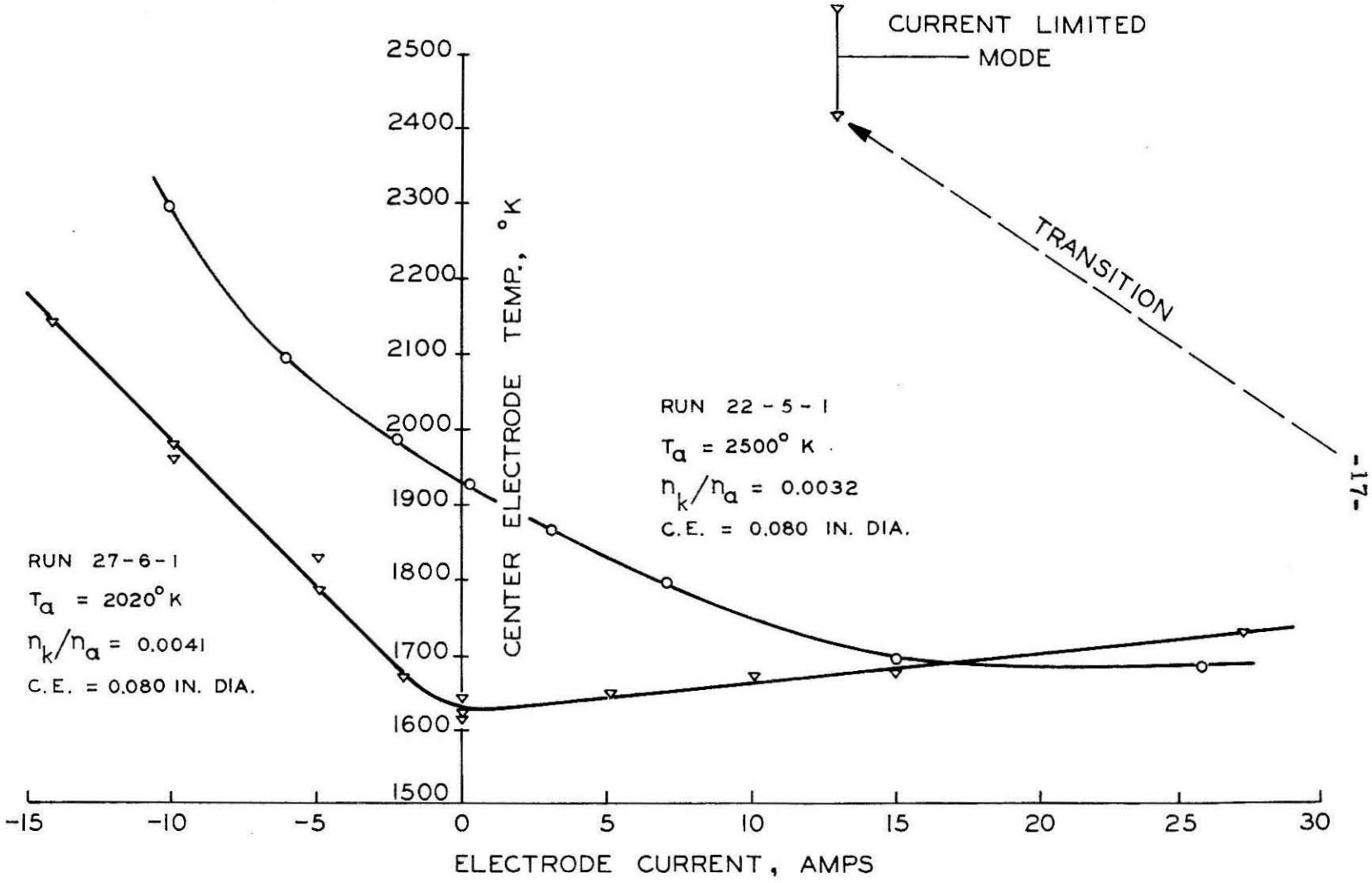

Figure 9. Center Electrode Temperature Versus Electrode Current (Coaxial Geometry).

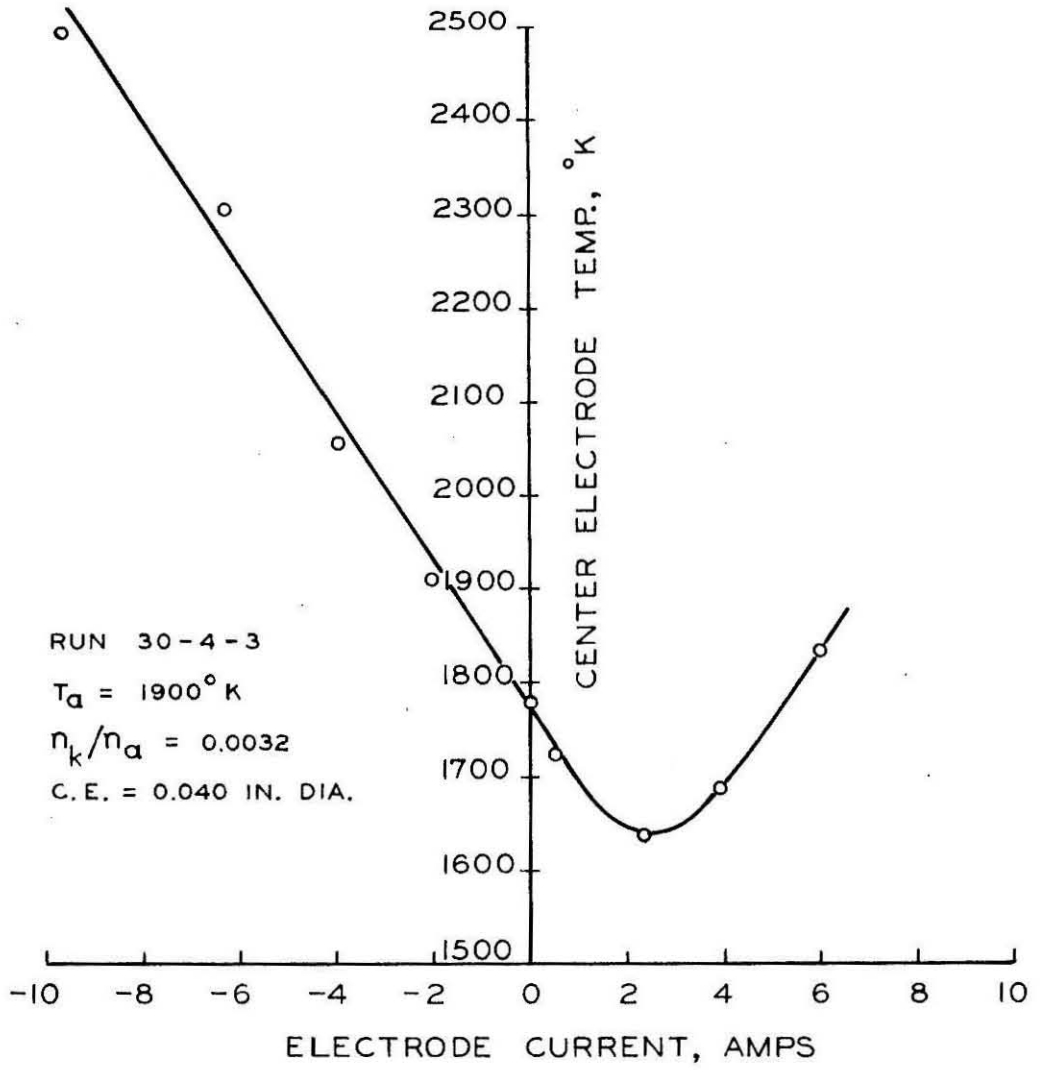

Figure 10. Center Electrode Temperature Versus Electrode Current (Coaxial Geometry).

The aforementioned visual observations occurred under normal test conditions. Data from such runs was reduced and evaluated. The following comments refer to test runs which were considered abnormal. Data taken under such conditions was not reproducible and thus was discarded.

When either electrode was operated at sufficiently low temperatures, an arc formed across the boundary layer. This arc formation occurred more often on the cathode than on the anode. The arc terminated a short distance from the electrode surface, and the conduction through the bulk of the gas appeared to be similar to normal operating conditions.

Another phenomenon similar to the arc formation in the boundary layer was also observed. At low currents, several small bright spots appeared on the cathode. Each spot was surrounded by a local reddish glow, and this gave the impression that the current was being conducted chiefly from these local spots (approximately 0.05 inches in diameter). As the current was increased, the size of these bright spots increased and eventually merged to completely cover the surface. Very erratic voltage-current data was taken when the "bright spot" phenomenon occurred.

Yet another strange effect was observed on several occasions. Under certain conditions, the electrode was found to be comparatively cool up to the downstream edge of the test section. At this position, the electrode temperature suddenly increased, and the electrode was surrounded by a very thin band (1/8 inch long) of bright gas. The reddish glow emanating from the band indicated that most of the current

was being emitted from the region of the cathode directly under the aforementioned "bright band".

B. Normal Mode Phenomena

Under normal mode operation, the external resistance of the electric circuit was varied, and the resulting test section voltages and currents were recorded. It was found that the electrode voltage changed from zero to about $\pm$ 6 - 16 volts while the current ranged upward from zero to $\pm$ 50 amps.

Due to the current limitations of the external circuitry, currents larger than 30 amps were allowed to flow for periods no longer than several seconds. The maximum currents obtained with .080" diameter center electrodes resulted in maximum current densities of approximately 80 amp/cm^2. However, with an electrode .020" in diameter, it was possible to obtain maximum current densities in excess of 230 amp/cm^2.

The recorded measurements of the electrode voltage and current indicated mean values upon which small random signals were superimposed. In almost all runs the maximum amplitude of the random component was only a few percent of the mean value. Data from test runs having larger fluctuations were not reduced.

1. Effect of gas temperature. - Figure 11 indicates the effect of varying the bulk gas temperature on the observed voltage-current characteristics. It is noted that the curves possess the same general features for the different gas temperatures. However, the curves are displaced upward by reducing the plasma temperature and are simultaneously changed slightly in shape. A stronger bend in the character-

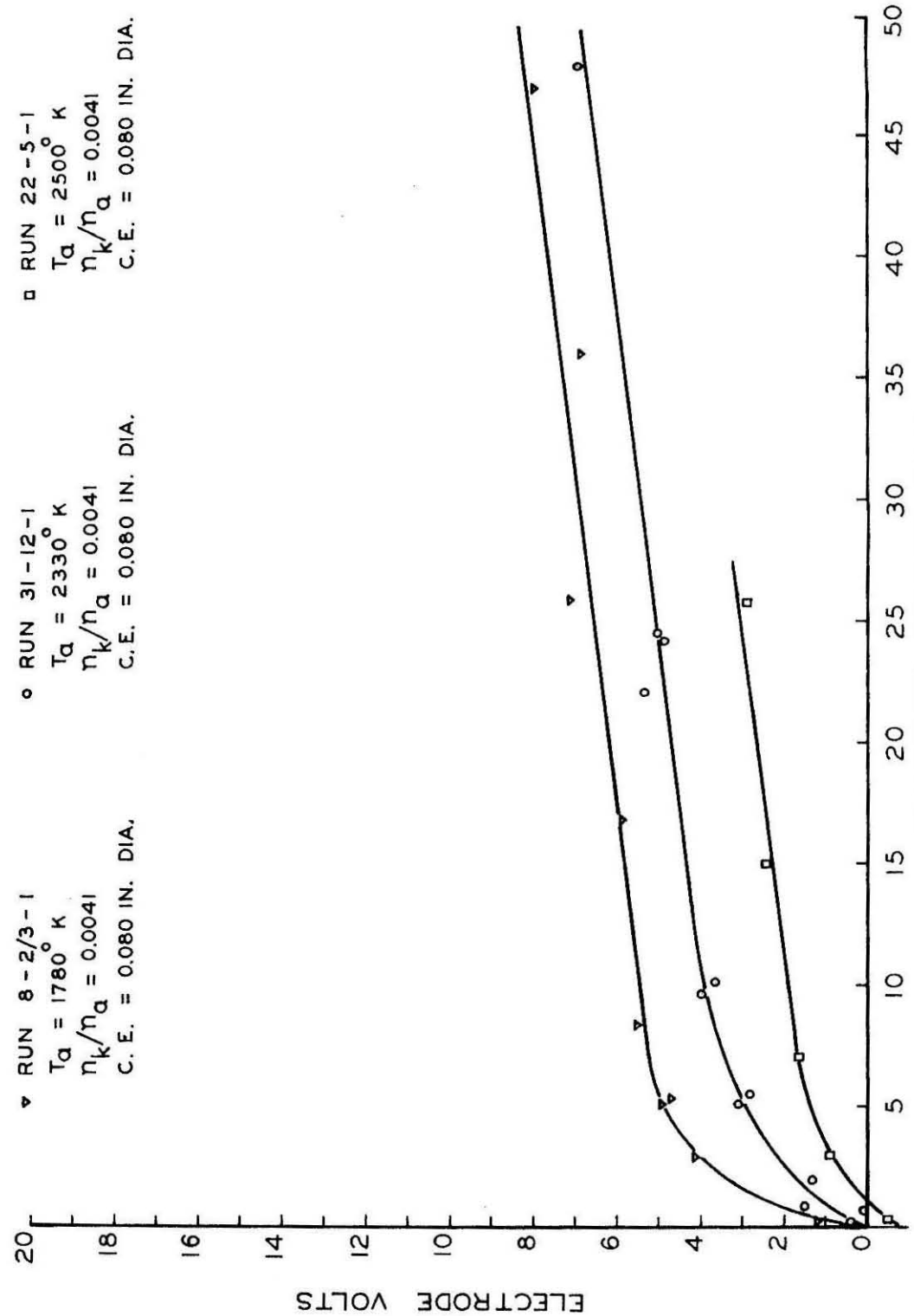

Figure 11. Voltage-Current Characteristics (Coaxial Geometry).

istic results again as the temperature is reduced.

The effect of varying gas temperature on the electrode temperature measurements is shown in Fig. 12. Data is shown only for the positive polarity case in which the center electrode serves as the cathode. It is noted that the curves are not only displaced as expected, but are also radically changed in shape as the gas temperature changes.

2. Seed concentration tests. - Figures 13, 14, and 15 show the results of varying the seed concentration for the coaxial, double wire, and axial geometries, respectively. It is interesting to note that the three geometries give essentially the same result (within the experimental scatter) for the optimum value of n_k/n_a (~ 0.003). Changing the inner electrode diameter from .040" to .080" did not affect the location of the resistance minimum in any regular way.

With the coaxial geometry, the shape of the resistance curve is much less curved for the case of the center electrode being positive. However, the location of the minima is not noticeably affected.

A special by-pass flow system was installed in which the gas temperature of the argon was maintained at a constant value while the mole ratio n_k/n_a was varied (see Appendix E). Figure 16 shows that the conductivity maxima observed with this constant temperature set-up is in agreement with the results of the aforementioned experiments. As expected, the shape of the curve for n_k/n_a greater than the optimum value is less strongly dependent upon n_k/n_a .

In all, there were sixteen tests performed at temperatures ranging from 1200°K to 2500°K with the purpose of finding the optimum seed concentration. The average value of all tests was $n_k/n_a = 0.0032$, with a variation from 0.002 to 0.0049.

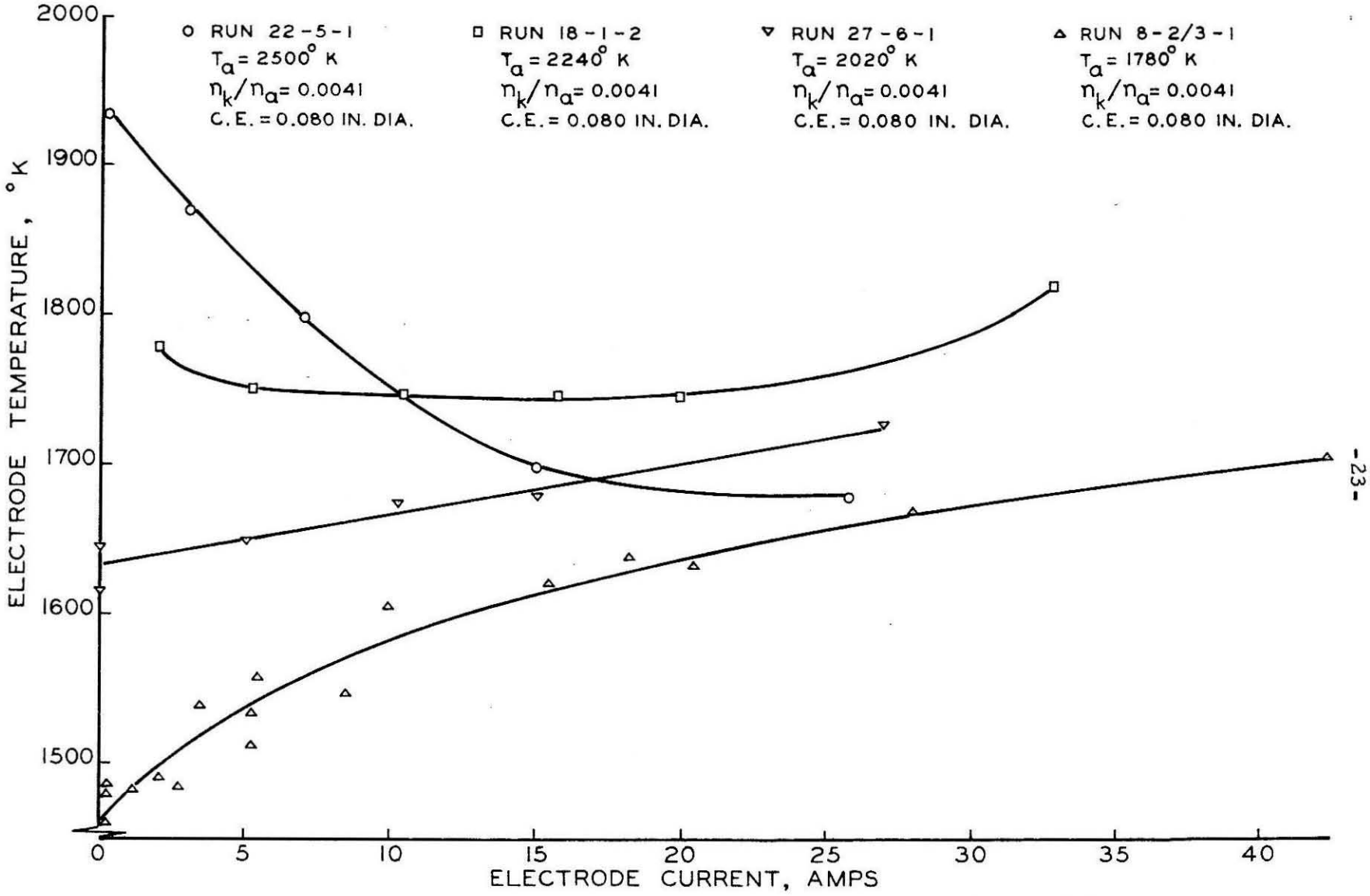

Figure 12. Center Electrode Temperature Versus Electrode Current (Coaxial Geometry).

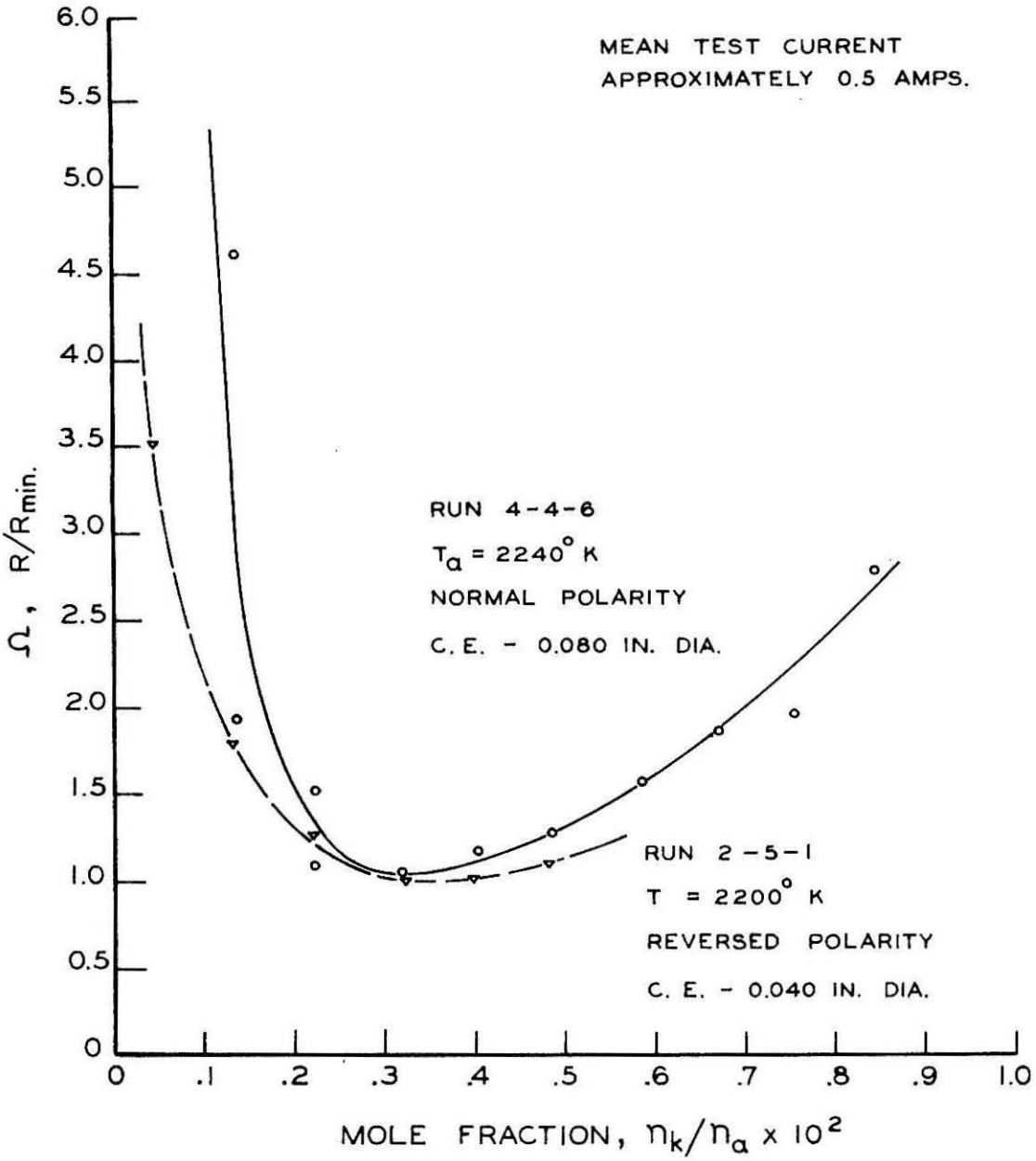

Figure 13. Non-Dimensional Resistance Versus Potassium Seed Fraction (Coaxial Geometry).

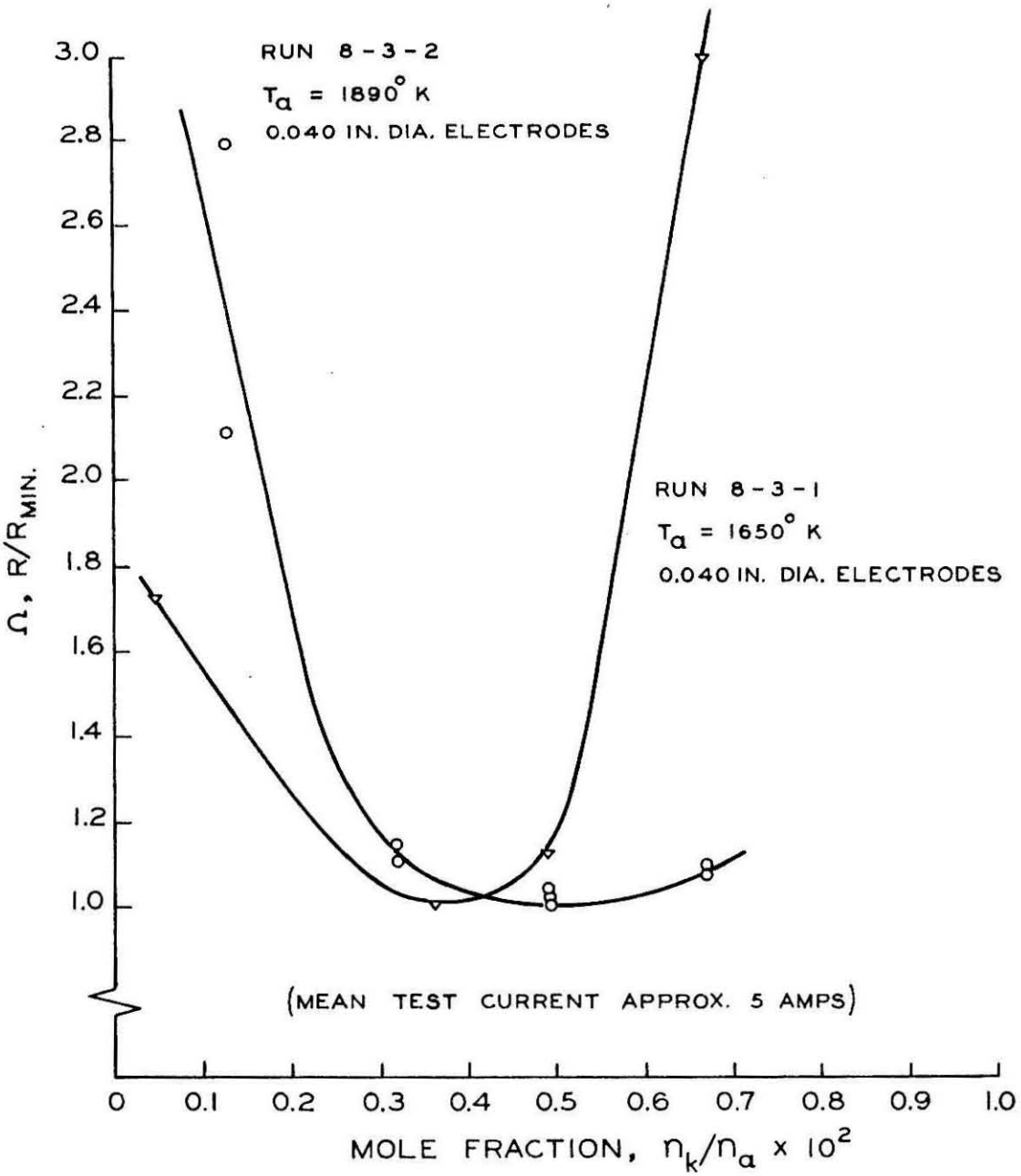

Figure 14. Non-Dimensional Resistance Versus Potassium Seed Fraction (Double Wire Geometry).

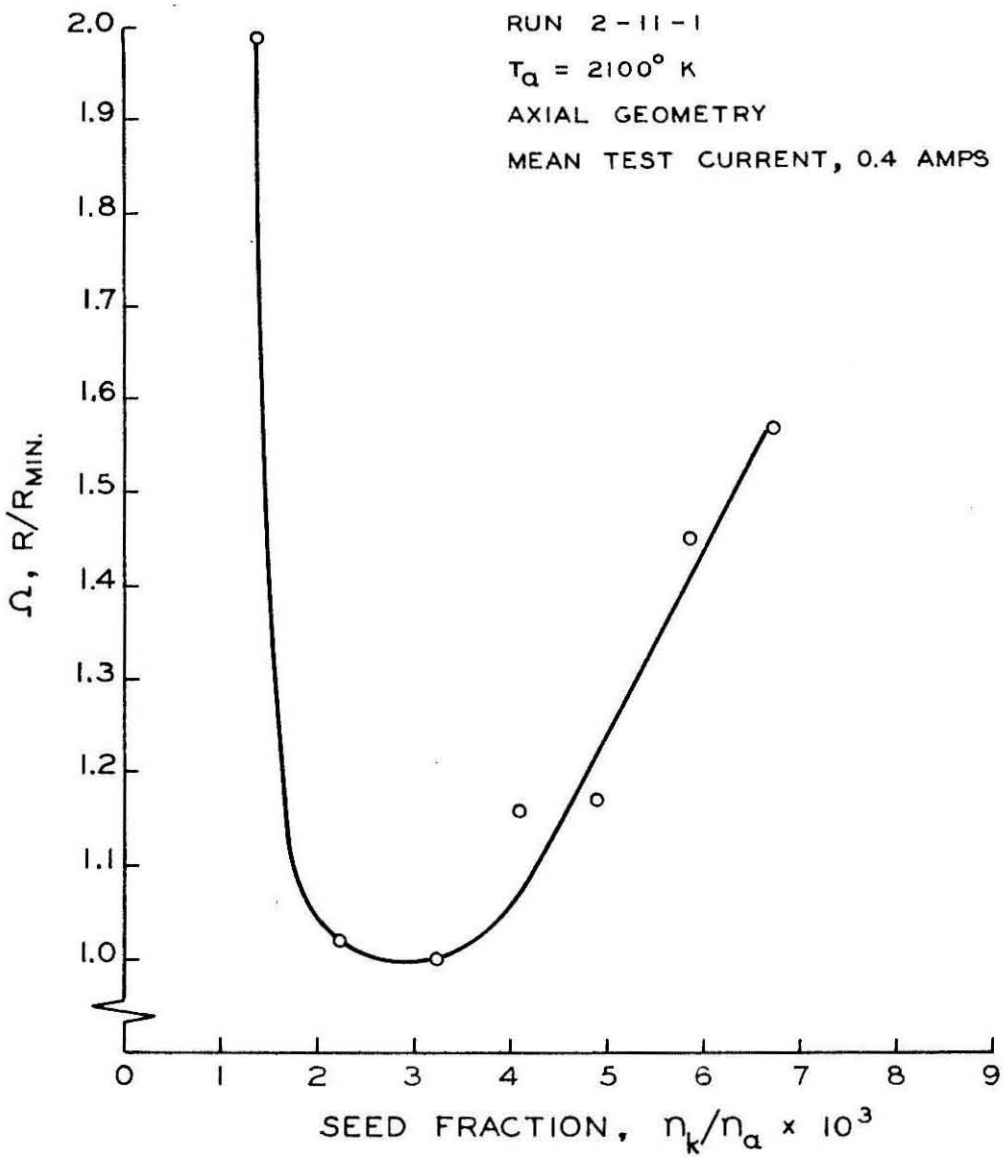

Figure 15. Non-Dimensional Resistance Versus Potassium Seed Fraction (Axial Geometry).

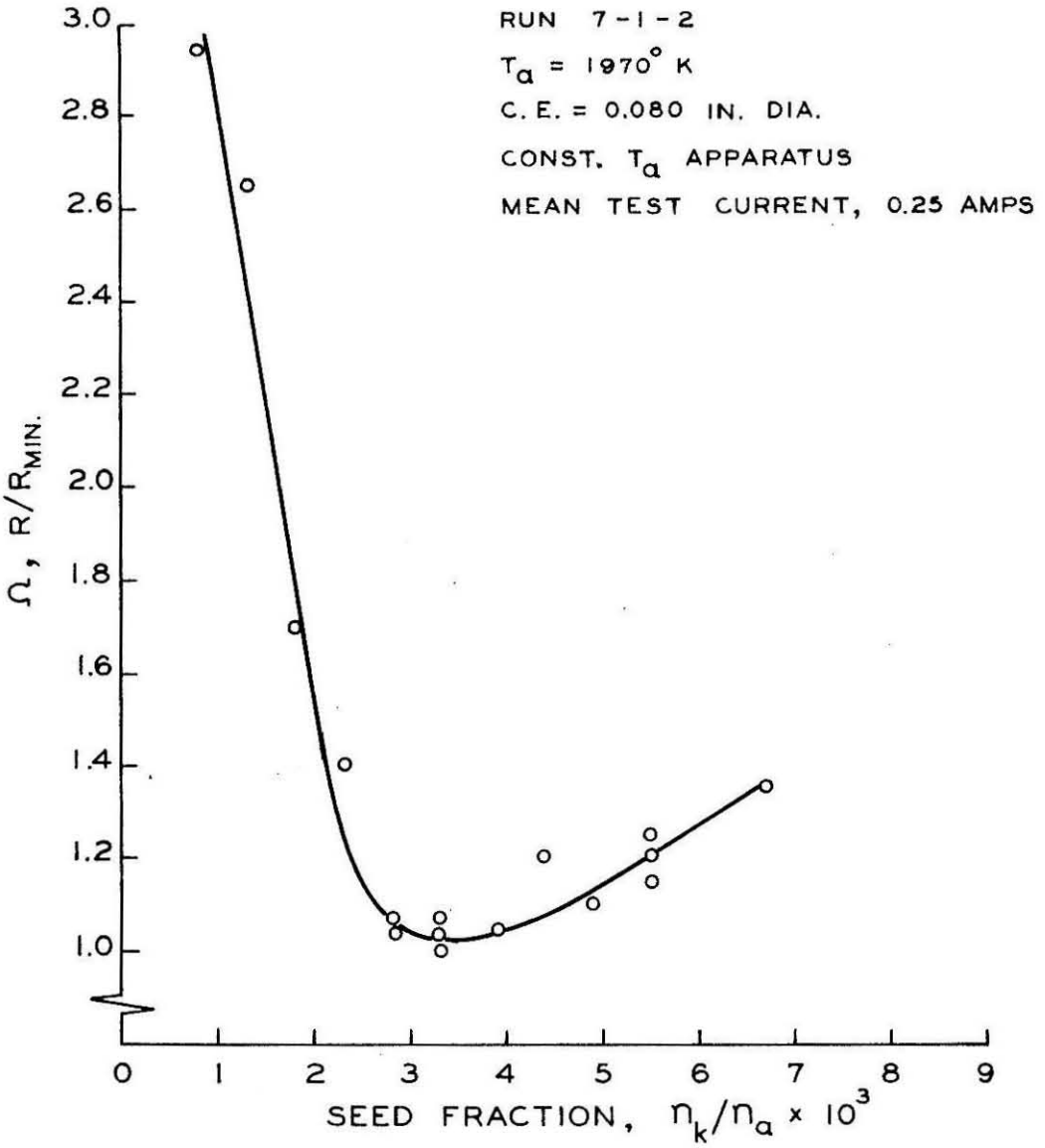

Figure 16. Non-Dimensional Resistance Versus Potassium Seed Fraction (Coaxial Geometry).

3. Effects of electrode geometry. - The general shape of the V-I curves obtained with the three different test section geometries was the same in all three cases. The transition phenomenon was noted with all three geometries.

A slight difference in the zero current intercept was found for the double wire geometry as compared to the other two geometries. With the double wire set-up, a zero volts - zero amps intercept was obtained. With the axial and coaxial arrangements, a negative voltage of approximately one volt was measured at zero current.

Besides investigating the effect of size, shape, and location of the electrodes as mentioned above, the effect of varying the electron-emitting area was investigated in the following manner. A simple experiment was performed with the axial geometry in which two "center electrodes" could be individually switched into the circuit (see Fig. 4). With the system in the normal mode and both electrodes initially conducting, one of the electrodes was open circuited; the total current decreased by less than 5 per cent. Alternating the two electrodes into and out of the circuit produced identical results; i. e., a slight reduction in the current with one electrode as compared with the case of two electrodes conducting. Approximately the same percentage decrease in the current was observed at 2, 5, 6, and 12 amps. With normal polarity (center electrodes as cathodes), a brief transition period (about one second) followed the opening or closing of the switches. With reversed polarity the transition time was extremely fast (a small fraction of a second).

4. Addition of diluent gases. - The effect of adding foreign gases

on the voltage-current characteristic is seen in Figs. 17 and 18. It is noted that small mole fractions of nitrogen radically change the shape and position of the curves. However, helium, even in large amounts, has little effect other than slightly displacing the curves.

5. Effect of impurities. - In some of the earlier test runs, the hot arc-jet gases came in contact with teflon insulators. Inspection of the insulators after a run indicated a relatively large amount of teflon ($\sim 1/3$ cm^3) had been vaporized. The effect of the entrained teflon is readily seen in the upper curve of Fig. 8. In comparing the two curves of Fig. 8, it should be noted that the effective length of the conduction region of Run 5-11-1 was one inch, while for Run 1-3/3-1 the length was one and one half inches. The most striking difference obtained between runs with and without teflon contamination was the voltage obtained with maximum external resistance, i.e., at minimum current. As strikingly indicated by Fig. 8, this voltage was up to 5 times larger in the case of contamination. In other runs with smaller amounts of contamination, the voltage-current characteristics would differ greatly at low currents (< 20 amps) and then approach each other rather closely at the higher currents. This trend is seen with the addition of nitrogen in Fig. 17.

During some runs, the amount of the teflon contamination appeared to vary in a quasi-periodic fashion. With all parameters fixed, the voltage and current were observed to oscillate slowly ($\sim 1/3$ cps) between two curves such as given in Fig. 8. When such oscillating phenomena were observed and the resulting V-I curves plotted, it was found that the lower envelope of the experimental points agreed quite

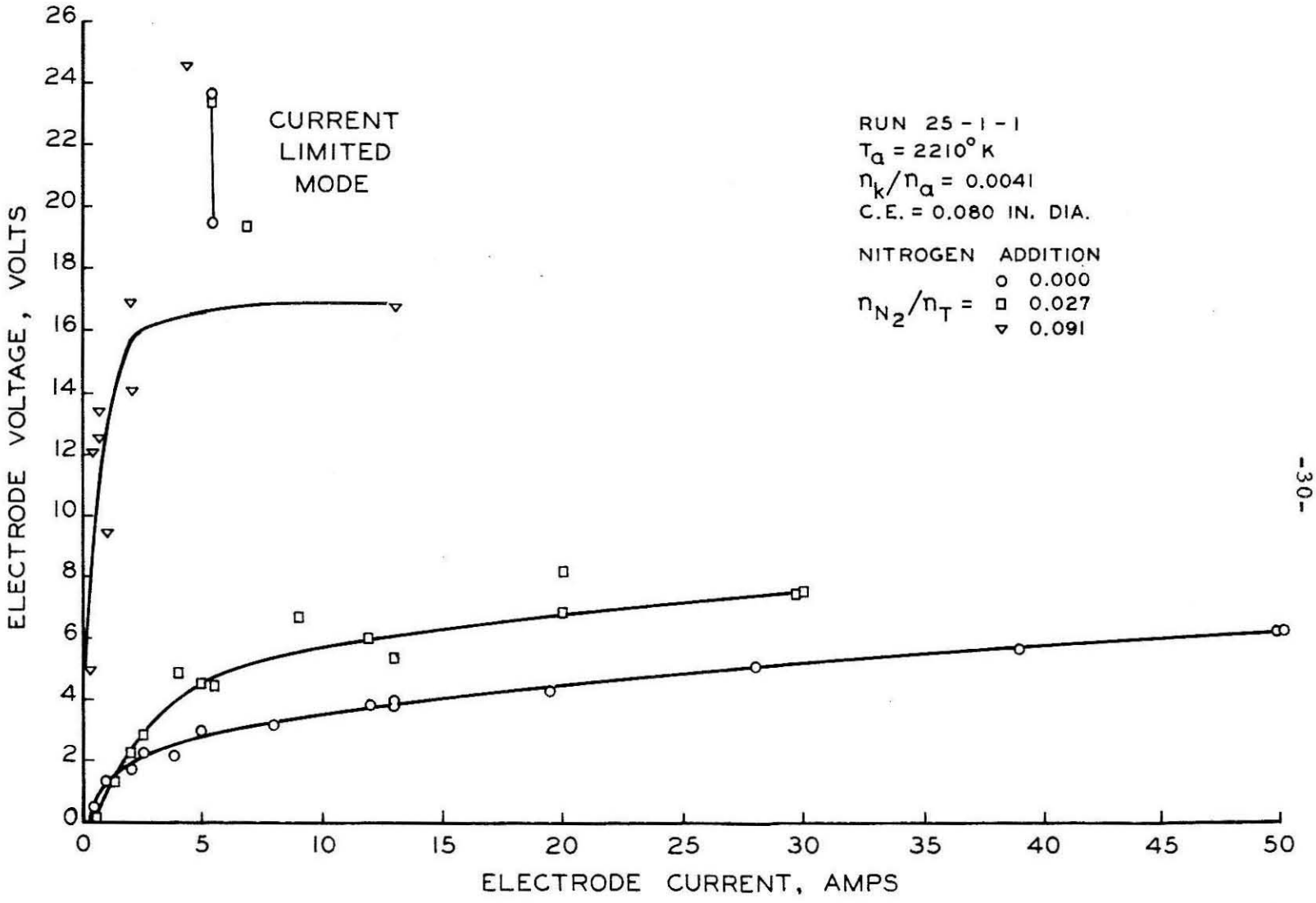

Figure 17. Voltage-Current Characteristics with Nitrogen Addition (Coaxial Geometry).

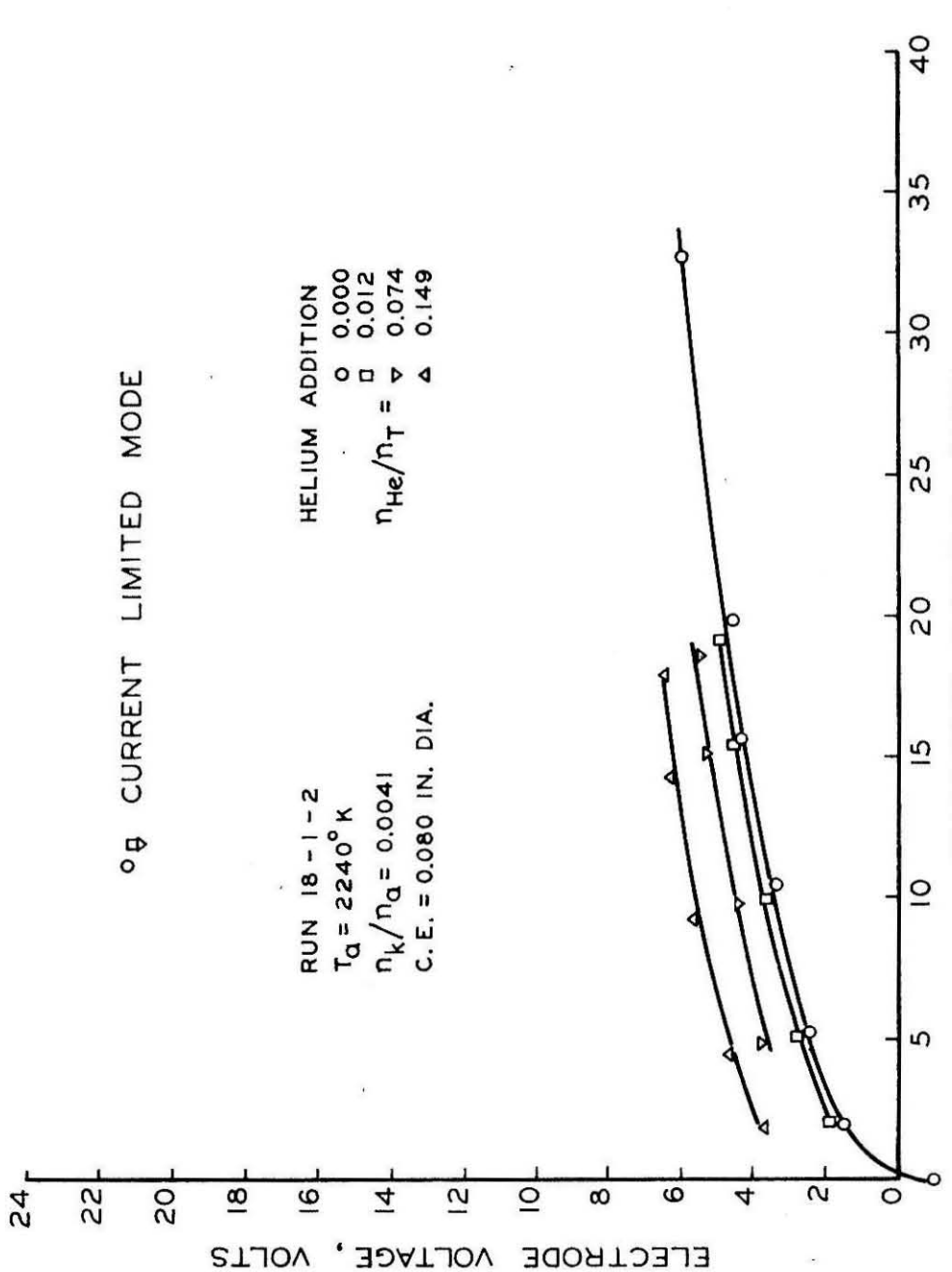

Figure 18. Voltage-Current Characteristics with Helium Addition (Coaxial Geometry).

well with V-I data taken under similar conditions in which there was no teflon contamination.

With the detection of the presence of impurities in the plasma, the question arises as to the reliability of the data and its reproducibility. An indication of the reproducibility of the data is given in Fig. 19 in which three runs are depicted. The runs were made under identical operating conditions on three separate days. Special care was taken to eliminate impurities in the aforementioned runs.

6. Gas temperature measurements. - In addition to recording the above-mentioned data during normal mode operation, a direct measurement of variation of the gas temperature was made during several runs. This was accomplished by using a sodium line reversal optical technique. Figures 20 and 21 depict the results of sodium line reversal temperature measurements plotted against the electrode voltage and the electrode current. The data in Fig. 20 was obtained with the sodium line reversal image positioned as shown in Fig. 2. Figure 21 was taken with the axial electrode configuration. The position of the SLR lamp image and the center electrode are as depicted in Fig. 4. In order to check the effect of the small viewing ports on the measured SLR temperatures, a test with no central electrode was conducted. In this test, the temperature was measured through the four ports and then with the entire image in the free jet and located adjacent to the outer edge of the test section. Identical temperatures were recorded in the three ports farthest downstream and in the free jet leaving the test section. The viewing port farthest upstream read a value about 150^{o}C lower. This was found to be due to an unavoidable misalignment

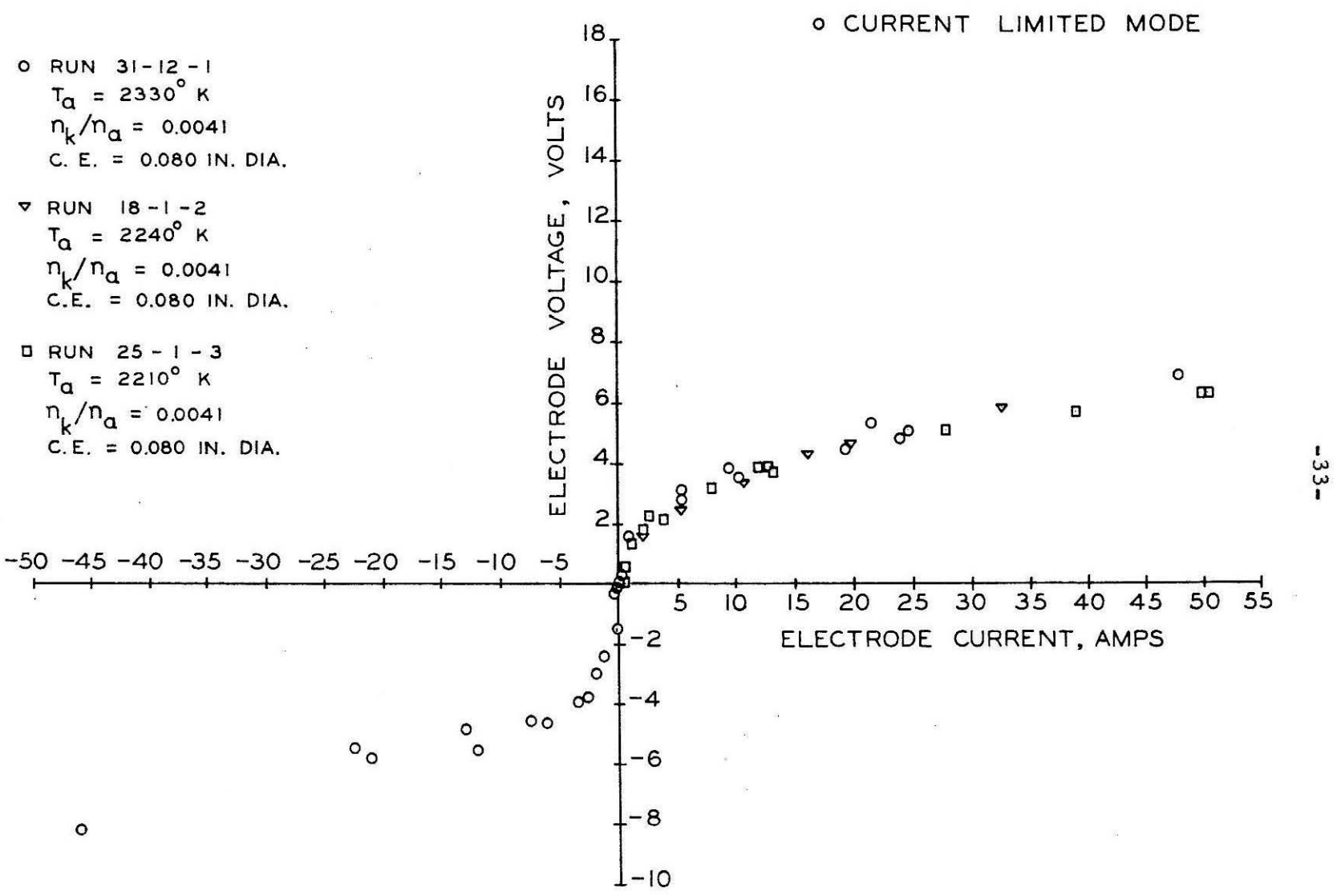

Figure 19. Voltage-Current Characteristic (Coaxial Geometry).

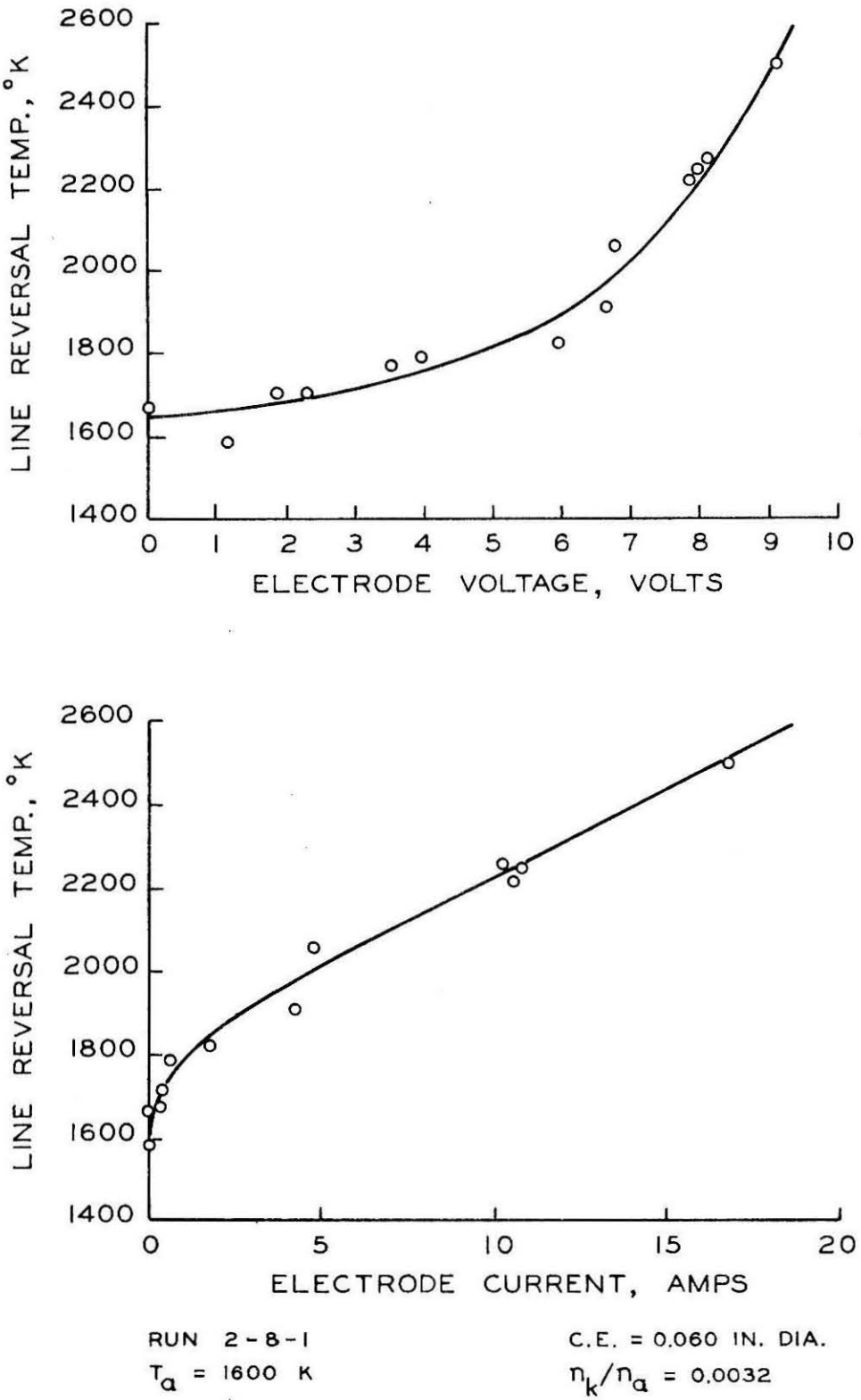

Figure 20. Sodium Line Reversal Temperature Data (Coaxial Geometry).

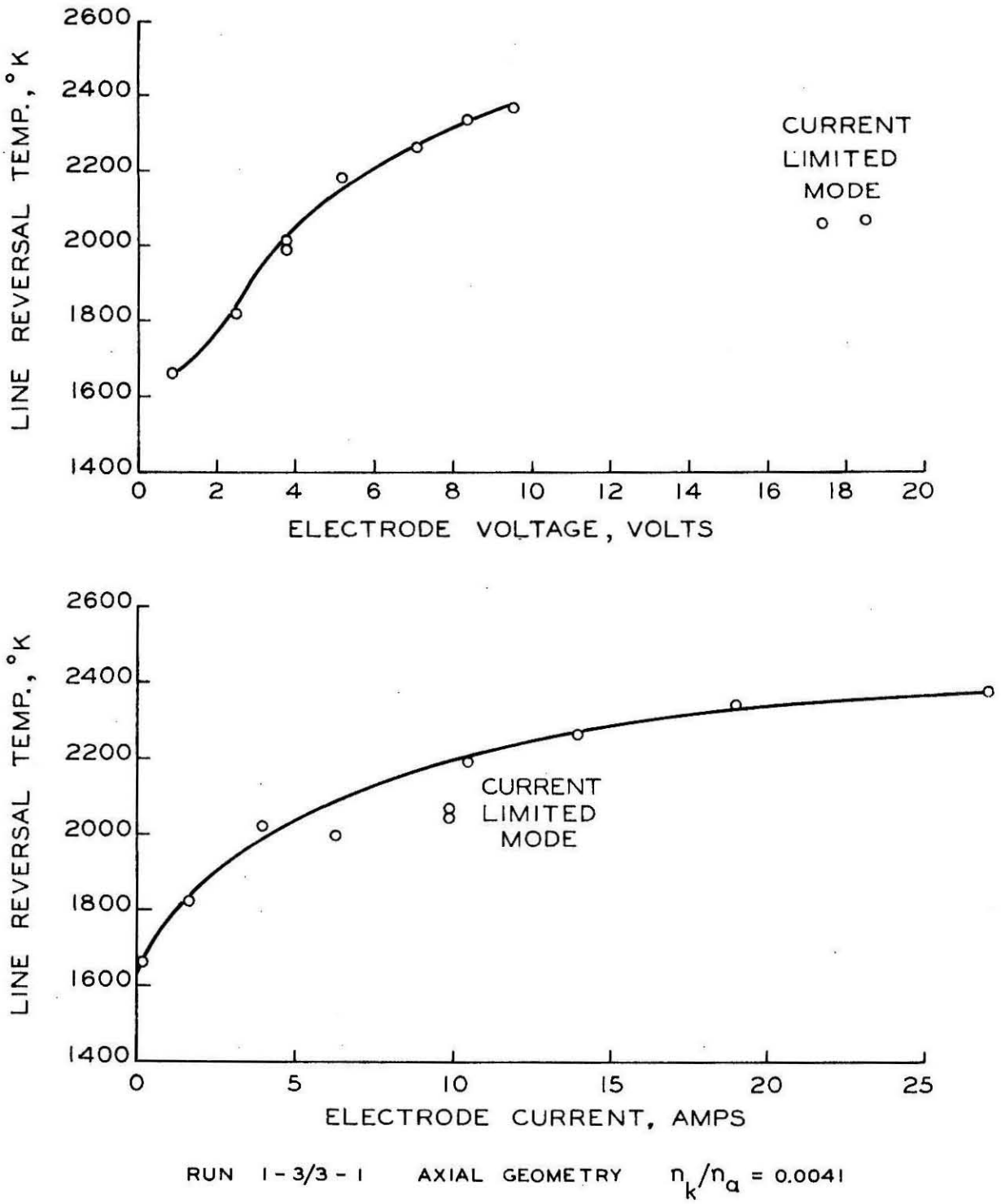

Figure 21. Sodium Line Reversal Temperature Data (Axial Geometry).

of the optical system when utilizing this port. Thus, only the temperatures from the second port were taken.

An experiment related to proper interpretation of the SLR temperature measurements was performed. Small amounts of nitrogen and helium were added to the flow with the electrodes open circuited. The variation of the measured SLR temperatures, along with the computed temperature decreases caused by the diluents, are depicted in Figs. 22 and 23. The "overshoot" in the temperature with nitrogen addition is especially interesting.

Figure 24 presents the measured SLR temperatures plotted against the distance from the jet axis for the case of zero test section current.

7. Electrode temperature measurements. - A series of typical electrode temperature variations with electrode current have been previously shown in Figs. 9, 10, and 12. These aforementioned temperatures were measured at a distance approximately 1/4" from the leading tip of the center electrode. The data plotted in these illustrations are from the same test runs as depicted in Figs. 5 and 6 as indicated. It is interesting to note that the electrode was continuously cooled to lower temperatures in Run 22-5-1 (positive polarity) even though the current was increased to 25 amps. Contrasting this with the large temperature increase with reversed polarity indicates a strong asymmetry between anode and cathode heat transfer rates. In reducing the temperature values from the optical pyrometer readings, the emissivity data of pure tungsten was employed. This procedure was experimentally checked by first measuring electrode temperatures in a pure argon atmosphere and subsequently adding the potassium seed and again recording the

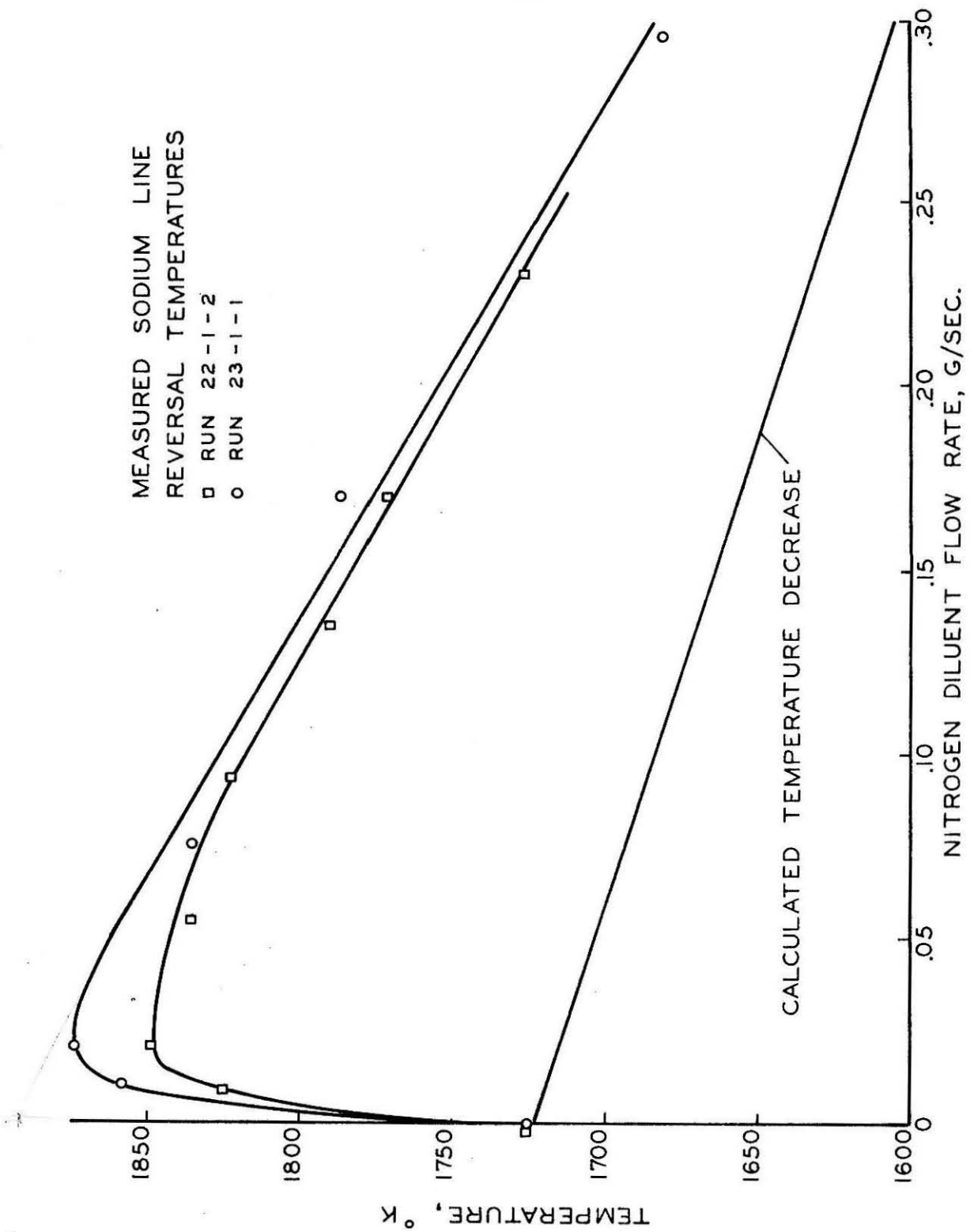

Figure 22. Gas Temperature Versus Nitrogen Flow Rate.

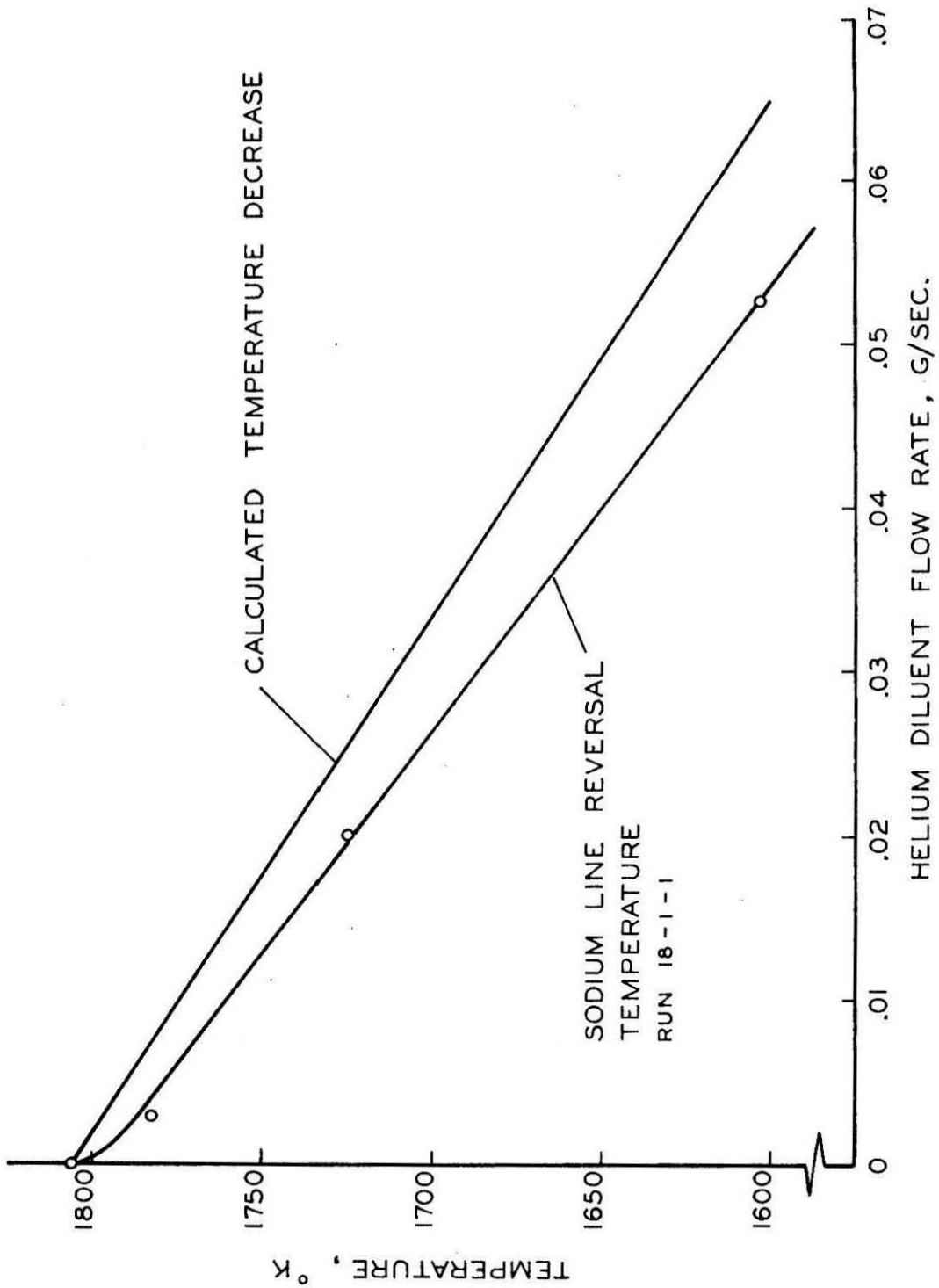

Figure 23. Gas Temperature Versus Helium Flow Rate.

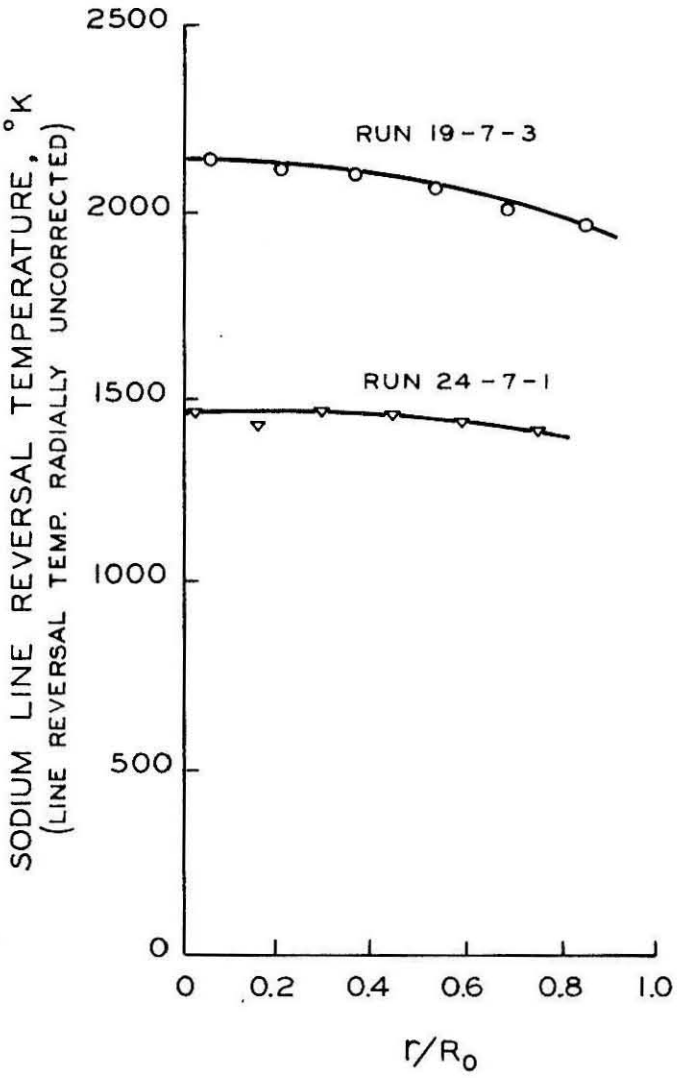

Figure 24. Radial Gas Temperature Distribution in Test Section.

temperature. Estimates of the error introduced by this procedure indicated the value to be no more than about 5°C, which is within the experimental scatter of the optical pyrometer measurements.

Figure 25 presents the temperatures of both the leading tip and the position along the wire corresponding to the downstream edge of the outer electrode. In this particular case, a "reversed" temperature gradient was obtained prior to transition to the current limited mode. With the electrodes operating in the current limited mode, a reversed temperature gradient along the center was always observed. This is noted in the points suitably designated in Fig. 25. Upon returning to the normal mode of current conduction, the temperature gradient returned to normal (tip of electrode hotter than downstream portion).

C. Transition Phenomena

A qualitative description of the transition phenomena has been previously given. It was found quantitatively that the maximum normal mode current which occurred just prior to transition increased monotonically with increasing seed concentration, as shown in Fig. 26. The large difference between the two curves shown in this last figure is indicative of the general results obtained in many tests of this type. It was found that the general trend was consistent between different electrodes and different runs. However, the magnitude of the aforementioned maximum current was apparently dependent upon the electrode surface ageing process and thermal history.

Transition to the current limited mode could be precipitated from normal operating conditions merely by reducing the potassium concentration. A return to the normal mode could then be accomplished by sufficiently increasing the seed fraction. A typical variation in the

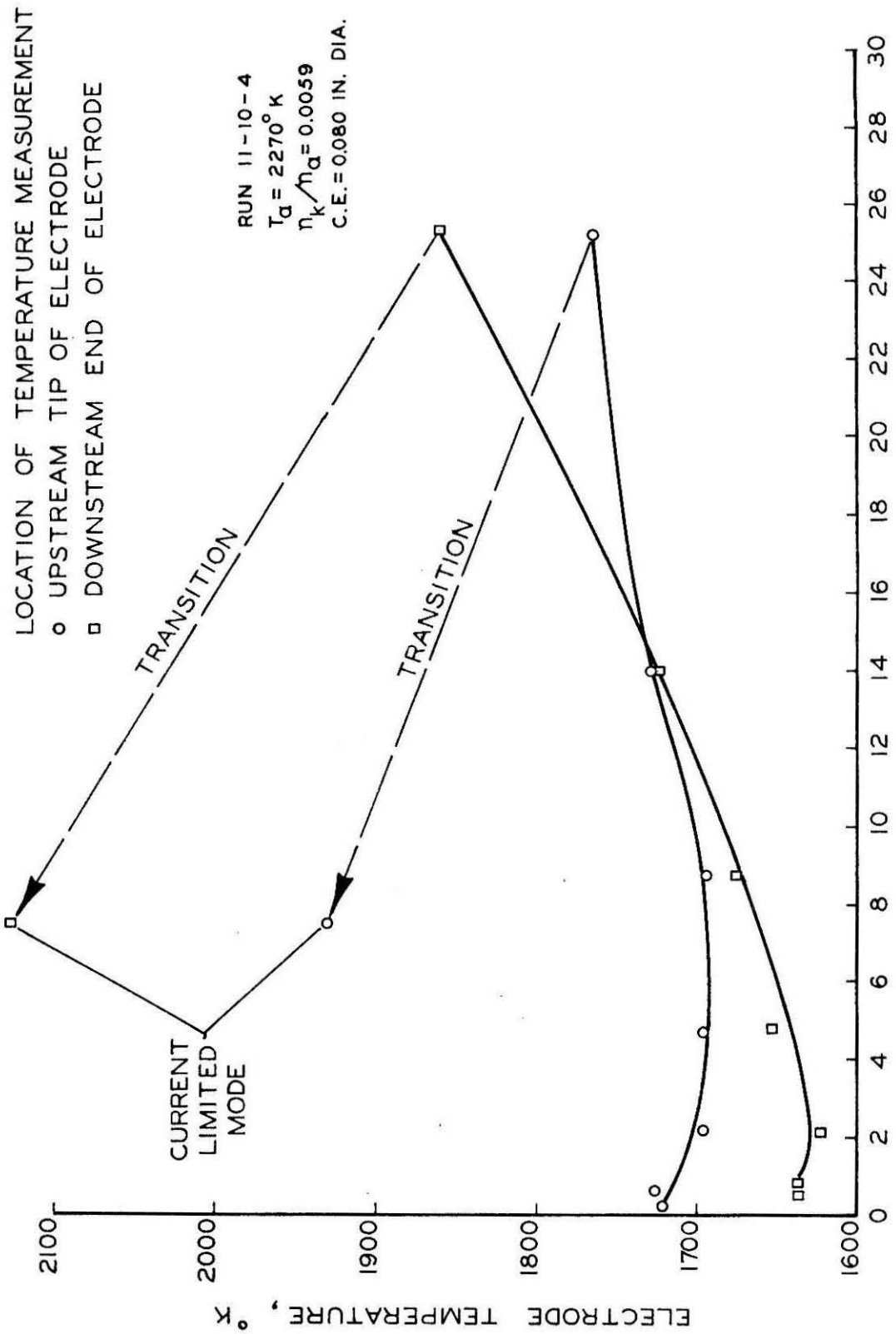

Figure 25. Center Electrode Temperature Versus Electrode Current (Coaxial Geometry).

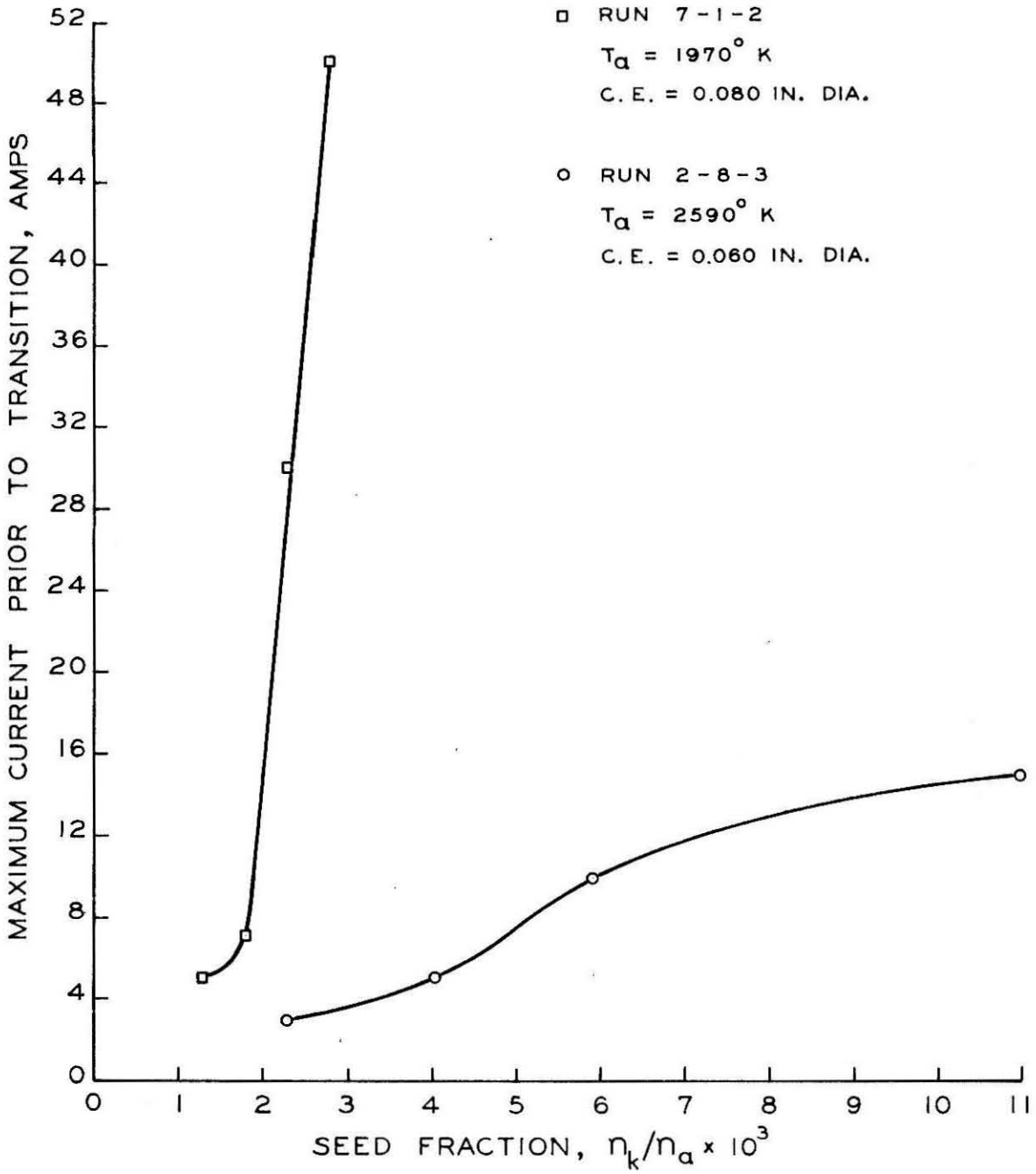

Figure 26. Maximum Electrode Current Versus Potassium Seed Fraction (Coaxial Geometry).

current caused by this large variation in n_k/n_a is given in Figure 27.

Reduction of the cathode surface area was another means of inducing transition to the current limited mode. This effect was observed in the aforementioned switching experiments. In one particular set of such experiments, about 20 amps was being conducted by the two electrodes in the normal mode. Switching one electrode out resulted in the remaining electrode passing into the current limited mode, and the current thus was reduced to approximately half the initial value. This behavior was observed whenever the two cathodes were conducting a current close to the magnitude of the maximum normal mode current.

D. Current Limited Mode Phenomena

1. Effect of electrode geometry and surface area. - Transition to a current limited mode was found to occur with all three electrode geometries. However, the magnitudes of the currents were different for each of the three geometries, even though the initial gas properties may have been the same. It should be noted here that the effective cathode emitting area was different for each of the three above-mentioned configurations.

The effect of changing the emitting surface area during operation in the current limited mode was accomplished by means of the switching experiment as described previously and depicted in Fig. 4. With the electrodes initially operating in the current limited mode, open circuiting one electrode resulted in a 50 per cent ($\pm$ 5 per cent) decrease in the total current. This effect was independent of which electrode maintained the current. Alternate switching of the electrodes produced the same 50 per cent reduction in the total current.

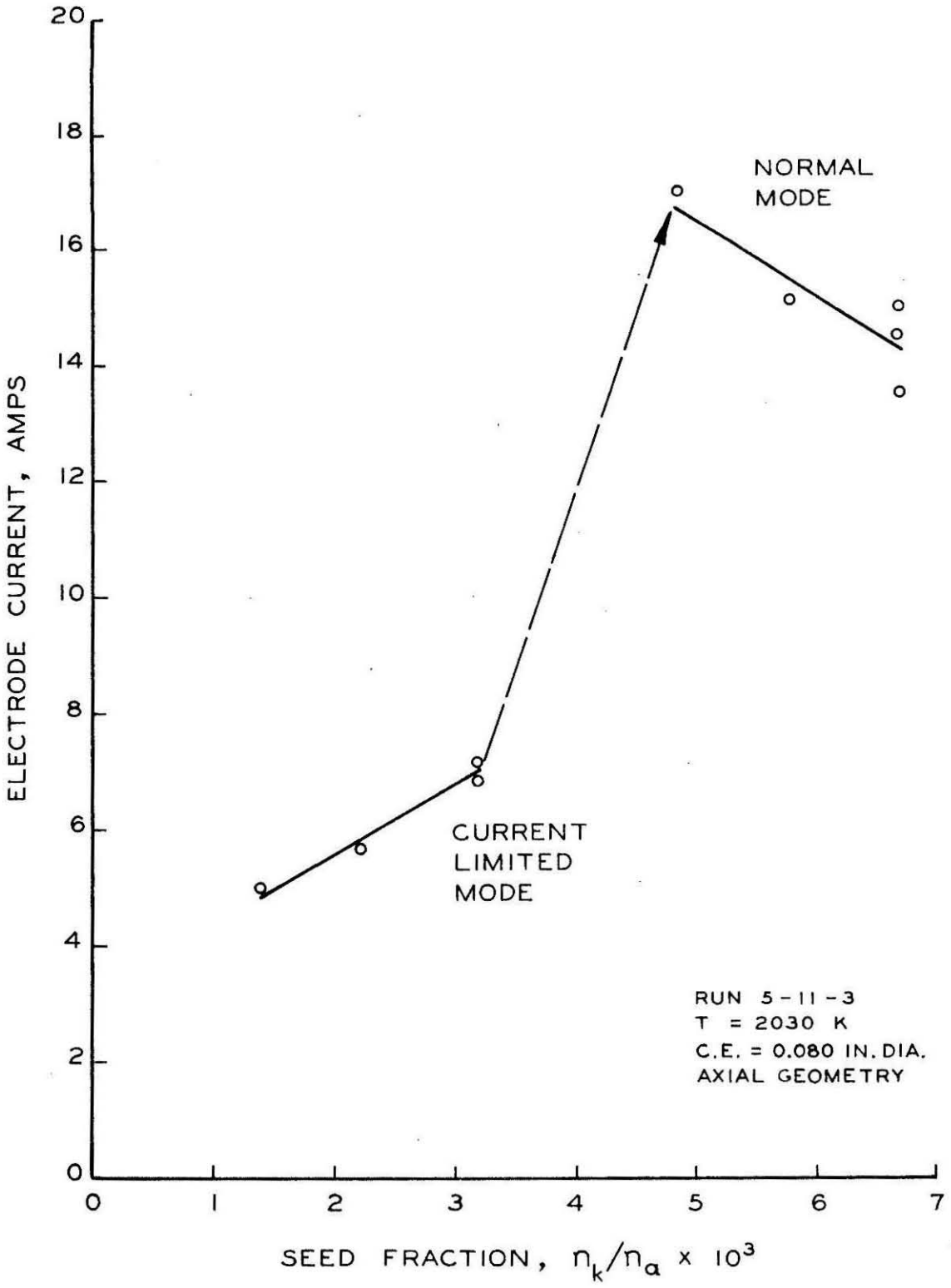

Figure 27. Electrode Current Versus Potassium Seed Fraction.

2. Effect of seed concentration and impurities. - The magnitude of the current obtained in this limited mode was dependent upon the seed fraction of potassium as depicted in Fig. 28. Simultaneously, the cathode temperature varied with seed concentration as shown in Fig. 29. It is noted that the wire is hotter near the downstream end of the test section than at the tip.

The addition of helium and nitrogen did not affect the magnitude of the currents in this mode if all other parameters were held constant. Similarly, the effect of teflon contamination had no influence on the current.

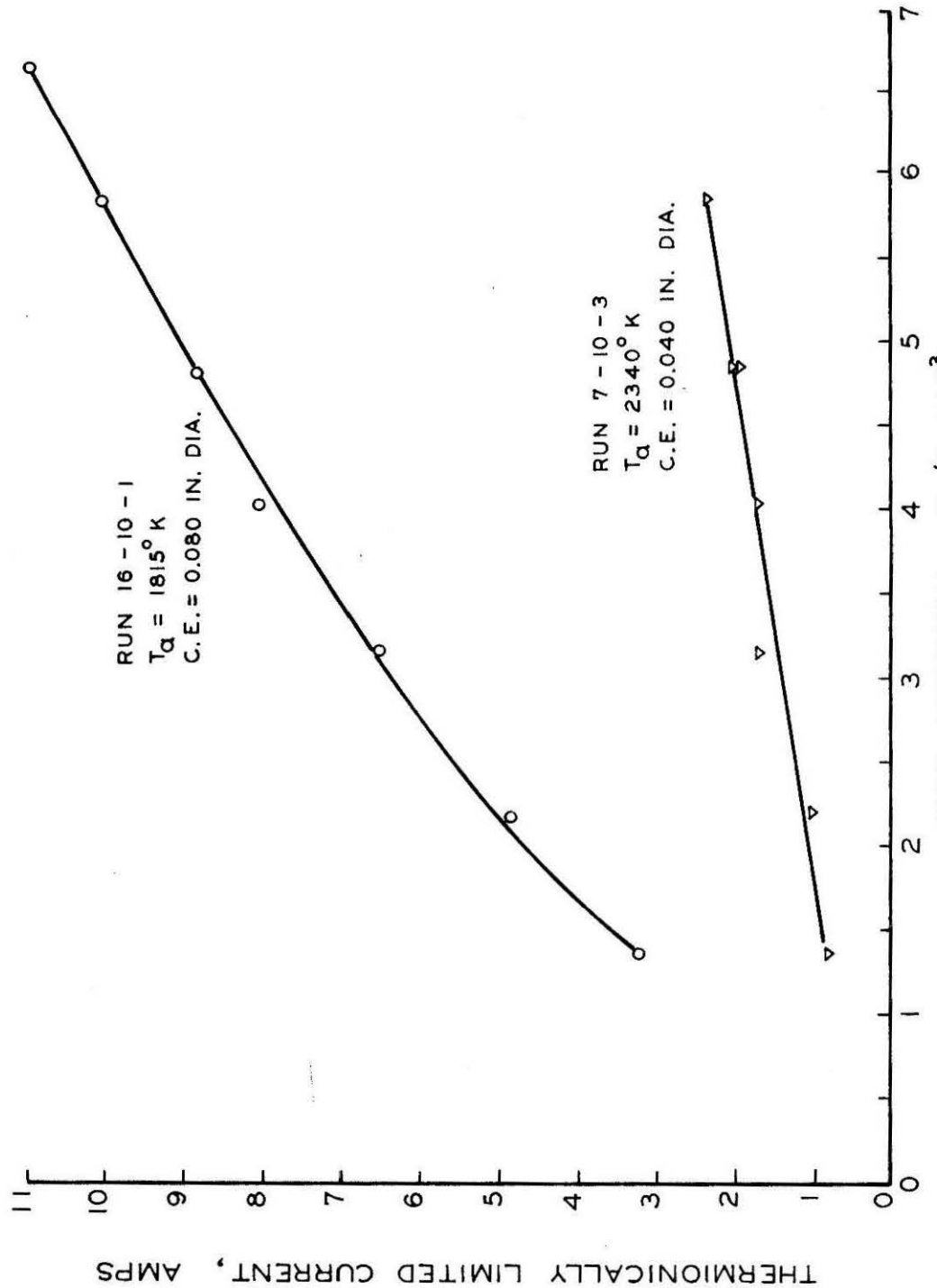

Figure 28. Electrode Current in Limited Mode Versus Potassium Seed Fraction (Coaxial Geometry).

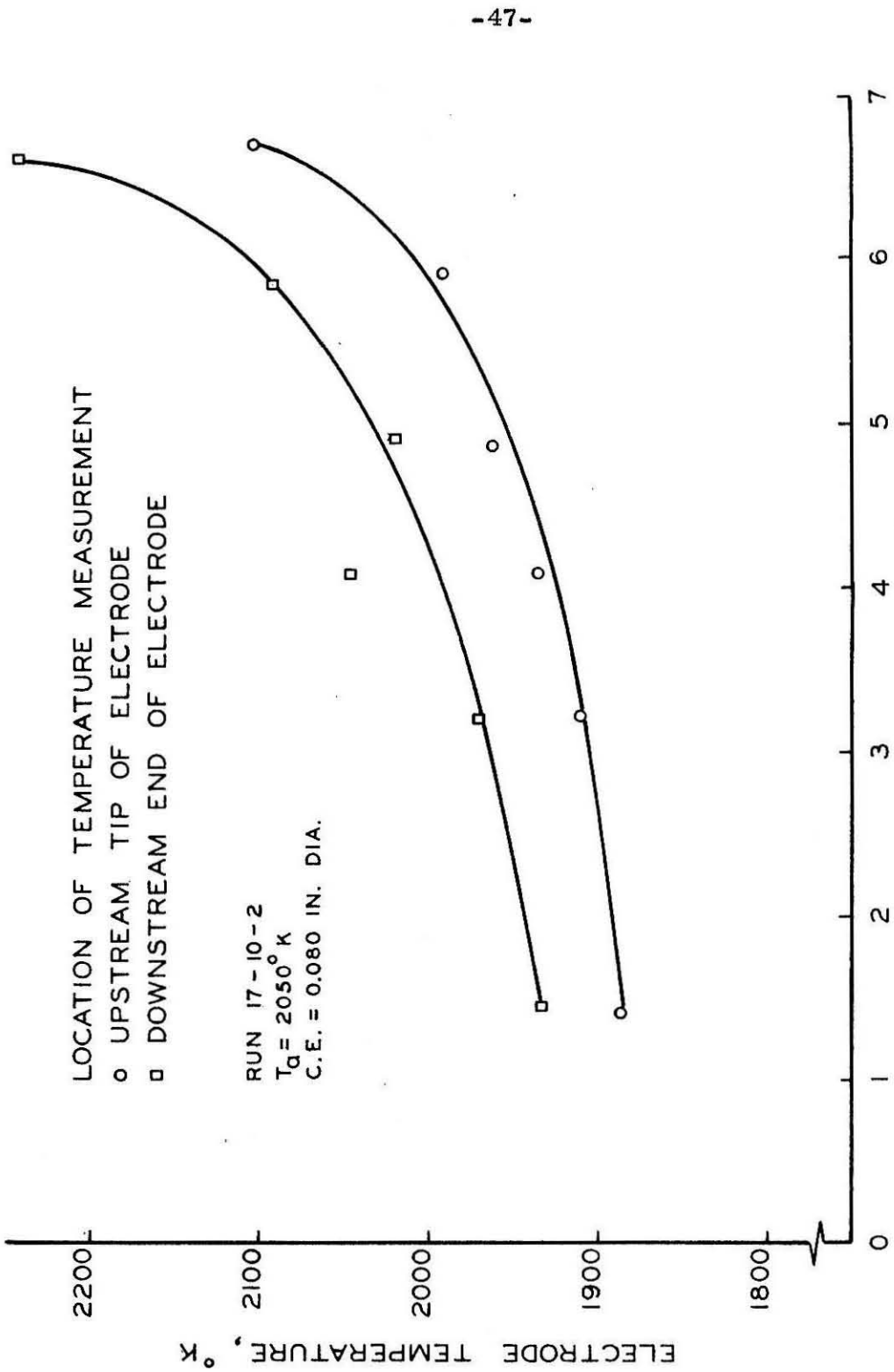

Figure 29. Center Electrode Temperature Versus Potassium Seed Fraction (Coaxial Geometry).

IV. DISCUSSION OF RESULTS

A. Potential Distribution in the Plasma

Before interpreting the results of voltage-current measurements in any plasma experiment, it is necessary to ascertain the relative magnitudes of the voltage drops across the gaseous conductor and those across gas-surface sheaths. In addition, in the particular experimental set-up employed here, there exists the possibility of appreciable voltage drops across comparatively cool gas boundary layers. Large voltage drops across either surface sheaths or boundary layers would result in gross errors in computing conductivities directly from voltage-current ratios.

It is the purpose of this section to discuss the problem of surface sheaths. The effects of voltage drops across thermal boundary layers will be considered separately for the various conduction theories in a later section.

If thermionic emission from the potassium-coated tungsten is greater than the current, then the sheath potentials should be on the order of kT_w. In contrast, with arc-like emission, the sheath voltage drops should be on the order of the ionization potential of the gas or surface material, which amounts to several volts in the present experiments. The general shape of the experimental voltage-current curves, and especially the low voltage observed at the zero current intercept, indicate that the sheath voltages are small. This suggests that thermionic emission may be adequate to account for the observed current densities.

The magnitude of the thermionic current emitted by a hot surface is given by the Richardson-Dushman equation,*

$$J = AT_w^2 e^{-\phi/kT_w} . \qquad (1)$$

In the case of a vacuum diode, this is the magnitude of the maximum current which may be drawn if the applied potential is maintained sufficiently low. At higher applied voltages, the Schottky effect becomes important, and the current continues to increase slightly with the applied voltage.

In the present experiments, all parameters in Eq. 1 can be easily determined except the parameter ϕ, which is the work function of the emitting surface. This parameter is extremely sensitive to surface conditions and is very strongly affected by the presence of adsorbed layers. Unfortunately, not much is known quantitatively concerning the effects on the value of ϕ of a layer or layers of potassium on a tungsten surface. Fortunately, though, a great deal of work has been carried out by Langmuir, et al.[2] with cesium layers adsorbed on tungsten, and at this point, it is of interest to review some of his results.

For the purposes at hand, the pertinent material from Langmuir's work is summarized in Fig. 30.[2] In this figure, the number of electrons emitted per unit time per unit surface area (ν_e) is plotted against the reciprocal of the surface temperature. The lines indicated as different values of θ_n refer to loci along which the fractional coverage of the surface by adsorbed cesium is a constant. In particular, the

* Symbols are defined in Appendix A, page 114.

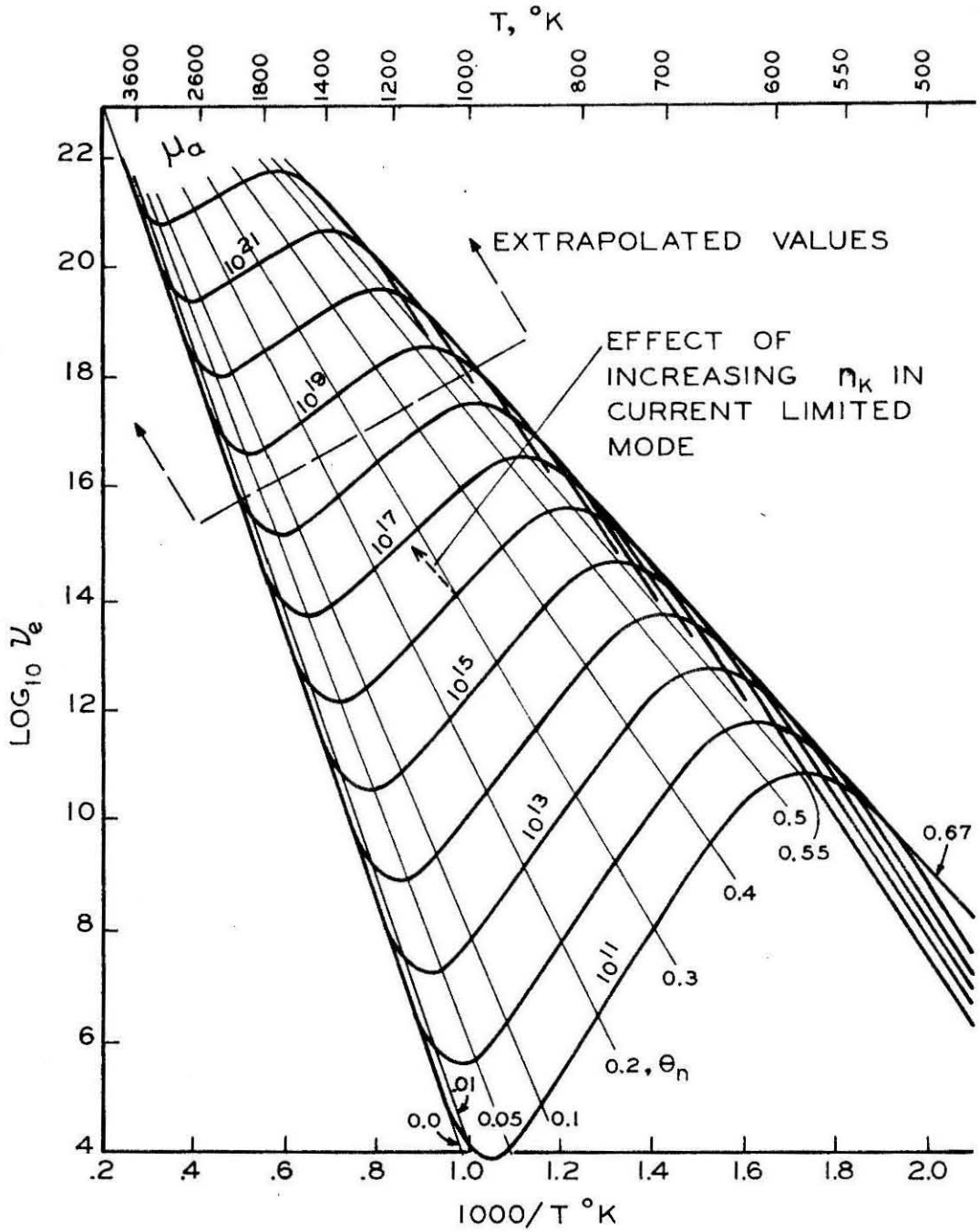

Figure 30. Logarithm of Thermionically Emitted Electron Flux Density ($cm^{-2}sec^{-1}$) Versus Reciprocal of Surface Temperature.

line with $\theta_n = 0$ gives the emission from a bare tungsten surface. As a larger fraction of the surface is coated with the cesium, the effective work function changes from that of pure tungsten to the value expected for pure cesium.

The various values of μ_a refer to the rate at which cesium atoms strike the surface per unit time per unit area. It is readily seen that if T is held constant, then increasing μ_a results in an increased fractional coverage (θ_n) and a larger emission current, ν_e. However, if μ_a is held constant and the temperature is increased, the emission current actually decreases over a wide range of θ_n values. Extrapolation of the data in Fig. 30 to values of $\mu_a = 10^{20}$, which were encountered in these experiments, indicated that currents comparable to those observed experimentally could be obtained.

At present, no data for electron emission from potassium-coated tungsten is available in the range of parameters for the experiments described here. However, extrapolation of Killian's[3] data by five orders of magnitude indicates current densities of at least 10 amps/cm^2 are possible. The shape of the potassium-tungsten curves is similar to the cesium-tungsten case. However, the line of maximum emission in the former situation nearly coincides with the $\theta_n = 0.4$ line in Fig. 30. Because of the immensity of the aforementioned extrapolation, it is quite possible that a large error exists in the estimated value of the emission current.

In addition to the above estimations concerning the magnitude of the thermionic emission current, several other factors also lend support to the idea of small thermionic-sheath potentials for the case of the normal mode.

In the previously mentioned switching test, the reduction of the emitting area by a factor of two required only about 0. 1 volt increase to maintain the same current (normal mode case). This result was obtained at both high and low currents. As this resulted in doubling the current density in the sheath, it is evident that sheath voltage drops must either be small in comparison with the potential drop across the bulk of the plasma, or very insensitive to current density. If this latter situation were the case, the normal mode V-I curves would increase very steeply at low currents until a critical voltage were obtained and then break over sharply into a curve with the voltage essentially independent of the current. However, examination of the voltage - current characteristics indicates a smooth, gradual, continuous rise from zero current. Thus, this observation, along with the insensitivity of the V-I curve to the emitting surface area at low currents, also lends support to the idea of small sheath potentials.

The strong dependence of the normal mode voltage-current characteristics on the bulk gas temperature, the seed fraction, and the presence of impurities confirms the dominance of gas phase phenomena in the normal mode. Of particular note in this regard is the observed optimum value of the seed concentration which is predicted by gas kinetic considerations.

Finally, additional evidence is obtained by comparing the two branches of the voltage-current characteristic. Examination of the characteristics for the normal mode shows that the curves for both polarities are roughly similar in an approximate sense. With normal polarity, the electrons are emitted from a relatively hot (1200 - 1700°C)

tungsten wire having a small area (0.91 cm^2). In the case of reversed polarity, the current was emitted from a comparatively cool (900 - 1300°C) stainless steel electrode having a large area (4.23 cm^2). The cathode sheaths would thus be expected to differ considerably for the two polarities. If most of the potential drop was across the wall sheaths, then a very strong dissymmetry would be anticipated in the V-I curves for the two polarities. This conjecture does not agree with the aforementioned similarity of the two branches of the voltage-current characteristics.

At this point, it might be argued that the conduction phenomenon is really an arc process. Because of the presence of potassium in the gas, the arc would be referred to as a "gas arc" in the nomenclature of Cobine[4]. In this type of arc, the dominant phenomena are determined by gas effects and are relatively insensitive to cathode and anode material surface condition and surface temperature. However, the previously mentioned experimental observation of arc formation near the surface of cold electrodes and its absence for hot electrodes is an additional point supporting thermionic emission. The diffuse nature of the observed current conduction also supports this contention.

Thus, in view of the several considerations above, the interpretation of normal mode data will assume the potential to drop across the gaseous conductor, while the sheath potentials will be neglected in general. Until further experiments indicate otherwise, it will be assumed that thermionic emission is sufficient to provide the observed currents in the normal mode of conduction.

At this point, an objection may be raised concerning the magni-

tude of the open circuit voltage observed in these experiments. From a study of thermionic emission, it is readily seen that the net current due to thermionic emission may be reduced to zero with sheath potentials of a few kT_{vv}. This amounts to a sheath potential of a few tenths of a volt, and thus cannot account for the observed voltages which are on the order of a volt.

Chapman and Cowling[5] show that when a temperature gradient exists in a gas, and no current is conducted, a potential gradient must simultaneously exist. This is a gas effect which occurs in the bulk of the gas, and is dependent only upon gas properties and the temperature gradient in the gas. With the double wire geometry, the net effective temperature gradient was zero, and as anticipated, the open circuit voltage was precisely zero. The large temperature difference between the two electrodes in the coaxial case produced a significant net temperature gradient in the gas. In order to obtain quantitative information from Chapman and Cowling's equations, the values of the ordinary diffusion coefficient, and especially the thermal diffusion coefficient, must be known. Unfortunately, this data is not currently available for the plasmas utilized in this set of experiments. Until this data becomes available, it will be assumed that this effect of the gas temperature gradient will be sufficient to account for the observed open circuit voltages.

The above arguments hold for the normal mode. Inasmuch as the currents in the current limited mode are smaller and the electrode temperatures higher, it is certainly possible that emission in this case is by a thermionic process. In fact, the lack of dependence of current

on the voltage suggests that the current is the thermionically limited current. This hypothesis is supported by the data obtained in the electrode switching experiments which indicate that the current is directly proportional to the electrode surface area, and by other experiments which indicate that it is independent of such gross properties of the gas as temperature and impurity level. The increase in current obtained when seed concentration is increased is in good qualitative agreement with this hypothesis, and the results of Langmuir summarized in Fig. 30.

The fact that thermionic emission provides the electrons in the current limited mode does not necessarily mean that the sheath potentials are small for this case. As seen in Fig. 5, the difference between the voltages in the normal and current limited modes for the same current indicates that a voltage on the order of 10 volts may exist across the cathode sheath in the steady, current limited mode.

In conclusion, the view adopted here will be one to assume that thermionic emission is sufficient to account for the observed currents in all modes of operation. In the normal mode, the circuit current is always less than or equal to the thermionic limited value, and sheath potentials are of the order of one kT_w. In the current limited case, circuit current is equal to the thermionic limited value, and sheath potentials are on the order of 10 volts.

B. Effect of Gas Phase Phenomena

As explained in the preceding section, the experimental evidence provides a strong argument for interpreting the normal mode voltage-current characteristics solely in terms of gas phase effects.

In this section, the data will be analyzed from this viewpoint, and conclusions will be drawn concerning the conductivity of the gaseous phase. Before attempting to explain the non-linear features of the observed V-I curves, consideration will be given to some of the experimental effects which may be more readily explained in a simple manner.

The first point in the discussion will be an explanation of the observed maximum in conductivity with varying seed concentration. Values of the conductivity calculated at low currents will then be compared with values computed from the classical theory.

In order to account for the shapes of the voltage-current characteristics, two current conduction theories will be presented and compared with experimental results. The first theory is based on the classical equilibrium approach, and relies on the effect of Joule heating of the gas to explain the observed phenomena. The second theory is often referred to as a "non-equilibrium" theory in that it incorporates an electron temperature which is elevated above the gas temperature. This section will then conclude with a discussion of the relative merits of the two theories.

1. Dependence of the gas conductivity on the seed fraction. - In the limit of small currents in the gas, it is permissible to assume that the conductivity may be accurately computed by perturbation techniques such as employed in Ref. 5. Figure 31 presents the results of computing the conductivity according to the following relations:

$$\frac{1}{\sigma} = \frac{1}{\sigma_{C.E.}} + \frac{1}{\sigma_{sp}} \qquad (2)$$

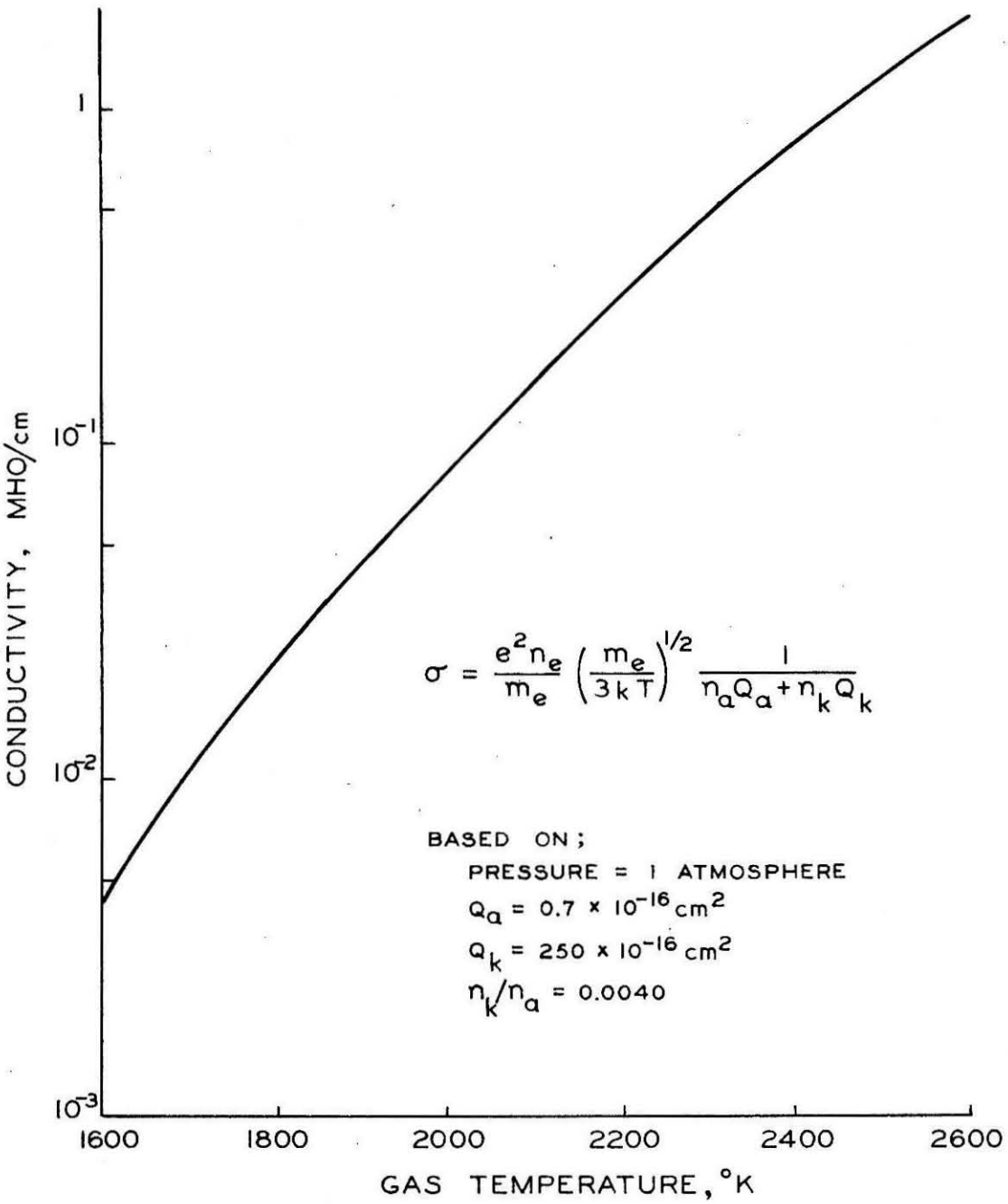

Figure 31. Equilibrium Conductivity Versus Gas Temperature.

where the effect of the electron-atom collisions (close encounters) is given by

$$\sigma_{C.E.} = \frac{e^2 n_e}{m_e\left(\frac{3kT}{m_e}\right)^{\frac{1}{2}}} \frac{1}{n_a Q_a + (n_k - n_e) Q_k} \quad , \tag{3}$$

and electron-ion collisions are accounted for by evaluating the σ_{sp} term (Spitzer conductivity[6]).

$$\sigma_{sp} = \frac{1}{.0176}\, n_e\, \epsilon_o^2 \left(\frac{2kT}{m_e}\right)^{3/2} \frac{1}{\log \Lambda} \tag{4}$$

where

$$\log[\Lambda] = \log\left[\frac{12\pi\,(\epsilon_o kT_e)^{3/2}}{(e^3\, n_e^{1/2})}\right] \quad . \tag{5}$$

Over most of the temperature range utilized in these experiments, the contribution of the σ_{sp} term may be neglected. The required value of the electron concentration is obtained from the Saha equation:

$$n_e^2 = \left(\frac{4\pi\, m_e}{3h^2}\right)^{3/2} (n_k - n_e)\, \epsilon_e^{3/2}\, e^{-\frac{3}{2}\frac{\epsilon_i}{\epsilon_e}} \quad . \tag{6}$$

It is now possible to find the optimum value of the seed concentration n_k for the case of constant temperature T_a. For very small degrees of ionization, $(n_e) \propto \sqrt{n_k}$, and substituting this relation into Eq. 3, it is seen that

$$\sigma \propto \sqrt{n_k}\,/(n_k Q_k + n_a Q_a) \quad .$$

Then

$$\left.\frac{\partial \sigma}{\partial n_k}\right|_{T_a} = \frac{\frac{1}{2}(n_k)^{-\frac{1}{2}}}{n_k Q_k + n_a Q_a} - \frac{\sqrt{n_k}\, Q_k}{(n_a Q_a + n_k Q_k)^2} = 0 \quad , \tag{7}$$

and it follows directly that

$$\left.\frac{n_k}{n_a}\right|_{opt} = \frac{Q_a}{Q_k} \qquad (8)$$

for the condition that the conductivity be a maximum. Figure 32 gives the variation of σ with n_k for the particular values of cross sections stated there. A reasonable estimate of the value of $n_k/n_a\big|_{opt}$ is .0028, based on $Q_k = 2.5 \times 10^{-14}$ cm^2 and $Q_a = 7 \times 10^{-17}$ cm^2. (7) This is to be compared with the average experimental value of 0.003. In view of the great degree of uncertainty in the value of the cross sections under the low temperature conditions of these experiments, this may be considered very good agreement.

The values of the cross sections used in the above estimate were obtained by averaging over a Maxwell velocity distribution and are the available data. (Other values of Q_a and Q_k have been reported, and they give values of the cross section ratio varying from 0.0007 to 0.02; cf. Refs. 8 and 9.)

The experimental scatter in the optimum seed value may be due in part to the strong variation of the cross section for argon with electron energy, since the temperature range of these experiments lies in the "Ramsauer portion" of the Q_a vs. energy curve. In fact, the trend given by the location of the conductivity maxima with bulk gas temperature indicates a minima in the argon cross section. The location of this minima in Q_a is not accurately known because of the difficulties in performing scattering experiments at low electron energies. However, the curve quoted in Ref. 10 seems to be qualitatively in accord with the experimental variation of $n_k/n_a\big|_{opt}$ with T_a.

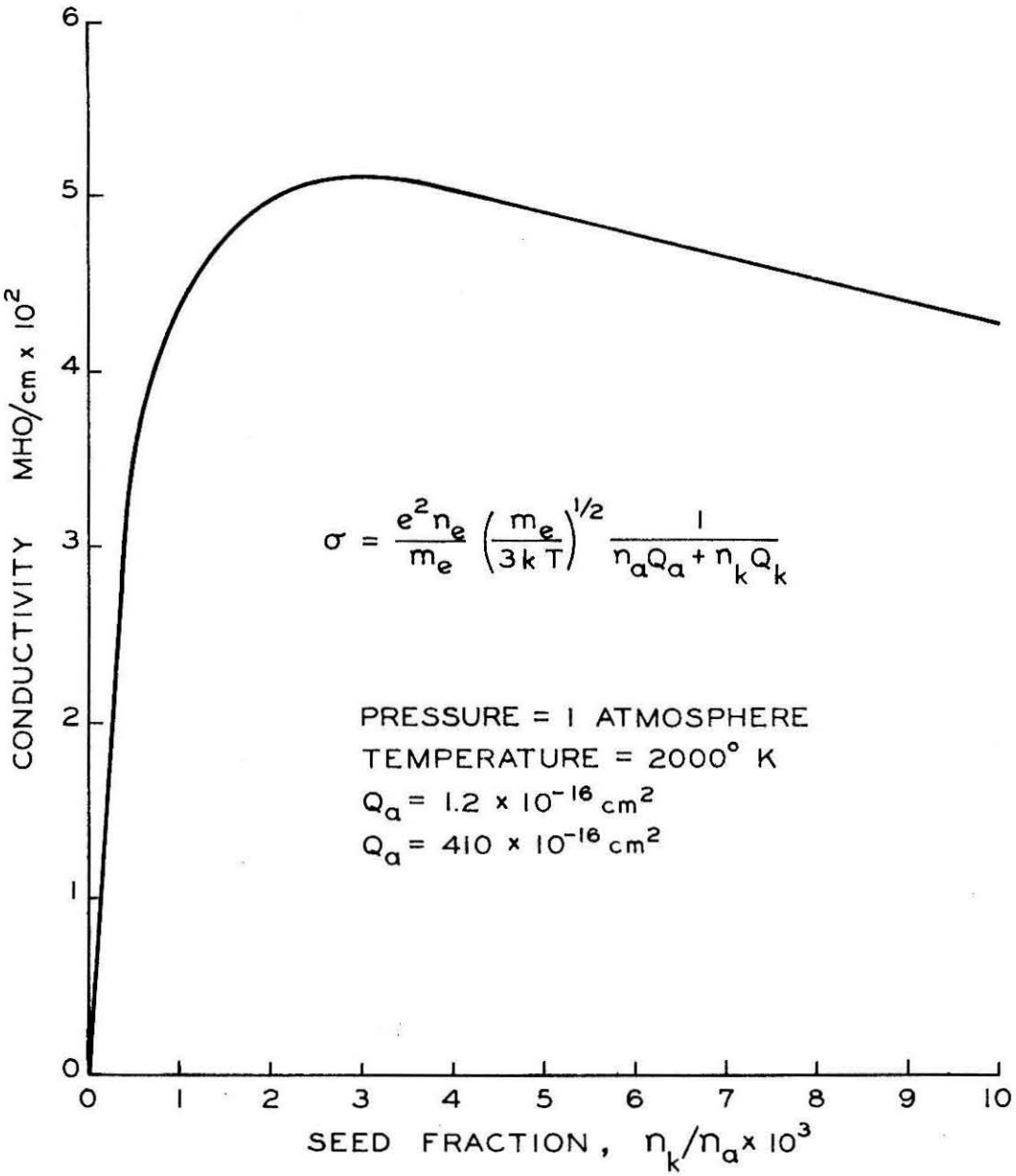

Figure 32. Equilibrium Conductivity Versus Potassium Seed Fraction.

The relation $n_k/n_a\,\big|_{opt} = Q_a/Q_k$ was derived with the assumption of constant gas temperature. In the early experiments, because of the variation of the total mass flow with seed concentration, the temperature decreased with increasing seed concentration. However, the effect of this temperature variation was quite small, as more recent seed optimization tests performed at constant gas temperature agreed quite well with the earlier data. (See Figs. 13 and 16.) The sharper conductivity maxima observed with the variable temperature set-up is anticipated, because the increase in total cross section is augmented by the decreasing temperature in the process of reducing σ after the maximum value has been obtained.

Another factor which must be considered in the interpretation of the seed optimization experiments is the effect of the sheath potentials (V_s). In the tests, the quantity $V_e = V_g + V_s$ is measured rather than the potential drop across the gaseous conductor (V_g). As R_{ext} had a large fixed value during the tests, the current did not vary more than 10 per cent, and thus V_s may be considered as a constant.

The experimental curves determine the condition

$$\frac{\partial(V_e/I)}{\partial n_k} = \frac{\partial\left\{\dfrac{(V_g+V_s)}{I}\right\}}{\partial n_k} = 0 . \qquad (9)$$

But from the circuit equations,

$$I = \frac{(V_b + V_s)}{R_{ext} + (V_g/I)} , \qquad (10)$$

which results in

$$\frac{\partial(V_e/I)}{\partial n_k} = \frac{\partial(V_g/I)}{\partial n_k}\left\{1 + \frac{V_s}{V_b + V_s}\right\} . \qquad (11)$$

In these experiments V_s was less than a volt, while V_b was approximately 24 volts. Thus, the difference between $\partial(V_e/I)/\partial n_k$ and $\partial(V_g/I)/\partial n_k$ is a negligible quantity for the conditions of the above experiments.

In a number of the seed optimization experiments, sodium was also present in the potassium pot and thus was entrained in the secondary argon flow. It is then necessary to investigate the effect of sodium on the conduction properties of the plasma. The ionization potentials of sodium and potassium are 5.14 eV and 4.34 eV, respectively. For the small degree of ionization present in these experiments, the ratio of ionized sodium atoms to ionized potassium atoms should be on the order of $e^{-\Delta\phi/kT} = e^{-0.80/0.2} = e^{-4} = 0.18$. This indicates that the potassium is the only source of electrons which needs to be considered. At the working temperature of the potassium pot (520°C), the vapor pressures of sodium and potassium are approximately 8 and 60 mm Hg, respectively. Thus, the ratio n_{Na}/n_K is 8/60. In assessing the relative effect on the conductivity, a comparison of $n_K Q_K$ and $n_{Na} Q_{Na}$ must be made. From Ref. 8, the appropriate cross sections are: $Q_{Na} = 350 \times 10^{-16}$ cm^2 and $Q_K = 410 \times 10^{-16}$ cm^2, and there results the ratio $n_{Na} Q_{Na}/n_K Q_K \cong 0.11$. Thus, a decrease on the order of 10 per cent in the value of the conductivity would be expected with the introduction of sodium into the potassium pot. In view of the magnitude of other experimental errors, this correction will be neglected here.

2. Low current conductivity. - As will be shown later in this section, at low current densities the non-equilibrium conduction effects

become less important. Thus, it is appropriate to compare the experimental conductivity values obtained at low currents with the values computed by the equilibrium model. However, at low currents and thus low voltages, the effects of sheath potentials become relatively more important. In order to circumvent this difficulty, values of V/I were computed for $V \geq 2$ volts, and the resulting data were extrapolated to zero current. These extrapolated values of V/I were then utilized in computing the conductivity values given below in Table II and compared with corresponding theoretical values.

TABLE II

Comparison of Conductivity at Low Currents with Equilibrium Theory

Run	T_a	n_k/n_a	$\sigma\|_{exp}$	σ_{theory} *
22-5-1	2500°K	.0032	0.36 mho/cm	1.16 mho/cm
9-5-3	2360	.0032	0.14	0.68
25-1-3	2210	.0041	0.10	0.35
8-2/3-1	1780	.0041	0.057	0.016

* Based on $Q_a = 0.7 \times 10^{-16}$ cm^2, $Q_k = 250 \times 10^{-16}$ cm^2

The results shown in Table II indicate that computed values of σ are three to four times the experimental values, with the exception of the low temperature (1780°K) run. In view of the uncertainties in cross sections and gas properties, the disagreement between theoretical and experimental values is not unexpected.

The non-equilibrium theory discussed later in this section predicts an increasingly stronger effect on σ at low current densities as

the gas temperature is reduced. Thus the fact that the experimental conductivity exceeds the computed conductivity may be attributed, at least in part, to the effects of non-equilibrium conduction.

3. Interpretation of non-linear voltage current curves. - Examination of the V-I curves (Figs. 5, 6, 7, and 8) reveals a decreasing slope with increasing current. Assuming that the major portion of the applied voltage is dropped across the bulk of the gas, the decreasing slope may be interpreted as an increase in the conductivity with an increase in the current. The validity of the above assumption has been examined previously in the section concerning the potential distribution in the plasma. A brief description of two simplified theories of current conduction which predict the aforementioned conductivity behavior will now be presented.

(a) Equilibrium theory of current conduction. - Inspection of Eqs. 3 and 6 indicate that the electron density, and thus the conductivity, are strong functions of the gas temperature. This fact suggests that at least part of the apparent increase in conductivity observed with increasing current may be due to Joule heating of the gas as it flows through the test section. The magnitude of the effect of Joule heating has been examined analytically by use of the following model.

The variation of gas conductivity with temperature is approximated by the relation

$$\frac{\sigma}{\sigma_o} = e^{\Gamma(T/T_o - 1)} \tag{12}$$

where σ_o is the conductivity of gas temperature T_o, and σ is the conductivity at temperature T. (Γ) is a constant chosen to give a good fit of the equation with calculated values of conductivity over the

temperature range of interest.

The coaxial geometry is analyzed under the assumptions that current flows radially and heats the gas; all of the Joule heating goes to increase the gas temperature locally, and thermal conduction effects are neglected.

Consider an element of gas moving down the test duct. As it moves downstream, it is heated, and consequently the conductivity, and therefore the local current density, will also increase. The net effect is that as the total current passing between the electrodes increases, the voltage drop first increases linearly with current, but for larger currents increases more slowly and finally reaches an asymptotic value.

A brief discussion of the procedures employed in computing a voltage-current characteristic based on the aforementioned conductivity variation is presented in Appendix B. The effect of gas boundary layers is considered there in an approximate manner, and the resulting computations are found to differ not too appreciably from the case where boundary layers are neglected. The theoretical curves shown below are thus based on the neglect of the effects of boundary layers.

Figures 33 and 34 present a comparison of typical experimental runs and the corresponding theoretical curves based on the conditions of the actual test run. The agreement between the curves is qualitatively satisfactory, except that the theoretical curves do not show the sharp break exhibited by the experimental values around 4 amps. This failure of the theory is typical. In addition, the asymptotic voltages calculated theoretically are usually too high by a factor of 1.5 to 2. Although some of these differences may be due to the simplifying

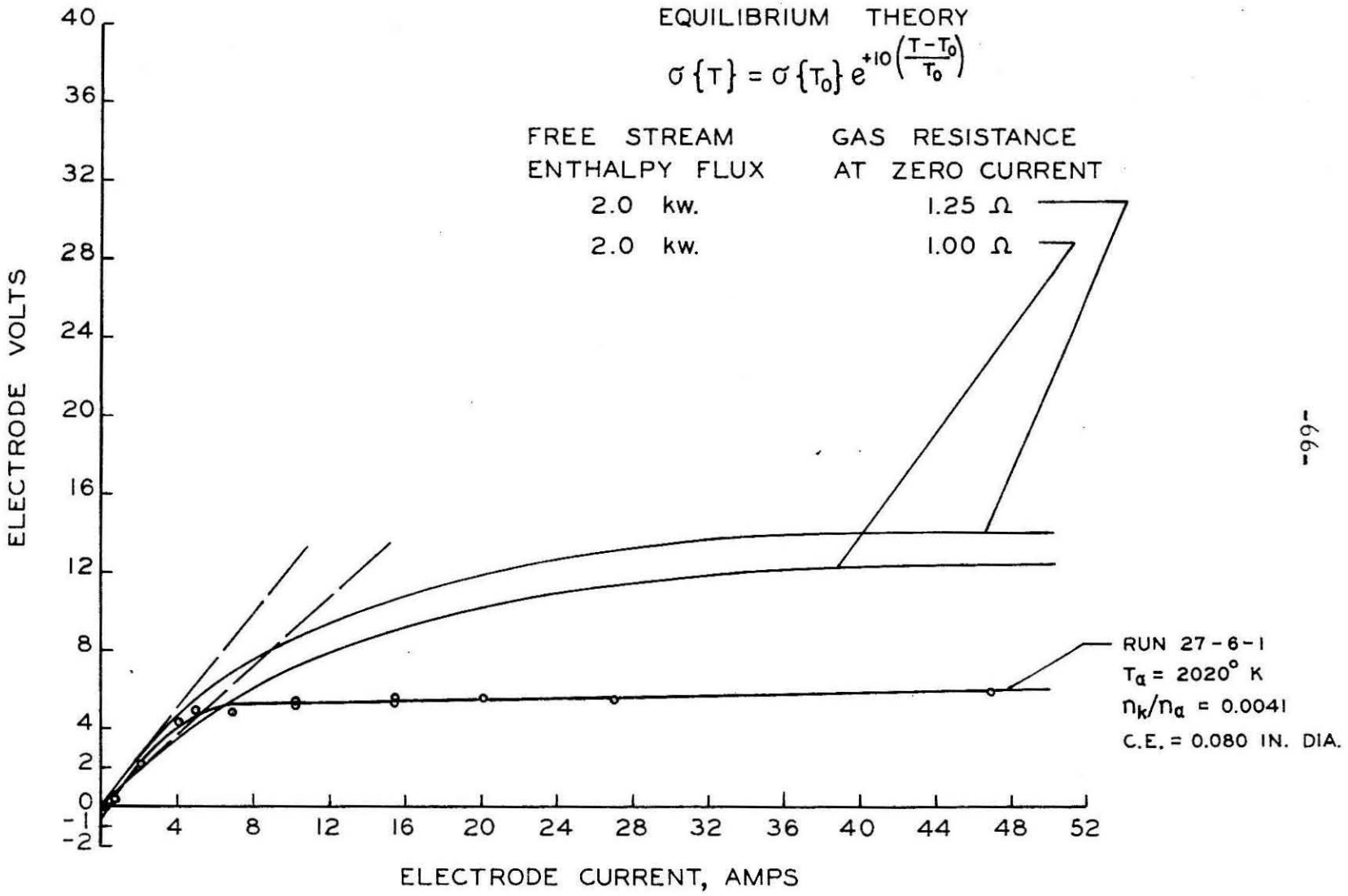

Figure 33. Theoretical and Experimental Voltage-Current Characteristics (Coaxial Geometry).

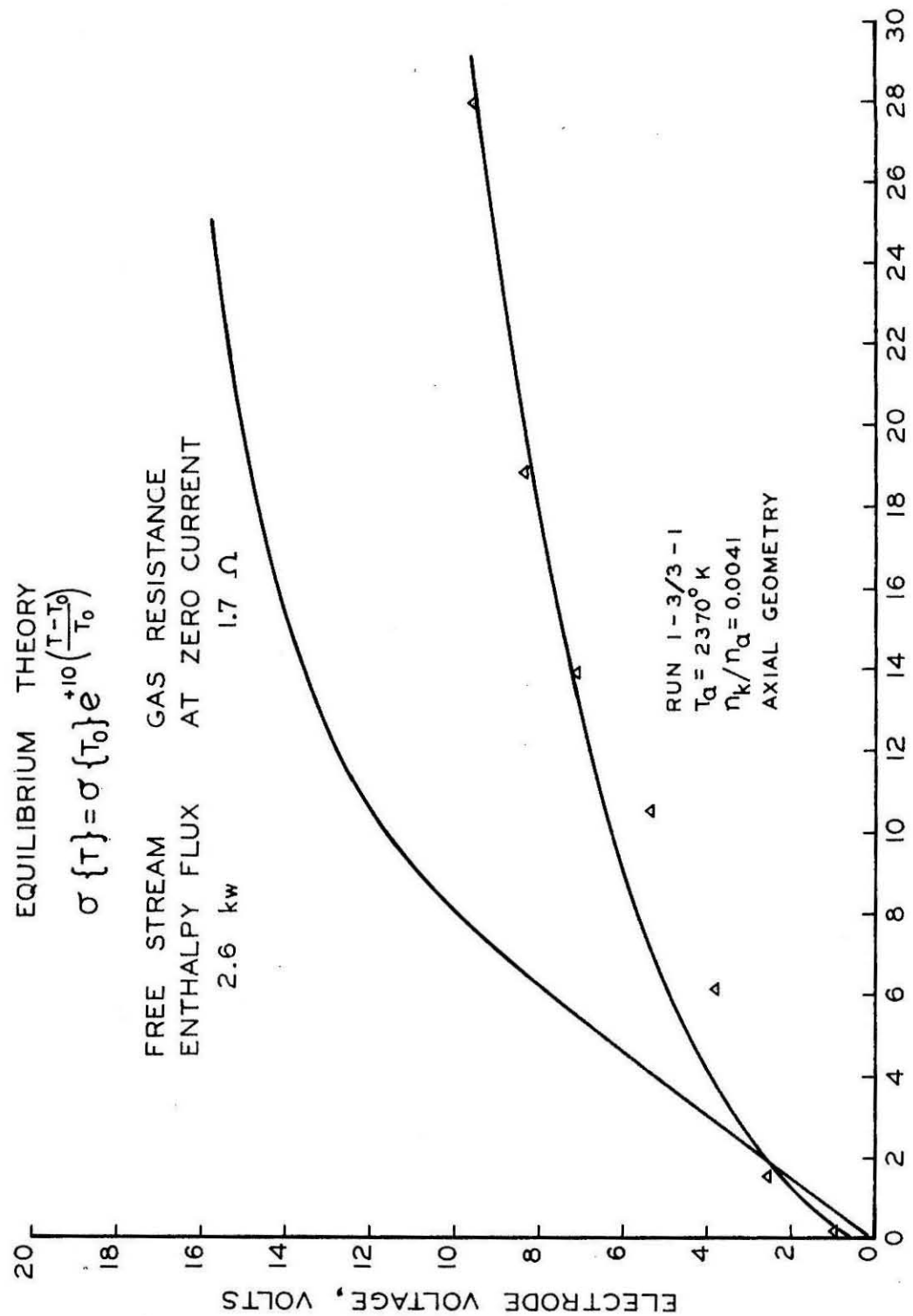

Figure 34. Theoretical and Experimental Voltage-Current Characteristics (Axial Geometry).

assumptions made in the theory, it is clear that agreement with experiments is not completely satisfactory. However, it is evident that simple equilibrium heating effects are quite important for the range of currents, voltages, and gas enthalpy fluxes used in these experiments. These effects must be properly accounted for in any complete theory.

(b) Non-equilibrium theory of current conduction. - While at the California Institute of Technology, Dr. Jack L. Kerrebrock developed the theory of "non-equilibrium" current conduction in seeded plasmas[1]. The problem considered is one in which a noble gas, such as argon, is "seeded" by injecting a readily ionized material, such as an alkali metal, in a ratio of approximately one mole per cent ($n_k/n_a \approx 0.01$). In Ref. 1, it is shown that under the flow conditions of these experiments, the current conduction phenomena are determined by the degree of ionization of the seed material and by elastic, electron-noble gas collisions.

Qualitatively, the non-equilibrium conduction theory can be considered in the following manner. The electrons "fall" through the electric field and obtain energy from it. They then proceed to lose this extra energy by means of relatively inefficient, elastic collisions. As a result, the mean energy of the electrons continues to increase until the rate of energy loss, which is proportional to ϵ_e, and the rate of energy gain from the field are equalized. The result of the elevated electron temperature is then to produce a greater degree of ionization, which in turn provides more conduction electrons, which increases the conductivity. A quantitative discussion of this current conduction theory will now be presented.

As the electrons drift in the direction of the applied electric field, they gain an increment of energy of eE per unit distance. The amount of energy lost when an electron collides elastically with a stationary atom is given by

$$\Delta\epsilon_e = \frac{2 m_e m_a}{(m_e + m_a)^2} \{\epsilon_e\} (1 - \cos \chi_{cm}) . \tag{13}$$

For a 90° deflection and $m_a \gg m_e$,

$$\Delta\epsilon_e \simeq \frac{2 m_e}{m_a} \epsilon_e . \tag{14}$$

When the atom is moving, however, the expression is more involved, and is usually expressed in the form

$$\Delta\epsilon_e = \frac{\delta m_e}{m_a} (\epsilon_e - \epsilon_a) , \tag{15}$$

where δ is on the order of unity for noble gases. δ is considered a parameter which must be determined from experimental data. Assuming that elastic collisions are the only major source of energy loss from the electrons, the following energy balance relation must hold:

$$\frac{d\epsilon_e}{ds} = eE - \frac{\delta m_e}{m_a} (\epsilon_e - \epsilon_a) , \tag{16}$$

where s is in the direction of the $\vec{E}$ field. Using the definitions $\vec{J} = \sigma\vec{E}$ and $\sigma = e^2 n_e / m_e \nu_c$ (Ref. 6), and solving for the asymptotic case $(d/ds \equiv 0)$ yields

$$\frac{\epsilon_e}{\epsilon_a} = 1 + \frac{m_a}{\delta\epsilon_a} \left(\frac{J}{en_e}\right)^2 . \tag{17}$$

This last relation indicates that the electron temperature varies with the square of the current density and inversely as the square of the electron density. Equation 17 will receive additional discussion with regard to experimental determination of the electron temperature.

Besides Eq. 17, Kerrebrock utilized two other basic relations in his theory. Ionization of the seed atoms was assumed to be given by the ordinary Saha equation, but with the usual temperature replaced by the elevated electron temperature.

$$n_e^2 = \left(\frac{4\pi m_e}{3h^2}\right)^{3/2} (n_k - n_a)\, \epsilon_e^{3/2}\, e^{-\frac{3}{2}\frac{\epsilon_i}{\epsilon_e}} \tag{18}$$

This use of the relation is justified by calculation of the pertinent electron -atom and electron-electron equilibration times. An elastic central impact of two particles of equal mass produces an exchange of velocity and kinetic energy. Thus, electrons will equilibrate themselves to a Maxwellian distribution in the time required for one electron-electron collision. Spitzer gives an expression for the mean electron-electron collision time:[6]

$$\tau_{e\text{-}e} = \frac{0.267\, T_e^{3/2}}{n_e \log \Lambda}\,, \tag{19}$$

where $\log \Lambda$ is given by Eq. 5. For the conditions of these experiments, $\tau_{e\text{-}e}$ is on the order of 10^{-10} sec.

An estimate for the electron-atom equilibration times can be obtained as follows. In a right-angle deflection, an electron loses an amount of energy $\Delta\epsilon_e \simeq 2m_e/m_a\ \epsilon_e$ (Eq. 14). The number of such collisions per unit time is obtained from the relation $\lambda = 1/n_a Q_a$ and the average velocity of the electron.

$$\bar{v}_e = \sqrt{\frac{8kT_e}{\pi m_e}} \tag{20}$$

Using a constant mean value for $\nu_{e\text{-}a}$, the electron-atom equilibration time is found to be on the order of

$$t_{e-a} = \frac{m_a}{2m_e} \left(\frac{\pi m_e}{8kT_e}\right)^{1/2} \frac{1}{n_a Q_a} \quad . \tag{21}$$

Assuming a constant, mean free path for the equilibration process yields

$$t_{e-a} = \frac{\sqrt{\frac{m_a^2}{2m_e}}}{n_a Q_a} \left(\frac{\sqrt{\epsilon_{e_o}} - \sqrt{\epsilon_a}}{\sqrt{\epsilon_{e_o} \epsilon_a}} \right) \quad . \tag{22}$$

In these experiments, t_{e-a} is on the order of 10^{-5} to 10^{-6} seconds. The calculations show that the electrons equilibrate sufficiently rapidly with themselves that they may possess a Maxwellian velocity distribution while still remaining at a temperature above that of the atoms. The very small cross section of the argon at these energies (the Ramsauer effect) aids in establishing such a situation.

The electron temperature is also employed in the expression for the electrical conductivity:

$$\sigma = \frac{e^2 n_e}{m_e \left(\frac{3kT_e}{m_e}\right)^{1/2}} \frac{1}{n_a Q_a + (n_k - n_e) Q_k} \quad . \tag{23}$$

A simplified derivation of the above equation follows from the relation $J = en_e u_d$ where u_d is the drift velocity of the electrons. On the average, the drift velocity should be $u_d = (eE/m)\tau$ where τ is the mean collision time, and from Eq. 20 it follows that $\tau = \left(1/\sum n_j Q_j\right)\left(\sqrt{\pi m_e/8kT_e}\right)$ if the electrons have a nearly Maxwellian velocity distribution. Hence

$$\sigma = \frac{e^2 n_e \sqrt{\frac{\pi}{m_e}}}{(8kT_e)^{1/2}} \frac{1}{\sum n_j Q_j} \quad , \tag{24}$$

which differs from Eq. 23 only by a small difference in the multiplicative constant.

With the three relations, 17, 18, and 23, it is possible to solve for n_e, ϵ_e, and σ as functions of the current density with n_k and ϵ_a as parameters. Reference 1 presents the results of solving these equations in a series of graphs. The pertinent material from this work will be introduced in a later section when the experimental results are discussed.

A common objection to Kerrebrock's non-equilibrium theory is the omission of electron energy loss by ionization and other inelastic collisions in Eq. 17. The validity of this objection may be surmised by estimating the fraction of the test section electrical power utilized in the ionization process. Energy is deposited in the ionization process throughout the test section conducting volume, at a rate given by

$$\dot{E}_i = \left[\oiint_A v_g \, n_e \, \phi_i \, dA \right]_1^2 \qquad (25)$$

where 1 refers to the test section inlet and 2 denotes the test section exit. The value of $\dot{E}_i$ is then to be compared with the product VI for the test section. A typical calculation based on $T_a = 2000^\circ K$, $n_k/n_a = .004$ and $I = 10$ amps yields the two values: $\dot{E}_i \cong 2.2$ watts and $VI \cong 33$ watts. The calculation of $\dot{E}_i$ was based on Kerrebrock's theoretical curves. In his experiments, he found it necessary to adjust his free parameters so as to reduce n_e for a given current density. Thus, the value of $\dot{E}_i = 2.2$ watts is conservatively high. Strictly speaking, the effect of ionization as an energy sink is of such a magnitude that it should be included in the theory. However, the accuracy of the present theory is sufficient for the purposes at hand.

In Ref. 1 mention is made of the effect of continuum radiation (bremsstrahlung) from the colliding electrons on the accuracy of the non-equilibrium theory. Kerrebrock states that this effect is not important for the conditions of the present experiment. However, in a recent discussion, Professor Kerrebrock has suggested that radiation caused by de-excitation of upper excited electronic states to other states above the ground state (non-resonance radiation) may be an important energy loss mechanism. It is then suggested that the value of δ may have to be suitably modified to account for this effect.

The problem of analyzing the data obtained with the coaxial electrode configuration is complicated by several factors which are due primarily to geometrical effects. In general, the current density varies inversely as the radial distance from the test section axis. This results in a Joule heating effect which varies strongly in the radial direction. Axial effects become important at larger currents as the gas at the test section exit becomes appreciably hotter than at the entrance. As a result, the conductivity varies both radially and axially. The resulting gradients in the electrical conductivity cause the electric field lines to distort so as to produce axial electric field components.

In view of the above difficulties, solution of the exact differential equations describing the aforementioned phenomena would be a most formidable task. However, if the problem is considered in view of the non-equilibrium conduction theory, several simplifications become possible, as will be shown below.

The first item is the question of the direction of the local electric field in the plasma. From the relation

$$\nabla \cdot \vec{J} = 0 = \nabla \cdot (\sigma \vec{E}) \ , \qquad (26)$$

it follows that

$$\nabla \cdot \vec{E} + \vec{E} \cdot \frac{\nabla \sigma}{\sigma} = 0 \qquad (27)$$

or

$$\nabla^2 \phi + \nabla \phi \cdot \frac{\nabla \sigma}{\sigma} = 0 \ . \qquad (28)$$

For the special case of $\nabla \sigma$ being always perpendicular to $\nabla \phi$, it is seen that ϕ then satisfies Laplace's equation and the resulting potential distribution is unaffected by the current. Such a situation could occur if σ varied only in the axial direction and the electric field was strictly radial. However, if $\nabla \sigma$ has a radial component, then, in general, $\vec{E}$ will possess axial components. Rough estimates of these axial fields indicate they may be on the same order of magnitude as the radial fields in some cases. In the limit of zero current, the measured radial temperature distribution (Fig. 24) indicated only a small decrease in the gas temperature in the radial direction. Thus, the effect of the $\nabla \phi \cdot \frac{\nabla \sigma}{\sigma}$ term can be neglected at low currents. Two important relations follow then at the low current limit. They are $\partial \vec{E} / \partial z = 0$ and $J(z) r = J_1(z) R_1$. The first relation results from the absence of axial electric fields and the assumption that the electrodes are equipotential surfaces. This results in radial electric fields only, and thus the current is in the radial direction only. This is expressed in the second relation above. The second point of consideration is the variation of the current density with axial distance down the test section for the case of small currents. The non-equilibrium theory then gives the following variation of the current density:

$$\frac{\partial \log J}{\partial z} = \alpha \frac{\partial \log J}{\partial z} + \beta \frac{\partial \log T_a}{\partial z} \qquad (29)$$

where

$$\alpha \equiv \frac{\partial \log \sigma}{\partial \log J}\bigg|_{T_a} \quad \text{and} \quad \beta \equiv \frac{\partial \log \sigma}{\partial \log T_a}\bigg|_{J} \tag{30}$$

Combining Eq. 29 with the free stream energy equation

$$\rho u c_p \frac{\partial T_a}{\partial z} = \vec{J} \cdot \vec{E} \tag{31}$$

yields

$$(1 - \alpha) \frac{\partial \log J}{\partial z} = \frac{\beta}{T_a} \frac{\vec{J} \cdot \vec{E}}{\rho u c_p} . \tag{32}$$

Multiplying both sides of Eq. 32 by $2\pi r dr dz$ and integrating over the test section volume gives

$$\log \frac{J}{J_o}\Big]_{R_1} = \frac{1}{\pi(R_2^2 - R_1^2)} \int_{z=0}^{L} \int_{R_1}^{R_2} \frac{2\pi r \beta \, J \cdot E}{(1-\alpha)\rho u c_p T} \, dr dz . \tag{33}$$

The right hand side of Eq. 33 is seen to vary directly with the total power added to the test section and inversely with the enthalpy convected into the test section by the gas. A reasonable approximation to $\log \frac{J_L}{J_o}\Big]_{R_1}$ for low power addition to the test section is given by

$$\log \frac{J_L}{J_o}\bigg|_{R_1} \cong \left(\frac{\beta}{1-\alpha}\right) \frac{\Delta T}{T_\infty} , \tag{34}$$

which can be written in the form

$$\frac{J_L}{J_o}\bigg|_{R_1} = e^{\left[(\beta/1-\alpha)(\Delta T/T_\infty)\right]} . \tag{35}$$

Equation 35 may be utilized to estimate how strongly the current density varies in the axial direction for various test conditions. It is readily seen that at zero current, no power is added to the test section

$\Delta T = 0$ and $J_L/J_o = 1$. At currents of 10 amps, J_L/J_o is about 1.25, and at 30 amps this ratio increases to about 3.5.

Thus, in analyzing the data in the following manner, it will be necessary to consider only data for which the power added to the test section does not appreciably affect the spatial uniformity of the gas properties.

With the above limitations in mind, and in view of the previous assumptions, it follows that

$$J/(\sigma(T, J)) = E = -\frac{d\phi}{dr} \quad \text{and} \quad J = I/2\pi rL \ .$$

Integrating the expression for Ohm's law gives

$$\int_{R_i}^{R_o} \frac{I}{2\pi rL} \frac{dr}{\sigma(T_a, J)} = -\int_{R_i}^{R_o} d\phi = \Delta V_{2-1} \ . \tag{36}$$

From Ref. 1, the relation between J and E is given by

$$J = e^{b(T_a)/1-\alpha} E^{1/(1-\alpha)} , \tag{37}$$

where

$$\alpha = \left(\frac{\partial \log \sigma}{\partial \log J}\right)_{T_a} . \tag{38}$$

For current densities above 5 amp/cm^2, α becomes independent of J and is a function of the argon temperature only. Thus α may be considered to be a constant in what follows.

From Eq. 37 it is seen that if the form $J = \sigma E$ is retained, then $\sigma = J^{\alpha} e^{b(T_a)}$, and ΔV is given by

$$\Delta V = \int_{R_i}^{R_o} \frac{I}{2\pi rL} \frac{e^{-b(T_a)}}{(I/2\pi rL)^{\alpha}} dr \tag{39}$$

and

$$\Delta V = I^{(1-\alpha)} \text{Const} \int_{R_i}^{R_o} \frac{e^{-b(T_a)}}{r^{(1-\alpha)}}\, dr \ . \qquad (40)$$

The integral in this last expression is a constant unless $T_a(r)$ changes with I. On a plot of $\log \Delta V$ versus $\log I$, the slope will differ from $(1-\alpha)$ by the term

$$\frac{d \log \int_{R_i}^{R_o} \frac{e^{-b(T_a)}}{r^{(1-\alpha)}}\, dr}{d \log I} = \xi \ .$$

Performing the differentiation,

$$\xi = \frac{I}{\int_{R_i}^{R_o} \frac{e^{-b(T_a)}}{r^{(1-\alpha)}}\, dr} \int_{R_i}^{R_o} \frac{e^{-b(T_a)}}{r^{(1-\alpha)}} \frac{d\left(-b(T_a)\right)}{dT_a} \frac{dT_a}{dI}\, dr \ . \qquad (41)$$

If we replace db/dT_a and dT_a/dI by suitable mean values, ξ becomes

$$\xi = \overline{\frac{db}{dT_a} \frac{dT_a}{dI}}\ (I) \ . \qquad (42)$$

Since db/dT_a and $dT_a/dI > 0$, it is seen that $\xi < 0$ in all cases. ξ represents the enhancement of the conductivity due to the gas temperature increase caused by Joule heating. The local slope on the $\log \Delta V$ versus $\log I$ curve should then be simply

$$\frac{d \log \Delta V}{d \log I} = (1 - \alpha) + \xi \ . \qquad (43)$$

As expected with $\xi < 0$, the Joule heating tends to reduce the slope given by the non-equilibrium effect acting alone.

Figure 35 is a plot of three voltage-current characteristics obtained at different gas temperatures. The experimental data of Kerrebrock's tests[1] are also shown. The agreement in the variation of the slopes with temperature is quite remarkable, as the data from Ref. 1 was obtained with a rectangular channel geometry.

Table III presents a comparison between the experimental slopes and the values predicted by the non-equilibrium theory. It is noted that the predicted slopes $(1 - \alpha)$ are much lower than the experimental values. If the effect of ξ (Joule heating) is included, the discrepancies between the experimental and theoretical values increase still further.

TABLE III

Comparison of Data with Non-Equilibrium Theory

Run	T_a (^oK)	n_k/n_a	$\left(\frac{d\log V}{d\log I}\right)_{exp}$	$\left(\frac{d\log V}{d\log I}\right)^*_{theory}$
22-5-1	2500	.0032	0.53	0.24
25-1-3	2210	.0041	0.34	0.22
8-2/3-1	1780	.0041	0.23	0.16

* based on $J = 10$ amp/cm^2.

In Ref. 1, Kerrebrock found a value of δ to be 3.47, which he attributed to the possibility of impurities in the system. Even if δ is changed from 2 to 4, the change in α is not appreciable for the

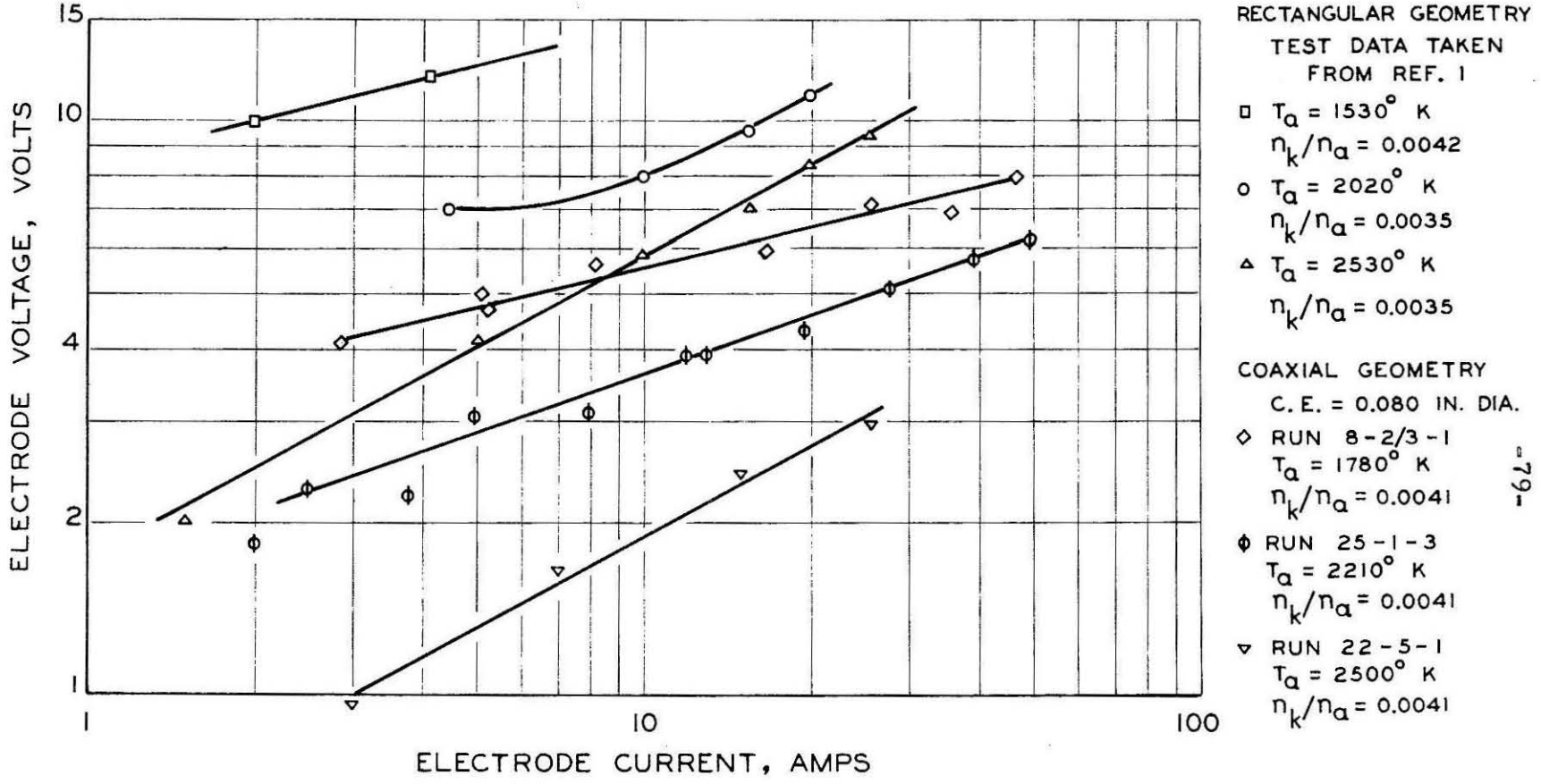

Figure 35, Logarithmic Voltage-Current Characteristics.

particular operating conditions of this experiment. As explained in Ref. 1, the value of α is determined solely by χ and ϵ_i/ϵ_a, where the quantity χ varies as the square of the current density.

$$\chi \equiv \frac{m_a}{\delta e^2}\left(\frac{3h^2}{4\pi m_e}\right)^{3/2}\left[\frac{J^2}{n_k\,\epsilon_a^{5/2}}\right] e^{\frac{3}{2}\frac{\epsilon_i}{\epsilon_a}} \quad . \tag{44}$$

Inspection of Fig. 36 indicates that changes in χ by a factor of two or so do not change α because the motion in the $\alpha - \chi$ plane is along the horizontal plateau of the curves for current densities greater than about 2 amp/cm^2.

At this point, it is appropriate to mention the effects of the electrode boundary layers on the resulting voltage-current characteristic. With operation in the normal mode and with the center electrode as the cathode, both electrode temperatures were several hundred $^{\circ}$C cooler than the bulk of the gas. Thus, in the cool boundary layers, both χ and ϵ_i/ϵ_a are varying parameters. However, decreasing temperatures result in increasing values for χ, and this only serves to move right along the plateau section of the curves in the $\alpha - \chi$ plane. As a result, the effect of the boundary layers in these particular experiments does not appreciably affect the slope of the log V - log I curve as far as the $(1 - \alpha)$ term is concerned. However, the boundary layer phenomena will alter the value of ξ and influence the V-I curves through the effects of Joule heating.

It is interesting to note that the slopes of the log voltage- log current curves remain essentially unchanged, even at the larger currents where the effects of Joule heating, gradients in the electrical conductivity, axial electric fields, etc., should become very important.

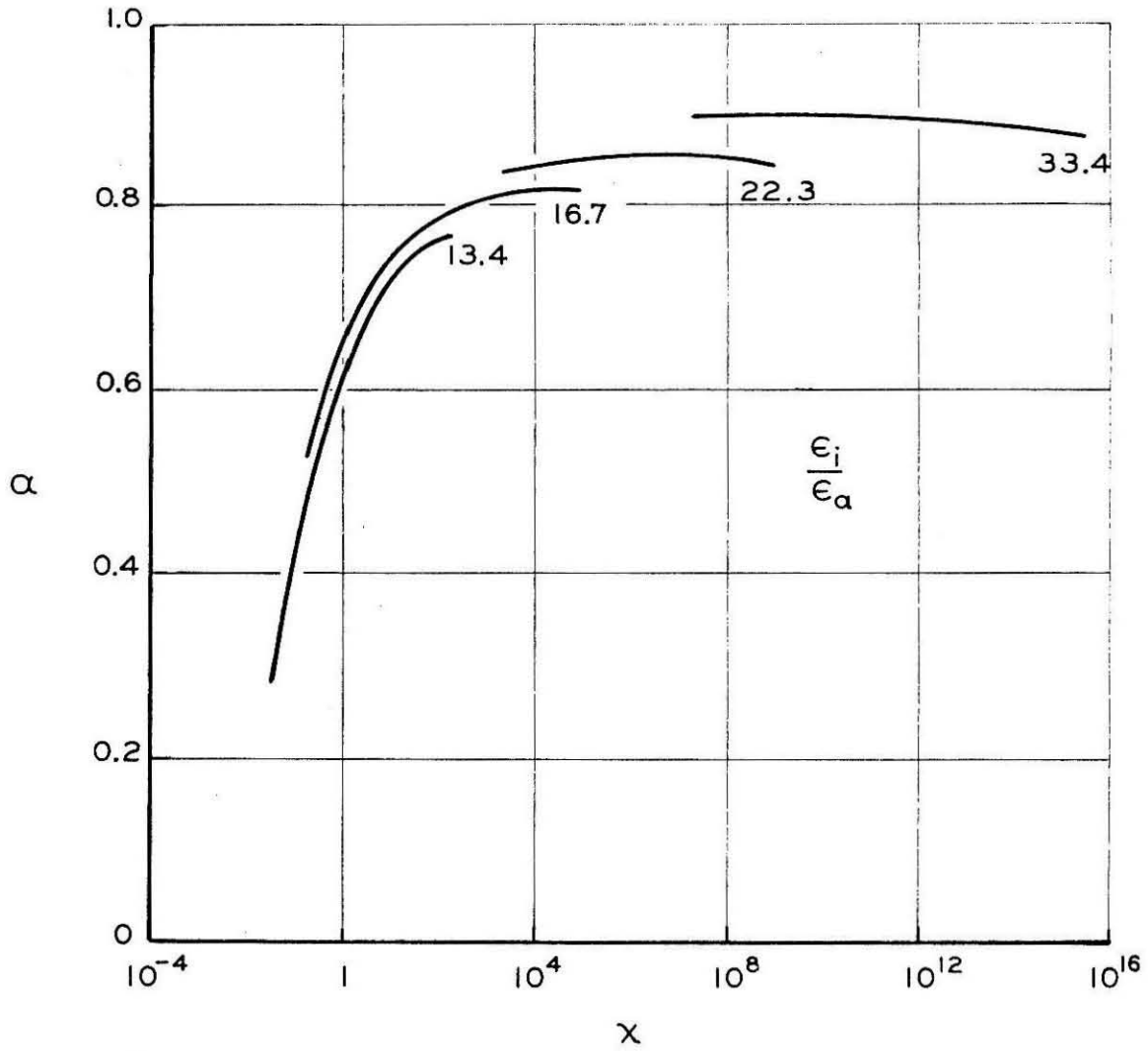

Figure 36. Conductivity Parameter $\alpha \equiv (\partial \log \sigma / \partial \log J)_{T_a}$ Versus Current Density Parameter χ.

In view of the effects just mentioned, a significant change in the slope would be anticipated as the test section power input becomes appreciable.

(c) Some comments on the two current conduction models. - Brief consideration will be given here concerning the question of the electron temperature in view of particle velocity distributions. In the section immediately following, the two models will be compared with some experimental data which are directly related to the electron temperature.

A further insight as to the conduction mechanism can be gained by examining the relative magnitudes of the mean electron drift velocities and the mean random velocities. This is equivalent to comparing the directed current density J to the random current flux $en_e\bar{c}_e/4$. If the equilibrium theory as well as the non-equilibrium theory is to be valid, then it is necessary that the directed current density be much less than the current density due to the random flux.

The previously mentioned restriction on the magnitude of J is required because both conduction theories are based on the assumption of a Maxwell-Boltzmann velocity distribution for the electrons. However, if the directed drift velocity of the electrons becomes an appreciable fraction of the mean thermal velocity, the distribution is distorted in velocity space along the direction of the drift velocity, and hence the distribution is no longer Maxwellian.

With the 0.080" diameter center electrodes, current densities of 50 amp/cm^2 and more were commonly observed. The simultaneously measured argon gas temperatures varied between 1800°K and 2000°K.

The equilibrium theory assumes that the electrons and neutrals are at the same temperature, while the non-equilibrium theory is based on an increase in electron temperature above the neutral temperature depending upon the magnitude of the current. Since the Saha equation is exponentially dependent upon the electron temperature in this latter case, the random currents predicted by the non-equilibrium theory far exceed the equilibrium assumption. See Table IV below.

TABLE IV

Gas Temperature	J_{rand}^{*} (Equilibrium)	$J_{rand}^{*\dagger}$ (Non-equilibrium)
1800°K	1.53 amp/cm^2	1010 amp/cm^2
2000	6.72	
2250	29.9	
2500	100	1200

* $n_k/n_a = .004$. † based on $J_{dir} = 10$ amp/cm^2.

The above table indicates that only the non-equilibrium theory is self-consistent in that it permits $J_{rand} \gg J_{dir}$ for the magnitudes of J_{dir} observed in the experiments. Although this simple comparison is not sufficient to validate the non-equilibrium theory, it still serves to indicate that the equilibrium theory by itself cannot furnish a complete picture of the process.

The original purpose of the sodium line reversal (SLR) temperature measurements was to develop a "direct" method of observing the elevated electron temperatures predicted by Kerrebrock's non-

equilibrium theory. The data will be compared to this theory first, and then a comparison will be made with the equilibrium point of view.

Qualitatively, it is readily seen that the SLR temperature should be related to the electron temperature. The SLR method measures the electronic excitation temperature of the transition responsible for the sodium D lines. This temperature, T^*, is defined by the ratio of excited sodium atoms to the number in the ground state,

$$\frac{n_1}{n_o} = \frac{g_1}{g_o} e^{-E_1/kT^*} , \qquad (45)$$

where g_1 and g_o refer to the statistical weights of the first excited state and the ground state of sodium, respectively. E_1 is the energy of the first excited level and is approximately 2.1 eV in the case of sodium.

The chief source of excited sodium atoms is the inelastic electron-sodium atom collision. The rate at which such collisions occur is, of course, dependent upon the electron temperature. If this temperature-dependent production rate of excited states is known and equated to the rate of de-excitation, then n_1 can be found, and hence a direct relationship may be found between T^* (SLR temperature) and T_e. In Appendix C, it is shown that under the conditions of these experiments, T^* and T_e are indeed equal ($T^* = T_e$). Thus, SLR temperatures given in Figs. 20 and 21 will be taken to be the electron temperatures.

From Eq. 3 of Ref. 1, the electron temperature is related to the other parameters in the system by

$$\frac{\epsilon_e}{\epsilon_a} \equiv \frac{\frac{3}{2}kT_e}{\frac{3}{2}kT_a} = 1 + \frac{m_a}{\delta\epsilon_a}\left(\frac{J}{en_e}\right)^2 . \tag{46}$$

However, this equation is not well suited for comparison with the experimental results, inasmuch as ϵ_a and n_e also change when J is varied. A more useful form is obtained by substituting $J = \sigma E$, where σ is given by Eq. 23. There results

$$\epsilon_e - \epsilon_a = \psi E^2/\epsilon_e , \tag{47}$$

where ψ is a factor which varies somewhat with E, but for the present purposes will be considered constant;

$$\psi \equiv \frac{1}{2\delta}\frac{m_a}{m_e}\frac{e^2}{\left(\sum_j n_j Q_j\right)^2} . \tag{48}$$

The next difficulty is the elimination of ϵ_a from Eq. 47, since ϵ_a changes due to Joule heating of the gas. For the case of the axial geometry, this can be done quite readily. The value of ϵ_a near the downstream edge of the test section is given by $\epsilon_a = \epsilon_{a_o} + \Delta\epsilon_a$;

$$\epsilon_a = \epsilon_{a_o} + \frac{\frac{3}{2}kL}{\rho u_\infty c_p}(JE) , \tag{49}$$

where ϵ_{a_o} is the appropriate value for zero current, $\Delta\epsilon_a$ is the increase due to Joule heating, and the assumed relations $J \equiv I/A$ and $E = V/L$ have been utilized. Thus, Eq. 47 can be solved by the quadratic formula to give

$$\epsilon_e = \frac{\epsilon_{a_o} + \Delta\epsilon_a}{2} + \frac{\epsilon_{a_o} + \Delta\epsilon_a}{2}\left\{1 + \frac{4\psi E^2}{(\epsilon_{a_o} + \Delta\epsilon_a)^2}\right\}^{\frac{1}{2}} \tag{50}$$

where $\Delta\epsilon_a$ is evaluated as in Eq. 49.

Another method of correlation was also utilized in analyzing the SLR results. In Ref. 1, an expression for ϵ_e/ϵ_a is developed,

$$\frac{\epsilon_e}{\epsilon_a} - 1 = \chi\left(\frac{\epsilon_a}{\epsilon_e}\right)^{3/2} e^{\frac{3}{2}\frac{\epsilon_i}{\epsilon_a}\left(\frac{\epsilon_a}{\epsilon_e} - 1\right)}, \qquad (51)$$

where χ has previously been given in Eq. 44, and ϵ_a is computed from Eq. 49. Figure 37, taken from Ref. 1, indicates the variation of $\frac{\epsilon_e}{\epsilon_a} - 1$ with the current density parameter χ. As previously mentioned, χ varies directly as the square of the current density.

In Fig. 38, the theoretical values of $(\epsilon_e - \epsilon_{a_o})$ computed from Eqs. 50 and 51 are compared with the experimental SLR temperature data. In the analysis utilizing the electric field as the independent parameter (Eq. 50), the local field was calculated simply from $E = V_e/L$ where V_e is the test section voltage and L is the electrode separation distance. The value of Ψ (Eq. 48) was based at first on a δ value of 3.47 and a value of the total cross section ($\sum_j n_j Q_j$) of 7.2×10^{14}, as previously suggested by Kerrebrock[1]. Computations based on these parameters gave values of $(\epsilon_e - \epsilon_{a_o})$ which were too high by a factor of three. After a later discussion with Professor Kerrebrock concerning the proper value of δ, the calculation was repeated for $\delta = 34.7$ (as a matter of convenience), and the resulting curve is so indicated in Fig. 38.

Use of such a large value of δ has no physical significance as far as energy transfer in elastic collisions between electrons and noble gas atoms is concerned. Increasing δ in such a manner is merely a crude attempt to account for other mechanisms which transfer energy from the electron gas. As previously mentioned, Kerrebrock attributes

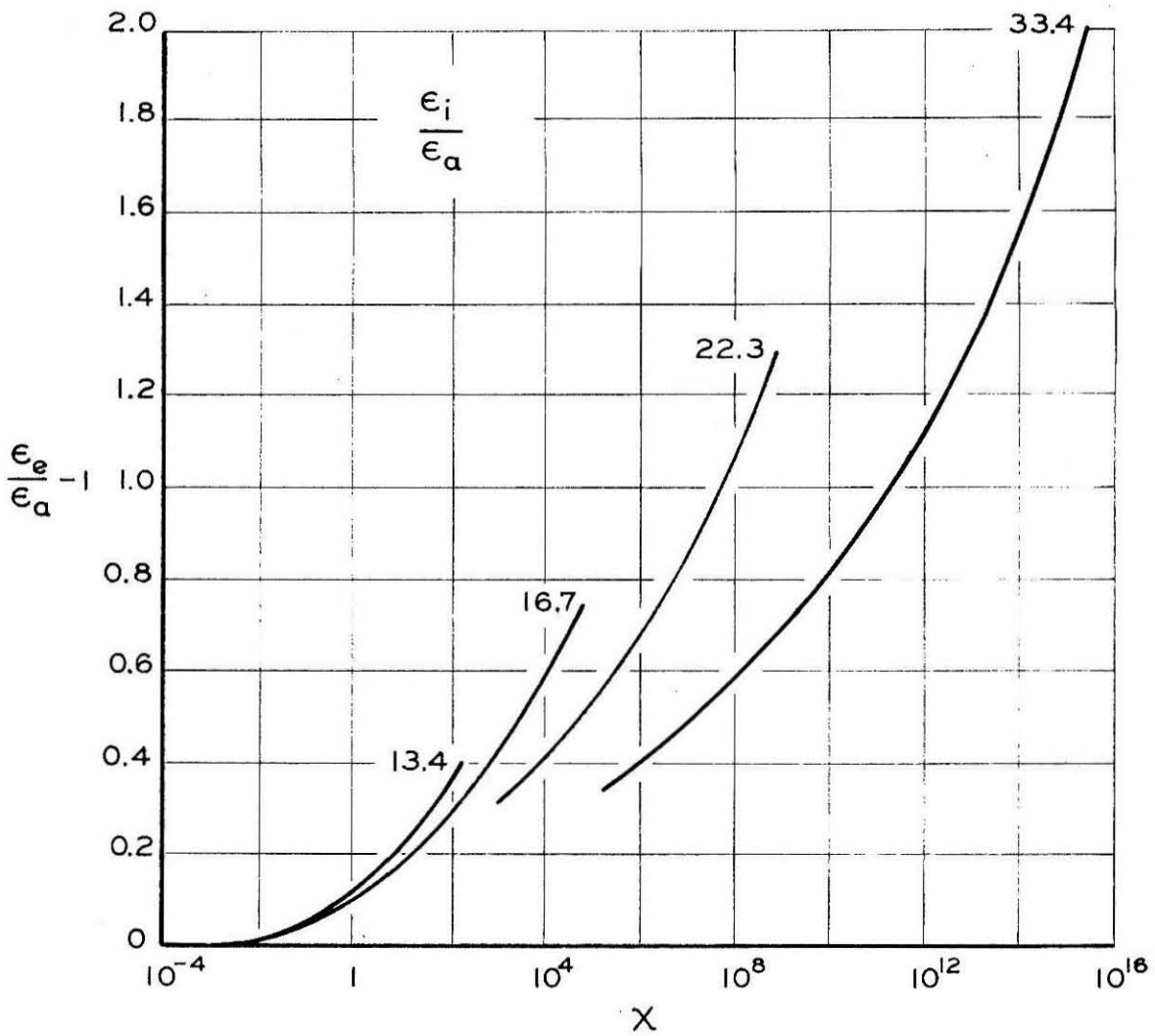

Figure 37. Normalized Electron Temperature Minus Unity Versus Current Density Parameter χ.

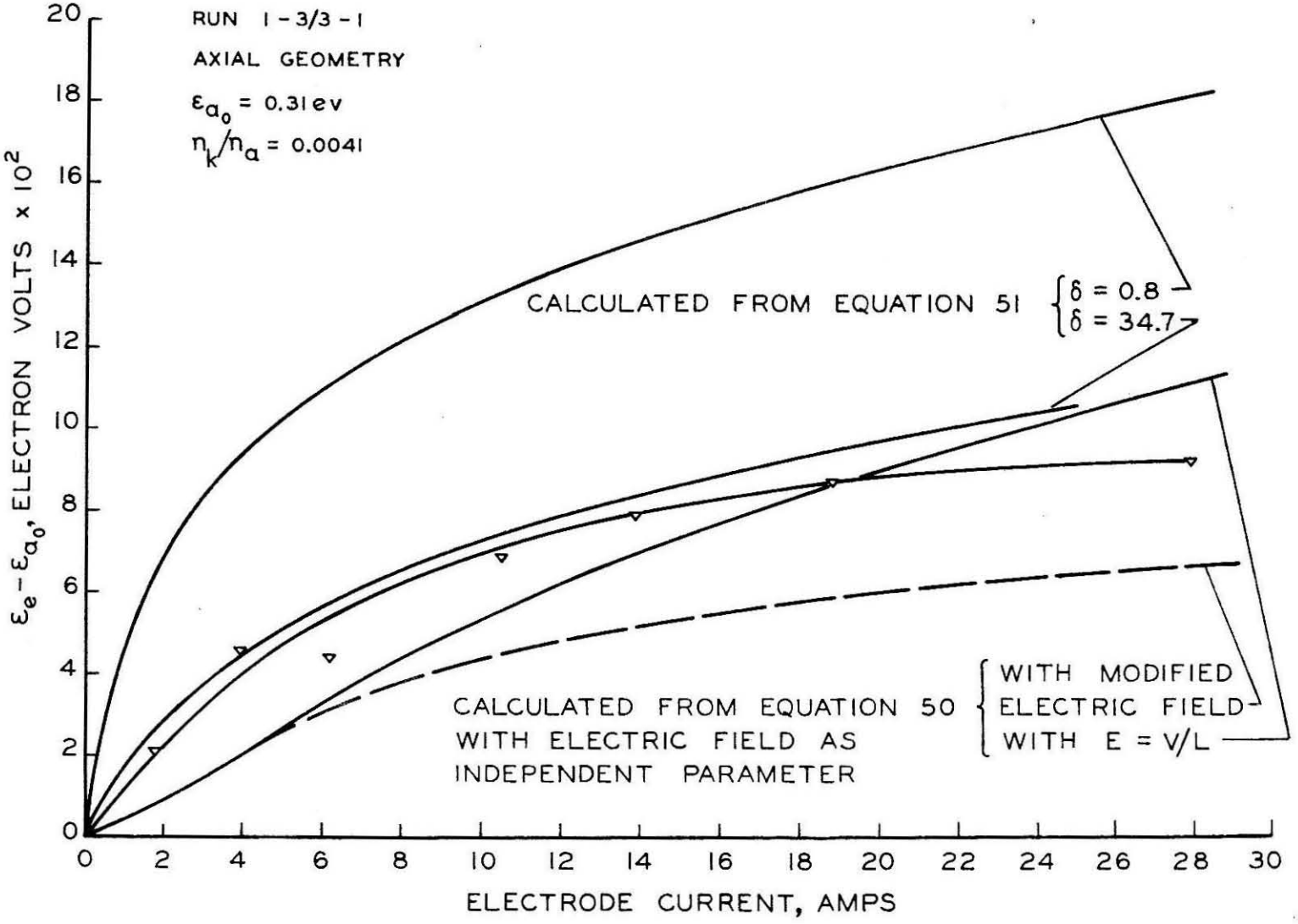

Figure 38. Electron Temperature Increase ($\varepsilon_e - \varepsilon_{a_o}$) Versus Electrode Current.

these large effective values of δ to non-resonance radiation from the upper excited electron levels of the gas atoms.

Use of the relation $E = V_e/L$ in computing the electric field near the end of the test section is not valid when Joule heating is present to change the conductivity by an appreciable amount in the axial direction. From $E = J/\sigma$ it is apparent that the E field at the downstream end of the test section will be less than V_e/L because of the increased conductivity at that location. A rough estimate of the appropriate value of E was then made. This procedure was based on using the Joule heating to compute a temperature rise with a resulting conductivity increase and then assuming a linear conductivity variation. Using these modified values of E in Eq. 50, a new curve was calculated and shown as the dotted line in Fig. 38.

It should be noted that the last curve is similar in shape to, but considerably below, the experimental curve. However, adjustment of the δ value or the total cross section would result in a displaced theoretical curve which could then be made to agree quite closely with the experimental data.

The two curves based on Eq. 51 indicate the strong effect of changing δ on this method of correlation. With $\delta = 34.7$, rather close agreement between the theoretical and experimental curves is obtained except at the high current values. In these computations, the value of J was based on the assumption of uniform current density across the duct. In view of the effects of Joule heating on the spatial distribution of the conductivity, this assumption is highly suspect, and the variation of the current density across the duct may thus account for the deviation of the aforementioned curves.

The equilibrium theory maintains that the electron and neutral temperatures are always equal. As a result, the increase in the measured SLR temperatures should be given simply by Eq. 49, where $\epsilon_a = \epsilon_e$. As the temperature rise is directly proportional to the Joule heating, the experimental SLR temperatures have been plotted against the electrical power dissipated in the test section (Fig. 39). The temperature increase predicted by Eq. 49 is also plotted there. The large discrepancy between the two curves clearly indicates that Joule heating alone is not sufficient to account for the observed SLR values.

C. Effect of Surface Phenomena

This section will consist of a discussion of the mechanism of transition to and operation in the current limited mode. It will be recalled that,by sufficiently increasing the current under normal mode conditions, a critical point was reached. Further attempts to increase the electrode voltage resulted in an abrupt decrease in the current. After this transition, the current was found to be essentially independent of the applied voltage. Figure 5 presents the voltage-current variations just described.

1. The transition process. - It is appropriate to begin with a qualitative discussion of the transition process. The interlocking effect of the electrical circuitry and the physical phenomena in the plasma will be considered first. This will be followed by several quantitative statements related to the physical processes involved in the plasma.

As shown in Fig. 5, the abrupt transition from the normal characteristic to the current limited mode resulted in a decreased current and an increased voltage. This relationship between voltage and

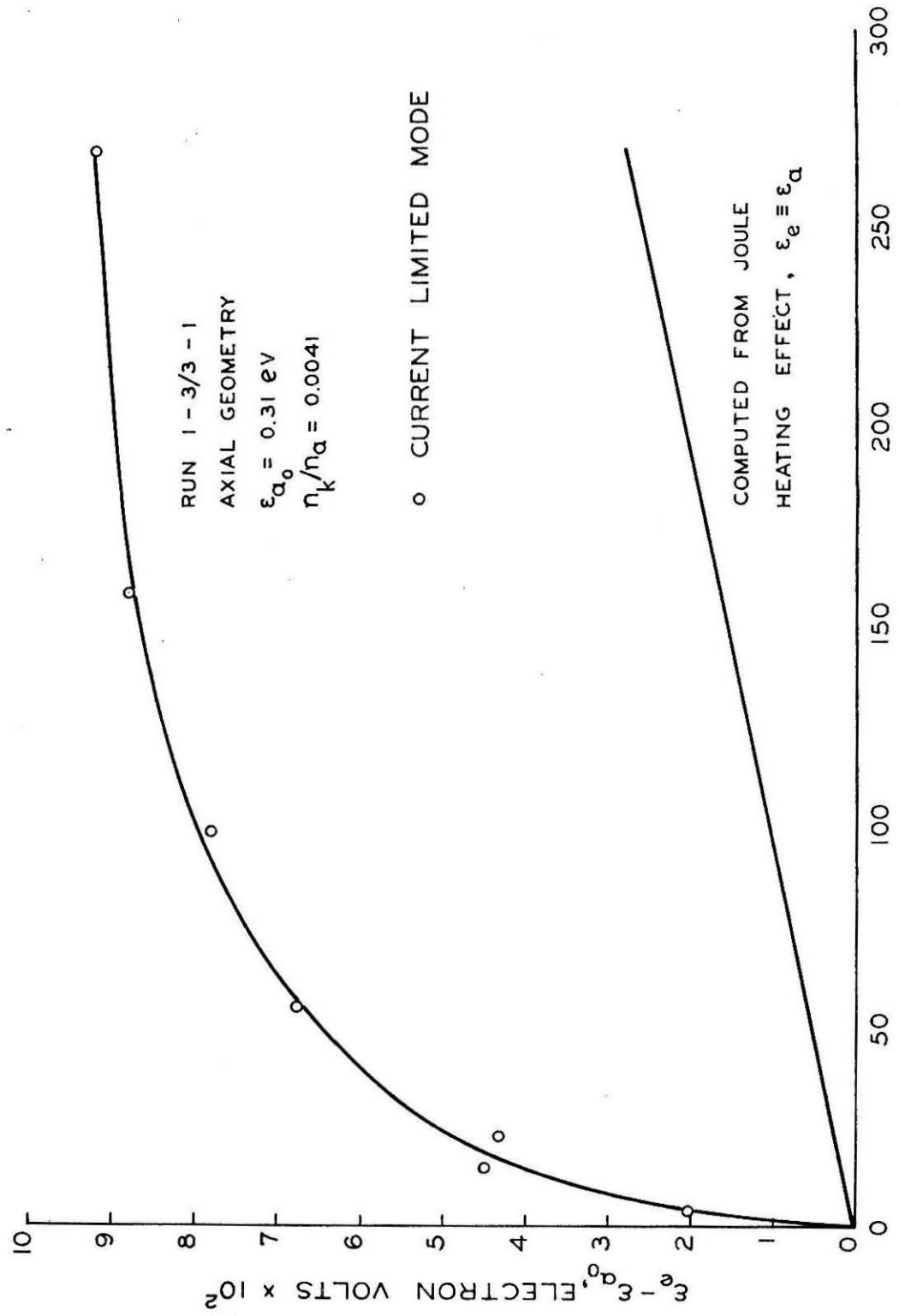

Figure 39. $\varepsilon_e - \varepsilon_{a_o}$ Versus Test Section Power Input.

current is anticipated in view of the presence of a ballast resistor in the external circuit. The circuit equation is given by Kirchhoff's law as:

$$V_e = V_{ext} - I_e R_{ext} \tag{52}$$

where V_{ext} is the battery voltage, and V_e is the electrode voltage which is related to the electrode current by some functional dependence

$$V_e = f(I_e) \ . \tag{53}$$

It is evident that a decrease in current will lead to an increase in voltage; this is exactly a curve of the type depicted in Fig. 5. Thus, in view of Eq. 52, the physically possible values of V_e and I_e must lie on the "load line" as depicted in Fig. 40. Reducing R_{ext} produces loci which more closely approach the horizontal.

It is of interest to study the physical mechanism which produces the reduction in current which then leads to the change from the normal mode of conduction to the limited mode. One piece of experimental data should be re-emphasized here: it was noted that the cathode temperature increased by 300 - 800°C when transition occurred.

Consider the case of the electrodes initially operating in the normal mode; when R_{ext} is reduced, the current increases until the thermionically limited current is reached. When the maximum possible current is being drawn from the cathode, the voltage drop across the bulk of the plasma cannot increase further. As a result, an additional increment in the applied voltage must appear across the sheath formed adjacent to the cathode surface. This situation is depicted schematically in Fig. 41.

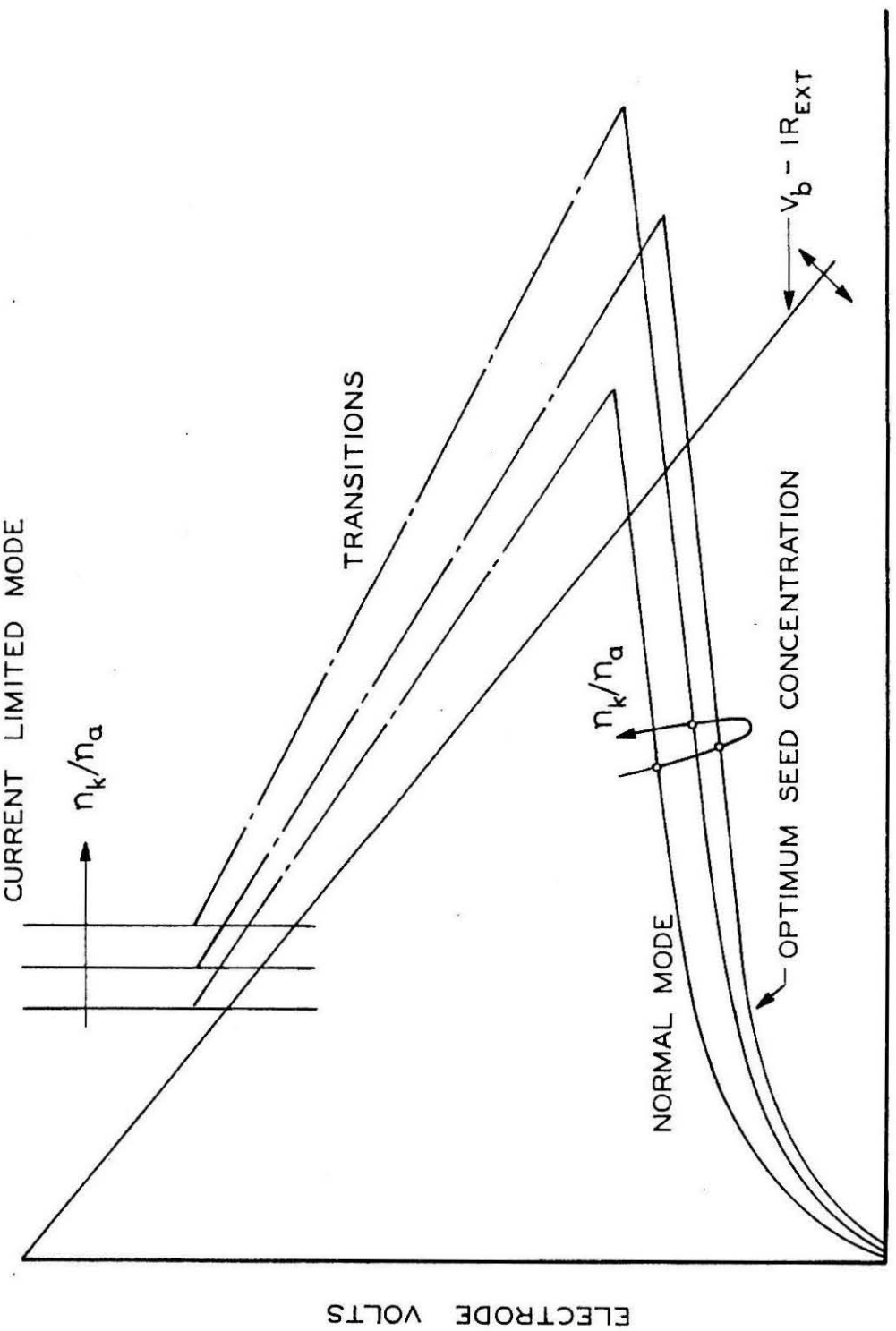

Figure 40. Schematic Voltage-Current Characteristics.

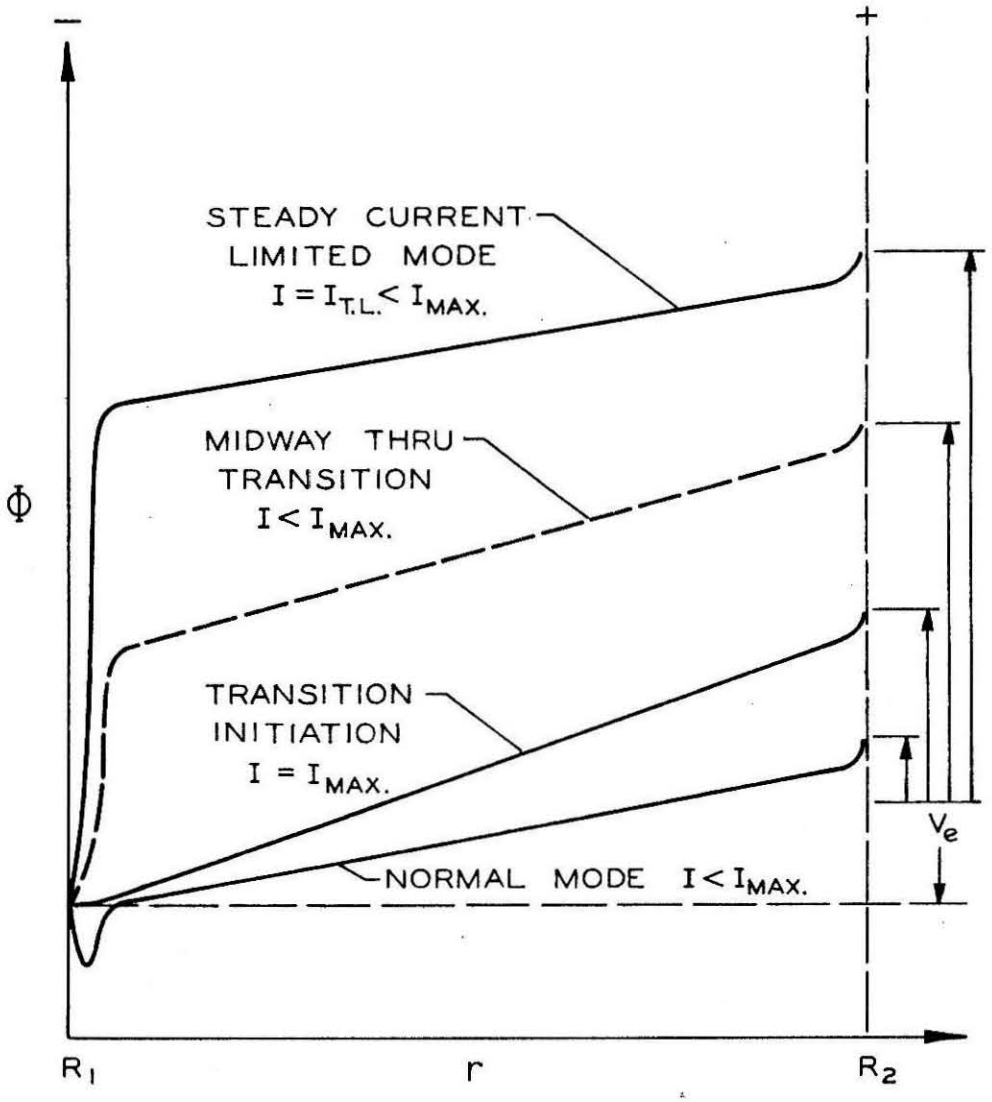

Figure 41. Sketch of Radial Potential Distribution in Plasma (Coaxial Geometry).

The emitted electrons, which have been accelerated by the sheath potential, are then thermalized by elastic collisions with the atoms and electrons in a region near the cathode.

Now the thermalizations of the electrons constitutes an energy source near the cathode, which results in the heating of the cathode. In turn, this increased cathode temperature produces a reduction of the fractional surface coverage of potassium. This results in an increased work function ϕ (Ref. 2) and a reduction in the thermionic current as indicated by Eq. 1.

The resulting decrease in the current produces a further increase in the sheath potential and thus an increase in the energy of the emitted electrons, which are accelerated by the sheath potential, ϕ_s. In the energy range from 1 to 10 eV, the cross section of the elastic electron-argon collision rapidly increases. Thus the heating effect increases with increasing sheath potential, because the strength of the heating source ϕ_s is increased, and simultaneously the effective distance of the heating source from the cathode is reduced. This interaction then continues to increase the cathode temperature until other competing mechanisms are sufficient to limit the temperature increase.

Radiation from the wire, which increases as T_w^4, and the cooling effect on the cathode of passing the electrons through the work function barrier both produce a heat flux out of the cathode. When the aforementioned heating and cooling effects reach a balance, a new stable operating condition is achieved. With this qualitative picture in mind, it is now proper to approach some aspects of the transition phenomena from a quantitative point of view.

A measure of the sheath thickness is given by the Debye shielding length[11].

$$L_D = (kT/4\pi n_e e^2)^{\frac{1}{2}} \tag{54}$$

For the conditions of the previously mentioned experiments, L_D is on the order of 10^{-5} cm, while the electron-atom mean free path is on the order of 10^{-2} cm. These calculations indicate the sheath is confined well within an electron mean free path. Hence the electrons which are emitted from the cathode surface will be accelerated to the velocity corresponding to the sheath voltage drop. In the steady current limited mode, this sheath drop is on the order of 10 - 20 volts, as may be noted from Figs. 5 and 8.

An estimate of the energy deposited per unit volume ($\dot{E}$) by the electron-atom thermalization process may be obtained by methods similar to those employed in the study of neutron thermalization[12]. The problem considered here is directly associated with the coaxial electrode geometry. Because of space limitations, only the result will be given below:

$$\dot{\epsilon} = \frac{J_L \phi_s}{4\pi\beta} e^{-r^2/4\beta} , \tag{55}$$

where $\beta = D/(\xi\Sigma)$ (see list of symbols in Appendix A). The details of this analysis may be found in Appendix D.

Equation 55 is obtained by considering only the effects of electron-neutral collisions and neglecting the effects of electron-electron and electron-ion collisions. The effect of the latter types of collisions is also treated in an independent manner. In a strict sense, it is not correct to try to analyze the physical situation by considering the different

types of collisions in a separate manner. However, to solve the problem in a complete way is an undertaking of rather large magnitude. Thus, the following approach was adopted to obtain some insight into the phenomena without the expenditure of an inordinate amount of effort.

From Eq. 55 it is seen that the major portion of the energy deposited by the colliding electrons occurs within a characteristic radial distance given by

$$r^* = (4D/\xi\textstyle\sum)^{\frac{1}{2}} \qquad (56)$$

where $D \approx 1/(3\textstyle\sum)$ for electrons diffusing through neutral atoms. Typical calculations based on Eq. 56 indicate that r^* is reduced from approximately 2 cm at $e\phi_s = \frac{1}{2}$ eV to 10^{-2} cm for $e\phi_s = 10$ eV.

Thus, as previously indicated, the heating effect increases with increasing sheath potential because both the strength of the heating source ($e\phi_s$) is increased and, simultaneously, the effective distance (r^*) from the heating source to the electrode is reduced. In addition, the maximum rate of energy deposition which occurs at the surface of the electrode ($r = 0$) also increases because β decreases as the square of the electron-argon collision cross section. With the aforementioned values of r^* in mind, the question of electron - charged particle interactions will now be considered.

As shown in Appendix D, the effect of electron interaction with other charged particles can be viewed in terms of an effective electron slowing down length. The computed values of this slowing down length were approximately 3×10^{-4} cm for 0.1 eV electrons and 0.6 cm for 10 eV electrons (see page 147). Comparing these values with the earlier mentioned values of r^* indicates that at large sheath potentials the

electron-neutral collisions predominate in thermalizing the electrons. This is why electron - charged particle interactions were overlooked in the previous discussion. At low sheath potentials the electron-electron and electron-ion collisions are the important factor. As a result, the electrons interact with themselves chiefly, and their resultant velocity distribution is relatively unaffected by electron-neutral collisions. Thus, these calculations support the viewpoint of the non-equilibrium conduction theory.

Another heat transfer mechanism which must be considered in the transition phase is associated with the production of ions near the surface by the high-energy sheath electrons. If a large number of ions were produced near the edge of the sheath, these ions would fall through the sheath potential and deliver a heating effect to the cathode equal to the sheath potential plus their ionization potential as they impact and recombine on the surface.

An estimate of the effective extent of the ionization region, produced by the sheath electrons, can be obtained by computing the effective mean free path for ionization. For potassium, the ionization cross section is given by[13]

$$Q_i = 4Q_m \left(\frac{\phi_i}{\epsilon_e}\right)\left(1 - \frac{\phi_i}{\epsilon_e}\right), \qquad (57)$$

where the maximum cross section $Q_m = 3 \times 10^{-6}$ cm^2, and it occurs at $\epsilon_e = 2\phi_i$. Based on the above value of Q_m, $n_k/n_a = .004$, and $T_a = 2000^\circ$K, the minimum mean free path for ionization is on the order of 3 cm. However, the total track length of the electrons as they slow down through the thermalization region is also on the order of 3 cm. Thus, at sheath potentials above the ionization potential, a region

of comparatively high ion concentration may exist at the edge of the sheath. During the transition process, when the sheath potential is below the ionization potential, the chief mechanism by which a portion of the energy of the sheath electrons is returned to the cathode is by electron-neutral thermalization collisions and subsequent ordinary $-K\frac{\partial T}{\partial r}$ neutral heat transfer back to the wire.

2. Operation in the current limited mode. - In view of the preceeding discussion, it is now of interest to estimate the magnitude of the various heat transfer mechanisms for operation at the upper stable point of the transition, i. e., the current limited mode. A typical case is Run 27-6-1 (Figs. 5 and 9). As the wire temperature was approximately 2400°K in the transition mode, the convective heat transfer to the bulk of the gas may be ignored. Thus, only a comparison between the radiation, electron cooling, and energy input to the sheath electrons need be considered.

It should be noted that the upper stable conditions is not one in which the tungsten cathode surface is completely bare. The magnitude of the thermionic currents obtained requires that the potassium fractional coverage be approximately 30 per cent.

Calculations from a typical run indicate that the surface work function (ϕ_{wf}) changes from a value of 2. 6 eV just prior to transition to a larger value, 3. 2 eV, in the current limited mode. The work function of bare tungsten is approximately 4. 4 eV.

The radiant heat transfer is approximately 54 watts, while the electron cooling is $\phi_{wf} I_{CLM} \cong 3.2\ (13) \cong 42$ watts, and the power imparted to the sheath electrons is approximately $\phi_s I = 14(13) = 182$ watts. If these three terms are equated as follows

$$\eta\phi_s I = \dot{q}_{rad} + \phi_{wf} I , \tag{58}$$

then η, which is the fraction of the energy of the sheath electrons which is returned to the cathode, is found to be approximately 0.5. A mental sketch of a reasonable gas temperature distribution in the CLM indicates this value of η is quite reasonable.

Figure 25 shows a reversal in the temperature gradient in the center electrode (coaxial geometry) just prior to transition. This reversed temperature gradient also occurs in the current limited mode. An explanation of this effect requires consideration of gas property variations and resultant current density variations which exist in the axial direction.

According to both the equilibrium and non-equilibrium conduction theories, the effect of Joule heating as the gas passes through the test section causes the conductivity to increase in the downstream direction. As a result, the current density also increases as the gas moves from the entrance to the exit of the test section. According to Eq. 21 of Appendix B, the equilibrium theory gives the following axial variation of the current density:

$$J(\tau) = \frac{2\nu}{\ell n \frac{\xi_2^2 + \beta}{1 + \beta}} , \tag{59}$$

where $\tau \equiv z/L$, ν is the non-dimensional electrode voltage, and $\beta(\tau) = \Gamma \int_0^\tau j^2(\tau) d\tau$. Appendix B gives the details for computing β.

The variation of current density in the axial direction as predicted by the non-equilibrium theory has already been considered, and the result is repeated here for convenience.

$$\log \frac{J(z)}{J_o}\bigg|_{R_1} = \frac{1}{\pi(R_2^2 - R_1^2)} \int_{z=0}^{z} \int_{R_1}^{R_2} \frac{2\pi r \beta \, J \cdot E}{(1-\alpha)\rho u c_p T} \, dr dz \quad (60)$$

Equations 59 and 60 show that as the total test section current is increased up to the transition point, the axial variation in the current density becomes increasingly pronounced. As previously shown, the non-equilibrium theory predicts a value of J_L/J_o about 3.5 for the large currents which occur just prior to transition. For the same experimental conditions, the equilibrium theory predicts a value of J_L/J_o which may be several times larger than the value quoted above for the non-equilibrium theory.

Upon the initiation of transition, the larger current densities near the exit of the test section provide a greater number of electrons per unit length of electrode. These electrons in turn provide a local heating effect of about $\frac{1}{2}\phi_s J$, as previously discussed. It is tacitly assumed here that the sheath potential does not vary appreciably in the z direction. Thus the local heating source (thermalization of the sheath electrons) is much stronger near the downstream section of the center electrode, and an inverse electrode temperature gradient results.

The increasing density of sheath electrons in the axial direction affects the free stream conductivity, by virtue of ionization, in such a manner as to augment further the original axial increase in current density.

D. Current Limited Mode

When operating in the current limited mode, the magnitude of the current is determined by the rate of emission of electrons from the

cathode surface. This statement is supported by several experimental observations. The vertical slope of the upper portion of the V-I curve in Fig. 5 shows that the current is independent of the applied voltage. This limitation of the current can occur only if there is some process in the system which limits the current.

The addition of nitrogen and helium and the presence of teflon contamination did not alter the magnitude of the current obtained in this second mode. This demonstrates again that the current is independent of gas phase phenomena.

As previously noted, the thermionic current density is given by the Richardson-Dushman equation

$$J = AT_w^2 e^{-\phi/kT_w} , \qquad (61)$$

where ϕ, the effective work function, is now dependent upon the amount of potassium adsorbed on the tungsten electrode surface. With an electrode system operating at a thermionic limit, a reduction in the electron emitting area will result in a proportional decrease in the current passing between the electrodes. The previously discussed "electrode switching" experiments, performed under conditions of current limited mode operation, are in exact agreement with the decrease in current predicted by Eq. 61.

As mentioned before, the magnitudes of the thermionic currents obtained in the second mode indicate that an appreciable fraction of the surface is still covered with adsorbed potassium. The work functions computed by the Richardson-Dushman equation varied between 3.0 and 3.4 eV. The work function of potassium is 1.9 eV, while that of bare

tungsten is 4.4 eV . For the case of cesium on tungsten, Taylor and Langmuir[2] found that the effective work function of the surface was that of cesium when the fraction of the surface covered (θ) with adsorbed atoms was approximately 0.60 . Figure 30 is taken from Ref. 2 and demonstrates the variation of ϕ_{wf} with θ . If a similar situation holds for potassium on tungsten, then a value of $\phi_{wf} = 3$ eV requires a θ value of about 0.35 if a linear relationship between ϕ_{wf} and θ is assumed.

In view of the above discussion concerning surface effects and the previous considerations of normal mode operation, it is now possible to properly explain the schematic voltage - current diagram given in Fig. 40 and the experimentally observed current variation shown in Fig. 27. Figure 40 is a schematic diagram of the V-I characteristics obtained when n_k/n_a is varied with all other parameters fixed. The spacing of the curves in the normal mode indicates an optimum seed concentration producing a maximum conductivity, as was observed here. Based on the experimental results, the increasing n_k/n_a produces a larger maximum normal mode current. This is also anticipated, since increasing n_k for a given T_w should tend to produce an increased fractional potassium coverage with resulting increase in the maximum thermionic current. The complete curve in Fig. 27 results from moving along the fixed load line of Fig. 40 by changing n_k/n_a and passing through both the normal and current limited modes.

It was found that increasing the seed concentration increased the thermionically limited current, as shown in Fig. 28. At first, this might be attributed to an increase in the fractional potassium surface coverage due to the increase in the number density of the potassium.

However, as shown in Fig. 29, the electrode temperature also increased with increasing potassium concentration. The overall result was an increase in the computed value of ϕ_{wf} with seed fraction. This result indicates that the increased temperature of the wire more than offset the increase in the potassium flux impinging on the cathode surface, and thus the fractional surface coverage decreased with increasing n_K. The variation of the experimental parameters is shown in a schematic way by the dotted line in Fig. 30.

The increase in electrode temperature due to adding potassium may be considered in light of the discussion given in the section on transition phenomena. It was shown there that the effective thermalization distance is inversely proportional to the macroscopic cross section. Thus, as previously explained, increasing the potassium concentration moves the effective heating source closer to the surface of the cathode, and thus the cathode temperature increases.

E. Electrode Heat Transfer

As previously mentioned, neither electrode was heated or cooled by an independent mechanism. Instead, the electrode temperatures were fixed by an energy balance between the various modes of heat transfer to or away from the electrodes. It is the purpose of this section to discuss the different heat transfer mechanisms independently of the current conduction model chosen, or which mode of conduction prevails.

In Ref. 1, the problem of heat transfer to the electrodes is considered for the case of small Mach numbers. In this analysis, the continuity and momentum equations are unchanged by the current. However, the energy equation for the gas has two additional terms due

to the electron flow.

$$\rho c_p \frac{DT}{Dt} = \nabla \cdot (K \nabla T + \frac{5}{2} kT_e \frac{\vec{J}}{e}) + \phi + \frac{J^2}{\sigma} \qquad (62)$$

The term containing T_e is seen to produce a difference in the heat transfer rates in the gas and hence to the two electrodes, too. Due to this term, the electrons heat the anode and cool the cathode by virtue of the energy flux which they transport.

Figure 9 shows the variation of the center electrode temperature for both current polarities. As previously mentioned, these temperatures were measured by means of a conventional optical pyrometer. The large increase in temperature with negative current coupled with the slight decrease (in some cases) for positive currents establishes the fact that the current conduction does produce asymmetrical heat transfer rates. The temperature increase for positive currents in Fig. 9 was typical of voltage - current characteristics which transformed from the normal mode to the current limited mode. Observations of the double-wire electrode geometry also indicated a very marked heating of the anode at high currents. However, a few simple calculations quickly indicate that the $\frac{5}{2} kT_e$ term is not sufficient to account for the observed data. The item of importance here is, instead, the work function barrier of the electrode surfaces.

When an electron is emitted from a surface, it moves into a region of higher potential energy by virtue of its having overcome the attractive image forces[14]. In a steady state condition, this emitted electron is replaced by an electron conducted in from the external circuit. This replacement electron possesses a mean energy which is approximately equal to the Fermi energy. As a result, the metal must

lose an amount of energy equal to $e\phi_{wf}$ for each emitted electron. This situation would be depicted in Fig. 42 if the cathode drop V_c were set equal to zero. The reverse process occurs when the electron enters the surface and the material is heated.

An energy balance for a differential element of the center electrode (coaxial geometry) gives the following relation:

$$K_w \frac{\partial T}{\partial r}\bigg|_{R_1} + \frac{4I_w^2(z)}{\sigma\pi^2 D_w^3} = -\frac{D_w}{4}\frac{d}{dz}\left(K_w \frac{dT_w}{dz}\right) \qquad (63)$$

where the first term represents the thermal energy conducted into the wire from the surface, while the second term represents the Joule heating within the electrode itself. These terms are equated (in steady state operation) to the net axial heat loss along the electrode as given by the right hand side of Eq. 63.

The effective heat transfer rate at the electrode surface may be obtained with the aid of Fig. 42. As shown in this figure, the location (1) refers to conditions inside the electrode, and this position may be moved arbitrarily close to the surface of the electrode. The position (2) refers to conditions in the plasma proper where collisional effects predominate and it is meaningful to speak of electron and ion temperatures, etc.

By considering an energy balance for an imaginary volume bounded by (1) and (2) and having unit cross-sectional area in a direction perpendicular to the surface, an exact expression may be derived for the surface heat transfer rate. Energy is delivered to this imaginary volume by the following mechanisms: the total current J passing through the net effective potential $\phi_w - V_c$, ordinary thermal conduc-

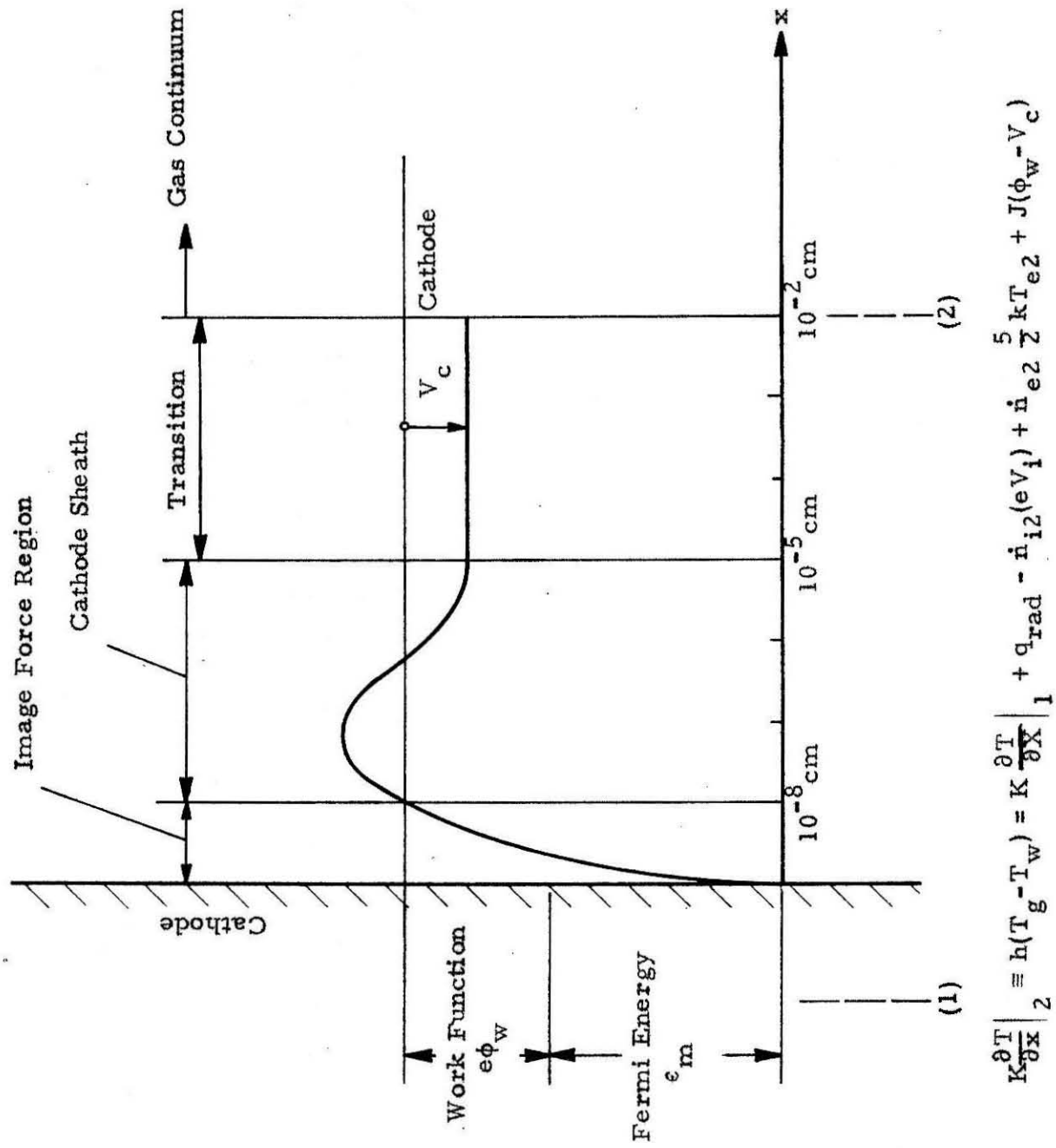

Figure 42. Schematic Diagram of Potential Distribution Near Cathode Surface.

tion from the gas ($K_a \left.\frac{\partial T}{\partial r}\right|_2$), and recombination of ions at the surface ($-\dot{n}_{i_2} eV_i$). Transport of energy out of this volume is accomplished by the following mechanisms: thermal radiation from the electrode surface and net transport of ions, electrons, and neutrals from the volume ($-\dot{n}_i\Big|_2 \frac{5}{2} k T_{i_2}$, $-\dot{n}_{e_2} \frac{5}{2} k T_{e_2}$, $-\dot{n}_{a_2} \frac{5}{2} k T_{a_2}$). Applying the principle of conservation of mass to the volume requires that $\dot{n}_{a_2} = -\dot{n}_{i_2}$ for a steady state. If the ion and neutral temperatures are taken to be equal in the gas, then the net effect of ion and neutral transport is zero.

By combining the above terms with the appropriate signs, the following equation results.

$$-K_w \left.\frac{\partial T_w}{\partial r}\right|_1 = q_{rad} - \dot{n}_{i_2} eV_i + \dot{n}_{e_2} \frac{5}{2} kT_{e_2} + J(\phi_w - V_c) - K_a \left.\frac{\partial T_a}{\partial r}\right|_2 . \quad (64)$$

In a steady state condition with no net recombination or ionization per unit volume, the ratio of $\dot{n}_i$ and $\dot{n}_e$ is on the order of the ratio of m_e over m_i, which is approximately 1/74,000. Since V_i is 4.34 eV and $\frac{5}{2} kT_i$ is on the order of a few tenths of an eV, it is safe to neglect the term associated with $\dot{n}_i$. The only exception to neglecting the $\dot{n}_i$ term is a case in which a region of large ion density existed just at the edge of a large surface sheath which then accelerated the ions toward the surface and caused them to impinge upon the surface with a large kinetic energy. The possibility of such a situation was considered in the discussion of the transition phenomena and the current limited mode.

As previously discussed, the sheath potentials obtained while operating in the normal mode are comparatively small. Thus, in the following analysis of the normal mode heat transfer data, the $\dot{n}_i$ term

will be neglected.

The effect of the various current conduction theories will affect the heat transfer correlation only in the $K_a \left.\frac{\partial T_a}{\partial r}\right|_2$ term. Depending upon the conductivity values chosen for the boundary layer, the resulting Joule heating in the gas will have a different value. This difference in the Joule heating will produce a different temperature gradient near the electrode surface , and consequently will change the heat transfer rate.

Combining Eqs. 63 and 64 yields the relation required to compute the axial temperature distribution in the wire. Because of the complexity of the resulting equation, this method was not utilized in the analyses of the experimental results. A simpler procedure based on quantities averaged in the axial direction was utilized and is presented below.

With the test section operating in the normal mode, the three dominant heat transfer terms are convection, electron heating or cooling, and radiation. Two other terms of somewhat lesser importance must also be considered; they are ohmic heating and thermal conduction in the electrode.

The data was analyzed by computing the various heat transfer terms and equating the net result to the convective term. A heat transfer coefficient was then computed based on a mean gas temperature near the wall, computed by the equilibrium theory (see Appendix B), and the mean wall temperature

$$h \equiv \dot{q}_{conv} / \{A_s (\bar{T}_g - \bar{T}_w)\} \quad . \tag{65}$$

The various heat transfer terms were determined in the fol-

lowing manner. For the given coaxial geometry of these tests, the net radiant heat flux from the cathode is given by

$$\dot{q}_{rad} = A_1\sigma\epsilon_1[T_1^4 - F_{12}\epsilon_2 T_2^4]$$

$$-\sigma A_1 F_{12} F_{21}\left\{\frac{\epsilon_1^2 T_1^4(1-\epsilon_2) - \epsilon_1\epsilon_2 T_2^4(1-\epsilon_1)(1-\epsilon_2)F_{12}}{1-(1-\epsilon_1)(1-\epsilon_2)F_{12}F_{21}}\right\} . \qquad (66)$$

The last term in Eq. 66 accounts for radiant energy reflected by the outer electrode back to the inner electrode. Because of the configuration factors involved, this term was in all cases a negligible quantity. Configuration factors were computed using the standard methods described by Jakob[15]. The emissivity of the center electrode was assumed to be that of pure tungsten. Temperature variation of the tungsten emissivity with temperature was obtained from Ref. 16. The emissivity of the stainless steel outer electrode was taken as 0.55 from McAdams[17].

Electron heating or cooling was computed for two values of $[\phi_w - V_c]$ = 2 eV and 3 eV, and the expression

$$\dot{q}_{electron} = \phi_{eff} I . \qquad (67)$$

These values are based on estimates of ϕ_w obtained by use of the Richardson-Dushman equation and the currents measured at transition from the normal mode. Again it is assumed that V_c is negligible in the normal mode.

Ohmic heating due to current conduction in the center electrode was computed from a mean value of the tungsten electrical conductivity[16] and by assuming a uniform emission current density from the center electrode. Based on these assumptions, the total Joule

heating in the center electrode becomes

$$\dot{q}_{J.H.} = \frac{1}{3}\frac{I^2 L}{\bar{\sigma}_T A_c} \quad . \tag{68}$$

Two electrode temperature measurements were taken near the tip of the center electrode and near the end of the test section. From these two numbers and a mean value of the thermal conductivity of tungsten[18] the thermal conduction losses from the center electrode were estimated by the relation

$$\dot{q}_{T.C.} = \bar{K}\frac{\Delta T]_o^L}{L} \quad . \tag{69}$$

The results of these calculations are given in the following table.

TABLE V.

Reduced Heat Transfer Data*

J (amps/cm^2)	T_{wall} °K	T_{gas} °K †	$h\{\phi_{eff}=2\text{ volts}\}$ watts/cm^2 °K	$h\{\phi_{eff}=3\text{ volts}\}$ watts/cm^2 °K
0	1780	2370	.027	.027
5.5	1712	2490	.028	.035
10.6	1697	2570	.037	.049
18.1	1692	2720	.045	.063
23.0	1683	2810	.047	.068
29.0	1659	3009	.047	.068

* Data taken from Run 24-5-2 † Estimated

A comparison of the above h values was made with the value for a flat plate (laminar flow)

$$h_{fp} = \frac{\bar{K}}{L}(0.332)(Pr)^{\frac{1}{2}}\sqrt{Re_L} \tag{70}$$

which for the conditions of the aforementioned test is 0.0135 watts/cm^2 ^{o}K. The value of h calculated for zero current is roughly twice the value obtained for a flat plate. This factor of two is quite reasonable in view of the circular cross section of the electrode and its small length-to-diameter ratio of about 6.

Examination of the h values indicates that the heat transfer coefficient increases with increasing current densities. The data indicate that an increase by a factor of 2 or 3 is produced by a current density of 30 amps/cm^2. This change indicates that the Joule heating of the thermal boundary has an appreciable influence on the heat transfer rate to the wall.

The results of this section indicate that Joule heating in the gas boundary layer may appreciably affect the electrode heat transfer, especially at the larger currents. However, it should be emphasized that the well known,but sometimes overlooked, heating or cooling effect of the passage of electrons through the surface work function barrier is usually of equal or greater importance.

F. Conclusions

Two modes of steady current conduction have been found for current flow between high temperature electrodes in a potassium-seeded argon plasma. In the first, or normal, mode, the conduction phenomena are dominated by gas phase effects. The conduction in the second, or current limited, mode is determined primarily by surface effects.

It should be stressed that in both modes of conduction, electron emission from the cathode is apparently by the thermionic process. In the first mode, the current density at the electrode surface is less than

the thermionic limit, and cathode sheath potentials are less than a few kT_w. In the second mode, the current density is equal to the thermionic limit, and sheath potentials are orders of magnitude greater than kT_w.

The transition between the two modes is produced by the increase in heat transfer associated with the sheath potentials, which may be large when the current is thermionically limited. Although the abrupt change in voltage which occurs at transition is a result of the use of uncooled electrodes in these experiments, both modes would still exist for constant temperature electrodes.

Interpretation of voltage - current data for the normal mode indicates that both Joule heating and some non-equilibrium process must be taken into account to explain the high conductivity values which were experimentally observed. The data obtained during the transition process and in current limited mode operation agrees well with the behavior anticipated in view of Langmuir's work concerning surface adsorption of alkali metals on tungsten.

Heat transfer phenomena are strongly influenced by electron cooling or heating effects. In the normal mode, the most important term appears to be the energy loss or gain associated with motion of electrons through the surface work function barrier. In the current limited mode, the dominant factor is the thermalization of emitted electrons, which have been accelerated by the large cathode sheath potentials.

APPENDIX A

Notation

A	electron emission constant (60. 2 amp/$\lceil cm^2\ ^oK\rceil$)
Å	angstrom
A_c	cross-sectional area of center electrode
A_s	surface area
A_1	surface area of inner electrode
$\vec{B}$	magnetic induction (field strength)
c_p	specific heat at constant pressure
$\bar{c}$	average velocity
$\bar{c}_e$	average electron velocity
c^2	velocity of light squared
C. E.	center electrode
D	diffusion coefficient for electrons
D_w	center electrode diameter
D/Dt	convective derivative
E	electric field magnitude
$\vec{E}$	vector electric field
$\dot{E}$	energy deposited per unit time per unit volume by electron thermalization
E^*	energy of excited electronic state above the ground state
e	electronic charge, base of natural logarithms
exp	experimental
F_{12}	configuration factor for radiant heat transfer
F_{21}	configuration factor for radiant heat transfer
f	oscillator strength

f_{0-1}	oscillator strength for resonance photon absorption
$f(\vec{r}, \vec{v}, t)$	velocity distribution function in phase space
g_o	degeneracy of electronic ground state
g^*	degeneracy of electronic excited state
h	Planck's constant, heat transfer coefficient
h_{fp}	heat transfer coefficient for flat plate
I	current
I_w	current in center electrode
i	non-dimensional current
J	current density (amp/cm^2)
J_{dir}	current density due to mean drift of charged particles through the plasma in the direction of the electric field
J_{rand}	current density associated with random motion of charged particles
J_L	current density at downstream end of center electrode (amp/cm^2), current density per unit length of center electrode (amp/cm)
J_o	current density at upstream edge of center electrode (amp/cm^2)
J_1	current density at surface of inner electrode (amp/cm^2)
$\vec{J}$	vector current density
j	non-dimensional current density
K_a	gas thermal conductivity
K_w	thermal conductivity of center electrode
^oK	degrees Kelvin
$\bar{K}$	mean thermal conductivity of tungsten
k	Boltzmann's constant
L	electrode length
L^*	characteristic length for absorption of resonance radiation

m_a	mass of argon atom, mass of neutral atom
m_e	mass of electron
$\dot{m}$	gas mass flow rate
m_l	mass of field particles
n_a	number density of argon atoms ($1/cm^3$)
n_e	number density of electrons
n_k	number density of potassium atoms
n_K	number density of potassium atoms
n_{Na}	number density of sodium atoms
$n_{Na(o)}$	number density of sodium atoms in ground state
$n_{Na(*)}$	number of sodium atoms in first excited electronic state
n_o	number of atoms in ground state,
n^*	number of atoms in excited electronic state
$\dot{n}_a$	net flux of neutral atoms ($1/[cm^2 sec]$)
$\dot{n}_e$	net flux of electrons
$\dot{n}_i$	net flux of ions
opt	optimum
Pr	Prandtl number
P_w	spectral absorption coefficient ($cm^{-1} atm^{-1}$)
p	impact parameter for two-body collisions, pressure in atmospheres
Q_a	electron-argon collision cross section
Q_k	electron-potassium collision cross section
Q_K	electron-potassium collision cross section
Q_{Na}	electron-sodium collision cross section
$Q^*_{0\rightarrow 1}$	electron-sodium atom collision cross section for excitation of first excited state of sodium

$\Omega^{*\uparrow}_{1\to 0}$	electron-sodium atom collision cross section for de-excitation of the first excited state of sodium
$q(\vec{r}, \tau)$	slowing down density
$\dot{q}_{conv}$	convective heat transfer rate
$\dot{q}_{electron}$	total heat transfer rate due to electron passage through the work function barrier
$\dot{q}_{J.H.}$	total rate of generation of thermal energy in center electrode due to Joule heating
$\dot{q}_{T.C.}$	total rate of heat loss from center electrode due to thermal conduction along the electrode
$\dot{q}_{rad}$	total rate of heat transfer from center electrode due to radiation
R_{ext}	external resistance
R_i	radius of inner electrode
R_o	radius of outer electrode
R_1	radius of inner electrode
Re_L	Reynolds number based on electrode length
R^o_ω	spectral intensity of blackbody radiation
$\overline{R^o_\omega}$	average blackbody spectral intensity of sodium D line width
r	radial distance
r_1	radius of inner electrode
r_2	radius of outer electrode
SLR	sodium line reversal
s	distance along particle path
T	temperature
T_a	temperature of argon atoms, temperature of neutral atoms
T_e	electron temperature
T_o	reference temperature
$\overline{T}_g$	mean effective gas temperature (axially averaged)

T_{SLR}	sodium line reversal temperature
$\bar{T}_w$	mean center electrode temperature (axially averaged)
T_w	surface temperature
T_1	temperature of inner electrode
T_2	temperature of outer electrode
T_∞	gas temperature upstream of test section
T^*	electronic excitation temperature
ΔT	temperature increment
t	time
T_{e-a}	electron-atom equilibration time
u	gas velocity, lethargy
V	voltage
V_c	cathode sheath potential
V_e	externally applied electrode voltage
V_g	potential drop across bulk of plasma
V_i	ionization potential
V_s	sheath potential
ΔV	voltage increment
ΔV_{2-1}	potential difference between inner and outer electrodes
v_e	mean electron velocity
v_g	gas velocity
w	test particle velocity
$\Delta w_{\|\|}$	change in test particle velocity in direction of original velocity
x	distance coordinate
z	axial distance

α	dimensionless parameter (non-equilibrium conduction theory)
β	dimensionless parameter (non-equilibrium conduction theory, specialized meanings given in text)
Γ	constant in equilibrium conductivity approximation
Δ	large increment
δ	dimensionless energy exchange parameter, small increment
ϵ	angle coordinate
ϵ_a	mean argon atom energy, mean neutral atom energy
ϵ_{a_o}	mean neutral atom energy at zero current density
ϵ_e	mean electron energy
ϵ_{e_o}	mean electron energy at zero current density
ϵ_i	mean ion energy, ionization potential
ϵ_o	permittivity of free space
ϵ_1	emissivity of inner electrode
ϵ_2	emissivity of outer electrode
$\dot{\epsilon}$	energy deposited per unit time per unit volume by electron thermalization
η	special meanings given in text
θ	dimensionless temperature ratio
K	thermal conductivity
λ	mean free path, wavelength
μ_a	net neutral flux of potassium atoms impinging on cathode (cm^{-2} sec^{-1})
ν	collision frequency, dimensionless voltage
ξ	average decrease of the logarithm of the electron energy per collision, special meanings given in text
π	3.14159...
ρ	gas density

$\sum$	dimensionless conductivity ratio, macroscopic cross section, summation symbol
σ	conductivity
$\sigma_{C.E.}$	conductivity computed from electron-neutral collisions
σ_{sp}	conductivity computed for fully-ionized gas
$\sigma\|_{exp}$	experimental value of the conductivity
σ_o	conductivity at reference temperature T_o
$\overline{\sigma}_T$	mean thermal conductivity of center electrode
τ	Fermi age, mean collision time, special meanings given in text
τ_{e-e}	mean electron-electron equilibration time
ϕ	viscous dissipation function
ϕ	electrical potential, work function
ϕ_{eff}	effective work function potential
ϕ_i	ionization potential
ϕ_s	sheath potential
$\Delta\phi$	potential difference
χ	dimensionless current density parameter
χ_{cm}	collision deflection angle in center of mass coordinates
ψ	special meanings given in text
Ω	dimensionless resistance ratio
ω	radian frequency
∇	gradient operator
$\nabla\cdot$	divergence operator
∇^2	Laplacian operator

APPENDIX B

Voltage-Current Characteristics Determined by Equilibrium Conductivity

This section describes an analysis performed by Professor E. E. Zukoski in conjunction with the interpretation of the experimental results described herein. As the details of this analytical work have not been published elsewhere, they are being presented here for completeness.

Three different channel geometries were considered in these calculations; coaxial and axial geometries similar to those utilized in the experiments, and a conventional rectangular geometry. The most difficult case is the coaxial one, and it will be treated first.

The basic equations which are needed are the following:

energy equation

$$\rho u c_p \frac{dT}{dx} = \frac{J^2}{\sigma} \quad , \tag{b-1}$$

current continuity

$$J_1 r_1 = jr \quad , \tag{b-2}$$

Ohm's law

$$V = \int_{r_1}^{r_2} \frac{J dr}{\sigma} \quad , \tag{b-3}$$

where the subscripts (1) and (2) refer to the inner and outer radii of the test section, respectively.

A group of non-dimensional parameters is then introduced:

$$\tau \equiv x/L \ , \quad \xi \equiv r/r_1 \ , \quad \theta \equiv T/T_o \ , \quad \sum \equiv \sigma/\sigma_o \ , \tag{b-4}$$

where the temperature $T = T_a = T_e$ as assumed by the equilibrium

conduction theory. In addition, the voltage and current density are normalized in the following manner.

$$j \equiv \frac{J_1}{\sqrt{\frac{\rho c_p u T_o \sigma_o}{L}}} , \tag{b-5}$$

$$\nu = \frac{V}{\sqrt{\frac{\rho c_p u T_o r_1^2}{L \sigma_o}}} . \tag{b-6}$$

Thus, the energy equation can be written in the form

$$\partial\theta/\partial\tau = j^2/\sum\xi^2 , \tag{b-7}$$

while Ohm's law becomes

$$\nu = \int_1^{\xi_2} \frac{j}{\sum\xi} \, d\xi . \tag{b-8}$$

Combining Eqs. b-7 and b-8 yields

$$\nu = \int_1^{\xi_2} \left(\frac{1}{\sum} \frac{\partial\theta}{\partial\tau} \right)^{\frac{1}{2}} d\xi . \tag{b-9}$$

The conductivity is then assumed to be given by the relation

$$\sum = e^{\Gamma(\theta - 1)} , \tag{b-10}$$

where Γ is a constant and $\theta \equiv T/T_o$. Inspection of conductivity values computed from the equilibrium theory indicates that Eq. b-10 is accurate to within 10 per cent over a temperature range slightly greater than 500°K.

Logarithmically differentiating Eq. b-10 and substituting from Eq. b-7 gives

$$\frac{1}{\sum} \frac{\partial \sum}{\partial\tau} = \Gamma \frac{\partial\theta}{\partial\tau} = \frac{\Gamma j^2}{\sum\xi^2} . \tag{b-11}$$

Integrating b-11 from 0 to τ and utilizing the boundary condition $\sum(\tau = 0) = 1$ results in the expression

$$\sum(\tau) = 1 + \frac{\Gamma}{\xi^2} \int_0^{\tau} \left(j(\tau)\right)^2 d\tau \ . \tag{b-12}$$

For convenience, the following definition is made:

$$\beta(\tau) \equiv \Gamma \int_0^{\tau} \left(j(\tau)\right)^2 d\tau \ . \tag{b-13}$$

Combining Eqs. b-11 and b-12 and substituting into b-9 produces a relation between ν and β.

$$\nu = \left(\frac{1}{\Gamma} \frac{d\beta}{d\tau}\right)^{\frac{1}{2}} \int_1^{\xi_2} \frac{\frac{1}{\xi} d\xi}{(1+\beta/\xi^2)} \tag{b-14}$$

Carrying out the integration in b-14 and realizing that ν, which is directly proportional to the externally applied voltage, may be considered a prescribed constant, results in the following differential equation for β:

$$\frac{d\beta}{d\tau} \left[\ell n \left(\frac{\xi_2^2+\beta}{1+\beta}\right)\right]^2 = 4\nu^2\Gamma \ . \tag{b-15}$$

Integrating b-15 from $\tau = 0$ to gives:

$$4\Gamma\nu^2\tau = \int_0^{\beta} \left[\ell n \left(\frac{\xi_2^2+\beta}{1+\beta}\right)\right]^2 d\beta \ , \tag{b-16}$$

where the limit on β is chosen so as to make τ equal unity once Γ and ν are given. The integral in b-16 can be evaluated in terms of an infinite series

$$4\Gamma\nu^2\tau = (\xi_2^2-1) \left[F\left\{\frac{\xi_2^2-1}{1+\beta}\right\} - F\left\{\xi_2^2-1\right\}\right] \ , \tag{b-17}$$

where the function $F\{x\}$ has the form

$$F\{x\} = \frac{1}{x}\left[(x+1)\ell n^2(x+1) - x\ell n^2 x + 2\left(1 - \frac{1}{4x} + \frac{1}{9x^2} + \frac{1}{16x^3} + \ldots\right)\right] \quad \text{(b-18)}$$

for $x > 1$, and

$$F\{x\} = \frac{1}{x}\left[(x+1)\ell n^2(x+1) + \frac{\pi^2 x}{3} - 2x^2\left(1 - \frac{x}{4} + \frac{x^2}{9} - \frac{x^3}{16} + \ldots\right)\right] \quad \text{(b-19)}$$

for $x < 1$.

The solution to Eq. b-17 is found by plotting the right hand side for various values of β. Then, by fixing Γ, setting $\tau = 1$, and picking a value of β, it is possible to solve for ν. With ν determined, Eq. b-17 is then used to find β as a function of τ for $0 < \tau < 1$.

From the original definition of β (Eq. b-13) and Eq. b-14 for ν, it follows that

$$\nu = \sqrt{\frac{j^2}{4}}\ \ell n\left[\frac{\xi_2^2 + \beta}{1 + \beta}\right] \quad , \quad \text{(b-20)}$$

and thus

$$j = \frac{2\nu}{\ell n\left[\frac{\xi_2^2 + \beta}{1 + \beta}\right]} \quad . \quad \text{(b-21)}$$

Since β is a function of τ according to b-17, it is seen that j is also a function of τ and may be determined in a closed form once ν is stipulated. After computing $j(\tau)$ from Eq. b-21, it is numerically integrated with respect to τ, and this yields a quantity directly proportional to the test section current. By reversing the normalizing procedure, $\int_0^1 j\, d\tau$ and ν give the desired current and voltage values, respectively.[0] The results of these computations are shown in Fig. 43, plotted as a function of the non-dimensional quantities v and i, where

$$v \equiv \frac{V}{\sqrt{\dot{m} c_p T_o R_o}} \quad \text{(b-22)}$$

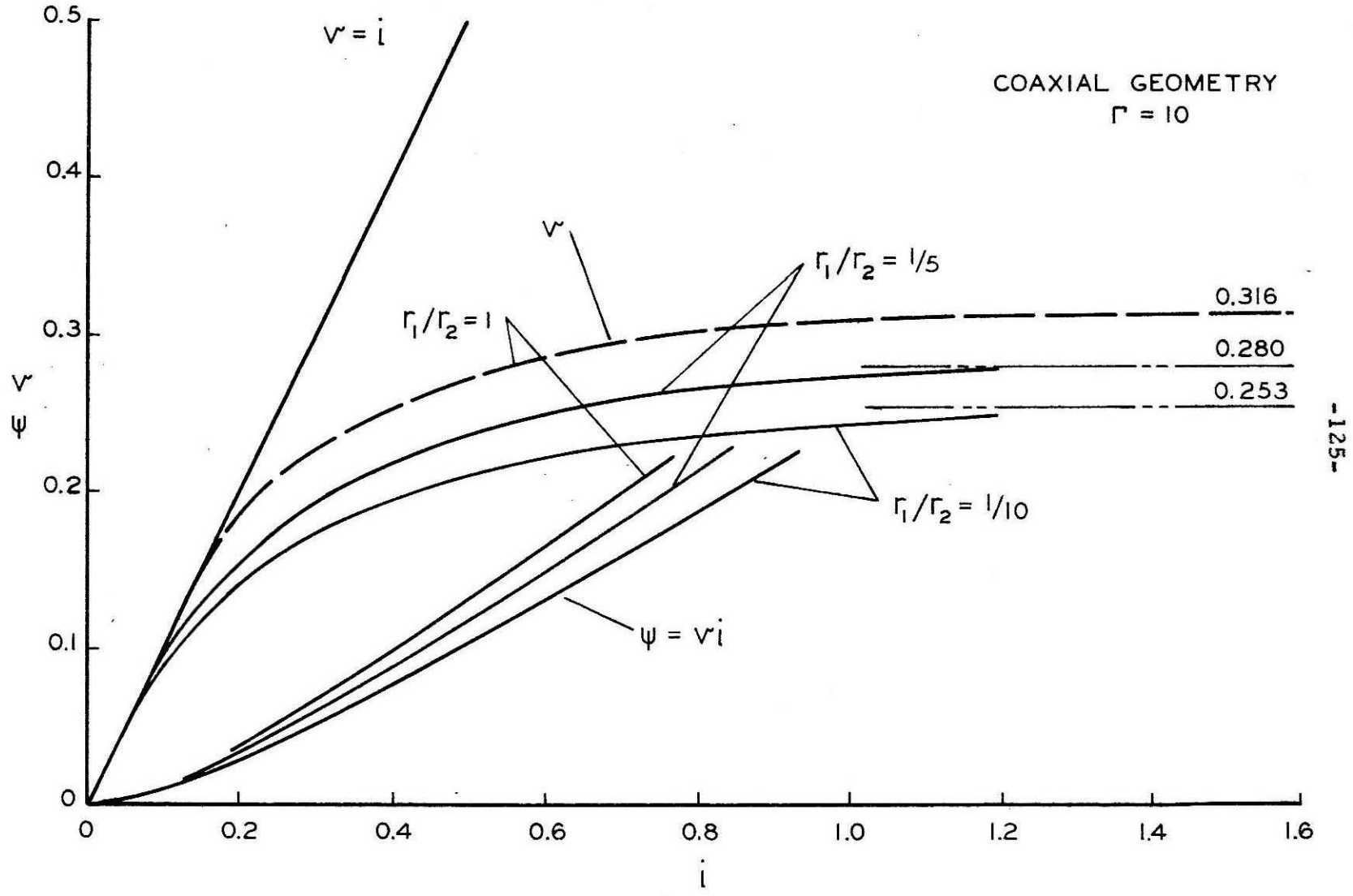

Figure 43. Non-Dimensional Voltage and Non-Dimensional Power Addition Versus Non-Dimensional Current (Coaxial Geometry).

and

$$i = \frac{I}{\sqrt{\frac{\dot{m}\, c_p\, T_o}{R_o}}} \quad . \tag{b-23}$$

In Eqs. b-22 and b-23, the quantity R_o is given by

$$R_o \equiv \frac{\ell n(r_2/r_1)}{2\pi L \sigma_o} \quad . \tag{b-24}$$

It can readily be shown that ν and $\int_0^1 j\, d\tau$ are related to v and i by the relations

$$v = \frac{\nu}{\left[(\xi_2^2 - 1)\ell n\, \xi_2^{\frac{1}{2}}\right]^{\frac{1}{2}}} \tag{b-25}$$

and

$$i = \left(\int_0^1 j(\tau)\, d\tau \right) \sqrt{\frac{\ell n\, \xi_2^2}{\xi_2^2 - 1}} \quad . \tag{b-26}$$

The solution of the axial case is straightforward. Non-dimensional quantities are introduced as before, except that $R_o \equiv (L/\sigma_o A)$ in this case. Integration of the equations in closed form is possible here with the following results:

$$v = \frac{\ell n(1 + \Gamma_i^2)}{\Gamma_i} \tag{b-27}$$

and

$$\psi \equiv vi = \theta(\tau=1) - 1 = \frac{\ell n(1 + \Gamma_i^2)}{\Gamma} \quad . \tag{b-28}$$

The parameter ψ is a measure of the total electrical power added to the gas as it passes through the test section. Equation b-27 predicts a maximum value of $v_m = 0.8/\sqrt{\Gamma}$ at $i = 2/\sqrt{\Gamma}$ with a corresponding value of $\psi = 1.6/\Gamma$. Figure 44 shows a plot of Eqs. b-27 and b-28 for $\Gamma = 10$. It is seen that $v_m \cong 0.25$ and the related value of ψ is 0.16.

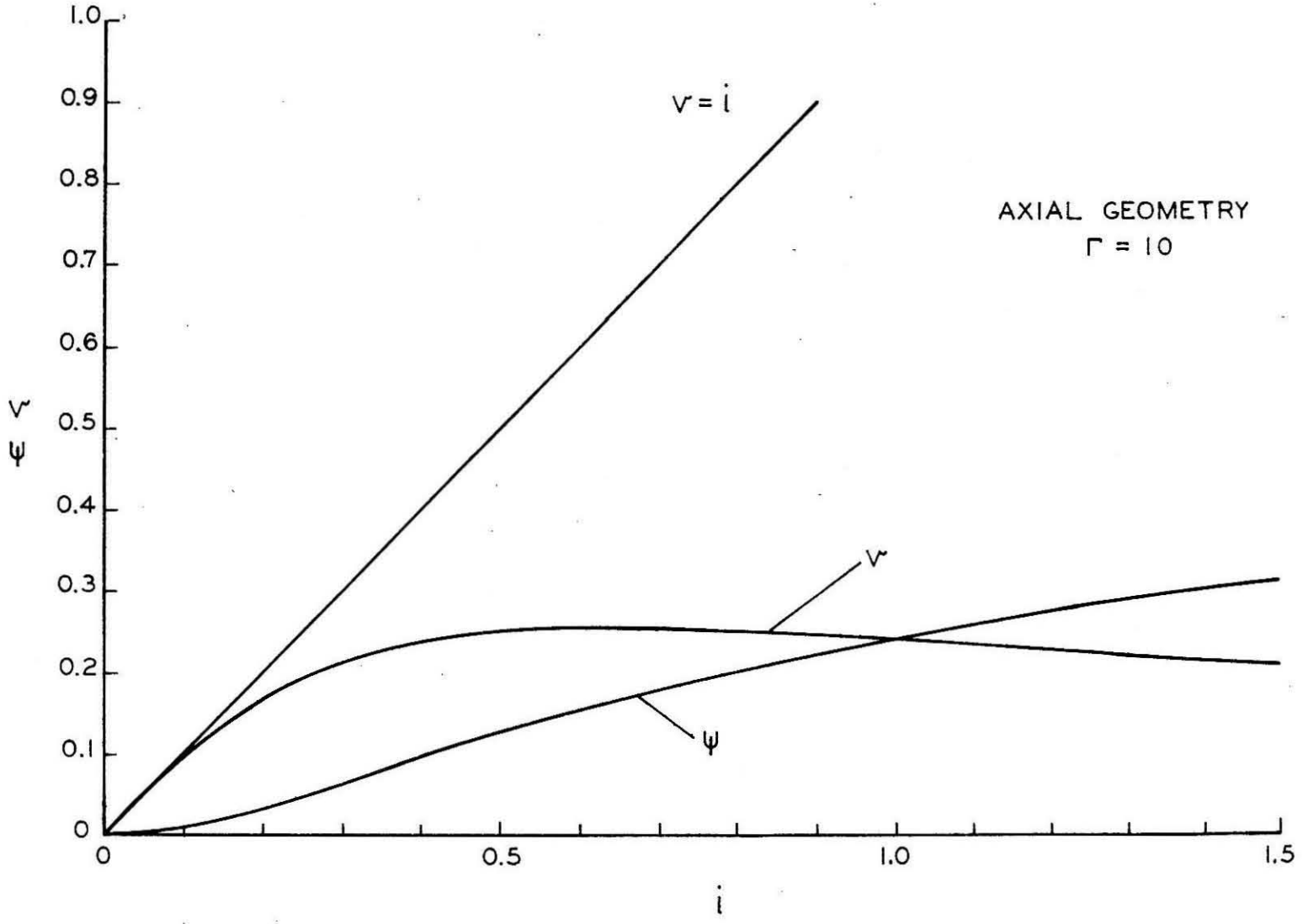

Figure 44. Non-Dimensional Voltage and Non-Dimensional Power Addition Versus Non-Dimensional Current (Axial Geometry).

This indicates that the voltage - current characteristic is highly non-linear, even with relatively small amounts of power addition.

Although no experiments were carried out with a rectangular geometry, this case was also treated in the above analysis. As with the axial case, the required integrations were easily carried through to give the results

$$i = \frac{1}{\Gamma v} \ell n \left(\frac{1}{1 - \Gamma v^2} \right) , \tag{b-29}$$

$$\theta(\tau) = 1 + \frac{1}{\Gamma} \ell n \left(\frac{1}{1 - \Gamma \tau v^2} \right) , \tag{b-30}$$

$$j(\tau) = \frac{v}{1 - \Gamma \tau v^2} , \tag{b-31}$$

$$\psi = \theta(\tau=1) - 1 = \frac{1}{\Gamma} \ell n \left(\frac{1}{1 - \Gamma v^2} \right) . \tag{b-32}$$

The notation is the same as that used in the previous cases, except that $R_o \equiv h/\sigma_o A_e$, where h is the distance between electrodes and A_e is the electrode area.

Inspection of Eq. b-29 indicates that a maximum value of the voltage is reached, even though i becomes indefinitely large. Figure 45 shows the behavior of the voltage-current characteristic for the case $\Gamma = 10$. There it is seen that v is within 90 per cent of its maximum value when $\psi = 0.16$. Once again, a strong non-linearity is evidenced at relatively small power additions.

In the preceding analysis the effect of cool gas boundary layers on the electrode surfaces has been entirely neglected. Because of the strong variation of the conductivity with temperature predicted by the equilibrium model of current conduction, the boundary layers might be expected to produce a marked influence on the voltage-current

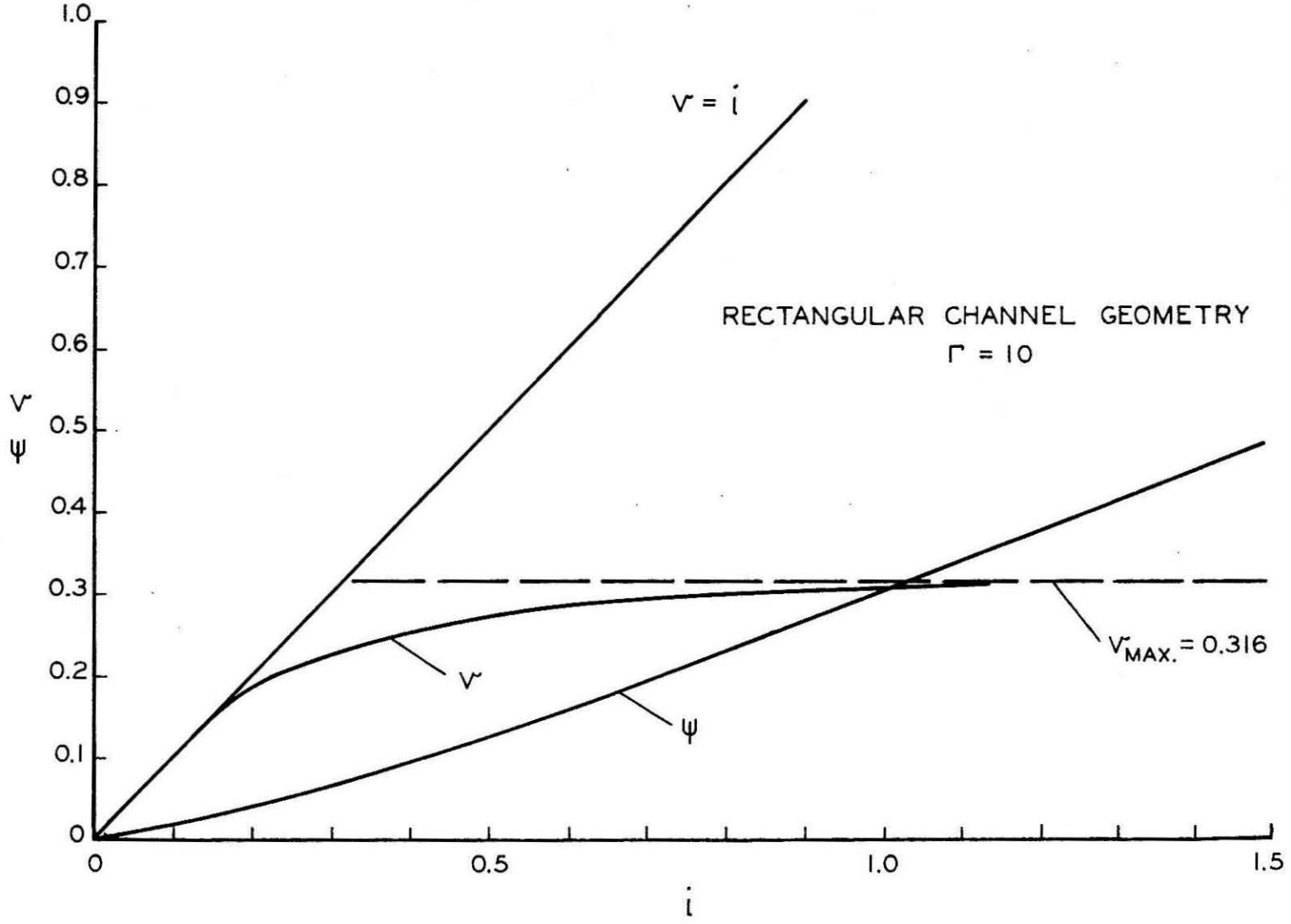

Figure 45. Non-dimensional Voltage and Non-dimensional Power Addition Versus Non-dimensional Current (Rectangular Geometry).

characteristics predicted by this model.

As in most boundary layer analyses, a solution could be obtained only by making some rather drastic simplifications. At the entrance to the electrode section (coaxial geometry) the conductivity was given an initial stepwise variation in the radial direction, while the initial radial temperature distribution was taken to be a constant value. The assumption of such inlet conditions is permissible in view of the small change in the conductivity. Thus, Eq. b-12 was modified to read

$$\sum(\tau, \xi) = \sum_o(\xi) + \frac{\Gamma}{\xi^2} \int_0^\tau (j(\tau))^2 \, d\tau \quad . \qquad \text{(b-33)}$$

The method of solution then proceeded in a manner completely analogous to that shown above. Substitution of the appropriate numerical quantities from a typical run produced a V-I curve which differed very little from the curve computed without the boundary layer effect. The two aforementioned curves were normalized to give the same total gas resistance at zero current. A more marked curvature at low currents and a decrease in the asymptotic voltage of about 15 per cent were the chief differences between the boundary layer example and the original curve.

Qualitatively, it may be seen that since the local Joule heating is inversely proportional to the local conductivity, the current tends to make the conductivity distribution more uniform. Thus, the effect of the cold boundary layer is rapidly reduced as the current is increased.

As previously mentioned, in the section discussing heat transfer, the quantity $\bar{T}_g$ was computed by means of the methods described in this Appendix. This was done simply by computing the variation of the

current density with axial position from Eq. b-21. Substitution of $j(\tau)$ into b-12 provides the variation of conductivity with z, and this information along with Eq. b-10 gives the desired free stream temperature variation with distance down the test section. A simple, linear, average value of this temperature variation then yields the desired value of $\bar{T}_g$.

APPENDIX C

Interpretation of the Sodium Line Reversal Temperature Measurements

If a plasma is in thermodynamic equilibrium, the principle of equipartition of energy applies. The relative degree of population of the various electronic levels of the atoms is then given by

$$n^*/n_o = g^*/g_o \, e^{-E^*/kT^*} \qquad (c\text{-}1)$$

where $T^* = T_a$. In equilibrium, T_a is the mean translational energy of the atoms, ions, and electrons, which are all equal.

If a sodium line reversal (SLR) temperature measurement is taken under the above conditions, the result will be $T_{SLR} = T^* = T_a$. Under non-equilibrium conditions, the SLR measurement will still yield the effective excitation or population temperature T^* associated with the sodium D lines (λ = 5890, 5896 Å, E^* = 2.1 eV). However, there may be a large difference between T_a and T^*.

The problem to be considered here is one of quasi-equilibrium. A spatially uniform, steady-state condition prevails in which the electron component of the plasma has a Maxwell-Boltzmann velocity distribution characterized by a temperature T_e. The ions and atoms have similar distributions characterized by temperature T_a. This is the situation that prevails locally, in the aforementioned current conduction experiments, according to the non-equilibrium theory.

Under strict equilibrium conditions, the principle of microscopic reversibility applies[19]. Briefly, this principle states that the rate of population of a given quantum state by a particular process must be exactly balanced by the rate of depopulation of the state by the

reverse of that particular process. When this principle applies, the rate of decay of the number of excited states by photon emission is just equal to the rate of production of the same excited state by photon absorption. Similarly, the rate of production of the excited state by inelastic electron-atom collisions is equal to the rate of de-excitation by super-elastic electron collisions. In order to equate these last two rates for the conditions of the aforementioned experiments, it becomes necessary to evaluate the competing mechanisms both for excitation and decay.

Since the mean lifetime of the first excited state of sodium is only 1.6×10^{-8} sec, it is readily seen that photon emission may be the dominant decay mechanism. This would be the case for a very thin layer of gas. However, the radiation resulting from the photon de-excitation has just the right frequency to be absorbed readily by a neighboring sodium atom. If there are a sufficient number of unexcited sodium atoms present, this "resonance radiation" from the D lines will be effectively confined. Thus, in the central regions of the plasma, there will be effectively no net rate of decay of this excited state by photon emission.

An estimate of the trapping of the resonance radiation may be obtained from computed values of the integrated absorption coefficient. Following Penner[20], it can be shown that

$$\frac{d}{d(px)} \int_{\Delta\omega} R^{o}_{\omega} \, d\omega = \int_{\Delta\omega} R^{o}_{\omega} P_{\omega} \, d\omega \quad , \qquad (c-2)$$

where $\Delta\omega$ implies integration over the absorption line width. Since only an estimate of the radiation attenuation is desired, it is permissible

to write

$$\frac{d}{d(px)}\left(\overline{R^{o}_{\omega}}\right)\Delta\omega = \overline{R^{o}_{\omega}} \int_{\Delta\omega} P_{\omega}\, d\omega \qquad (c\text{-}3)$$

where $\overline{R^{o}_{\omega}}$ is the value of the spectral intensity at the line center and $\int_{\Delta\omega} P_{\omega} d\omega$ is the integrated absorption coefficient.

From Eq. c-3 it follows that

$$\overline{R^{o}_{\omega}} = \text{Const}\; e^{-\left\{\int_{\Delta\omega} P_{\omega} d\omega\right\}(px)} \qquad (c\text{-}4)$$

and the characteristic attenuation length is

$$L^{*} = \frac{\Delta\omega}{p\int_{\Delta\omega} P_{\omega} d\omega} \quad . \qquad (c\text{-}5)$$

Penner has derived an expression for $\int_{\Delta\omega} P_{\omega} d\omega$ in terms of fundamental constants and an experimentally determined parameter known as the oscillator strength (f) .

$$\int_{\Delta\omega} P_{\omega} d\omega = \frac{\pi e^{2}}{p m_{e} C^{2}} n_{Na}\, f_{0\to 1} \qquad (c\text{-}6)$$

Thus

$$L^{*} = \frac{\Delta\omega}{\frac{\pi e^{2}}{m_{e} C^{2}} n_{Na}\, f_{0\to 1}} \quad , \qquad (c\text{-}7)$$

where n_{Na} is essentially the total number of sodium atoms per unit volume (approximately 2×10^{15} cm^{3}) ; the degree of excitation being very small for the conditions of the experiments reported here. The effective line width is taken to be 0. 1 angstroms as a conservative estimate. This value is quoted by Bundy and Strong as being applicable to "most flames at atmospheric pressure."[21] Actually, the line width

will be somewhat wider than this, owing to the effects of pressure and Stark broadening. The electric fields produced by the ions and electrons account for the presence of the Stark effect.

Taking the oscillator strength to be 0.33, Eq. c-7 gives $L^* \cong 0.5 \times 10^{-3}$ cm. This indicates that radiative equilibrium exists in the inner portion of the plasma.

It now becomes necessary to compare the competing mechanisms for excitation and de-excitation. For excitation, there exists the following possibilities:

$$\begin{aligned} Na + e &\rightarrow Na^* + e \\ Na + A &\rightarrow Na^* + A \\ Na + K &\rightarrow Na^* + K \\ Na + Na &\rightarrow Na^* + Na \end{aligned} \qquad \text{(c-8)}$$

Because of the relatively small quantities of Na^+, K^+, and A^+, the production due to inelastic collisions with these species will be negligible. A similar situation holds for the de-excitation process, which is the inverse of the processes considered in Eq. c-8.

Unfortunately, the data on the cross sections for the forward and reverse reactions indicated in c-8 are not very extensive. Massey and Burhop[13] present a plot of excitation cross section for electron-sodium inelastic collisions which gives a Q value on the order of 5×10^{-16} cm^2. From data concerning the quenching of resonance radiation by argon atoms, it is seen that the ($Na + A \rightarrow Na^+ + A$) reaction in either direction will have a cross section much less than 10^{-16} cm^2.[13] Based on statistical balancing, a definite relationship is found to exist between the cross sections for the forward and reverse

reactions. This will be demonstrated shortly.

No data seem to be available for the sodium-sodium collisions. However, the helium-helium excitation collision has a $Q \approx 5 \times 10^{-20}$ cm^2 at the energies present in these experiments. On this basis, the sodium-sodium reactions will be neglected.

Such analogous reasoning is, of course, very doubtful, especially in comparing helium collision data with similar alkali metal data. In the absence of the required information, some analogous reasoning procedure is the only course of action available. Again, no data is present for sodium-potassium excitation collisions. But with hydrogen atoms exciting helium atoms, no appreciable effect was noticed until an energy level of approximately 10 keV was reached. Thus, the sodium-potassium mechanism will also be neglected.

From the above considerations, the electron-sodium collisions emerge as the dominant processes for exciting and de-exciting the sodium in those regions of the plasma where the resonance radiation is essentially trapped. Thus, in what follows, the super-elastic collision de-excitation rate will be equated to the inelastic collision excitation rate.

From Ref. 5, the number of collisions between two classes of particles occurring per unit time and per unit volume of configuration space, is given by

$$\dot{n}_{a-b} = \int_{\vec{v}_a} \int_{\vec{v}_b} \iint_{p\,\epsilon} f_a(\vec{r}, \vec{v}, t)\, f_b(\vec{r}, \vec{v}, t)\, V p dp d\epsilon d^3v_b d^3v_a \,. \qquad \text{(c-9)}$$

The integration over p and ϵ may be carried out to give

$$\iint_{p\varepsilon} pdpd\varepsilon = \iint_{\chi\varepsilon} \sigma(\chi)\sin\chi d\chi d\varepsilon = \Omega_{ab} \quad . \tag{c-10}$$

For the problem at hand, only electrons (particles denoted by "a") having energies greater than E_1 (2.1 eV) can produce an excitation collision. The velocity of these electrons is very much higher than the mean velocity of the sodium atoms as the latter's mean energy is roughly 0.2 eV, and the mass ratio m_e/m_{Na} is on the order of 1/40,000. As a result, the sodium atoms may be considered essentially stationary with a distribution function ("b" corresponds to the sodium atom)

$$f_b(\vec{r}, \vec{v}_b, t) = n_{Na}(\vec{r}, t)\, \delta(\vec{v}_b) , \tag{c-11}$$

where $\delta(\vec{v}_b)$ is the Dirac delta function.

With $\vec{v}_b \equiv 0$ the expression for $V \equiv |\vec{v}_a - \vec{v}_b|$ reduces to $V = |\vec{v}_a| = \sqrt{2\varepsilon_a/m_a}$. Since V is now independent of the $\vec{v}_b$ integration, there results

$$\int_{\vec{v}_b} f_b \, d^3v_b = \int_{\vec{v}_b} n_b \, \delta(\vec{v}_b) d^3v_b = n_b(\vec{r}, t) \quad . \tag{c-12}$$

Finally, the integration over the applicable portion of the $\vec{v}_a$ velocity space $v_e^2 > 2E_1/m_e$ can be transformed into an energy integral if the $f(r, \vec{v}_e, t)$ distribution is isotropic in velocity space:

$$\iiint_{v_a^2 \geq \frac{2E_1}{m_a}} \Omega_{a-b} f_a(\vec{r}, \vec{v}_a, t) |\vec{v}_a| d^3v_a = \int_{\varepsilon_e = E_1}^{\infty} \Omega_{a-b} n_a f(\varepsilon_e) \sqrt{\frac{2\varepsilon_e}{m}} \, d\varepsilon_e \quad . \tag{c-13}$$

Combining c-10, c-12, and c-13 yields

$$\dot{n}_{a-b} = n_a n_b \int_{\varepsilon_a=E_1}^{\infty} Q_{a-b}\, f_a(\varepsilon_a) \sqrt{\frac{2\varepsilon_a}{m_a}}\, d\varepsilon_a \quad . \tag{c-14}$$

By inserting the appropriate cross sections in Eq. c-15, the rates of excitation and de-excitation are found to be respectively:

$$\dot{n}_{0\to 1} = n_{Na(o)} n_e \int_{\varepsilon_e=E_1}^{\infty} Q^*_{0\to 1}\, f(\varepsilon_e) \sqrt{\frac{2\varepsilon_e}{m_e}}\, d\varepsilon_e \tag{c-15}$$

and

$$\dot{n}_{1\to 0} = n_{Na(*)} n_e \int_{\varepsilon_e=0}^{\infty} Q^*_{1\to 0}\, f(\varepsilon_e) \sqrt{\frac{2\varepsilon_e}{m_e}}\, d\varepsilon_e \quad . \tag{c-16}$$

Equating Eqs. c-15 and c-16 and recalling c-1 yields

$$\frac{n_{Na(*)}}{n_{Na(o)}} = \frac{\int_{\varepsilon_e=E_1}^{\infty} Q^*_{0\to 1}\, f(\varepsilon_e) \sqrt{\frac{2\varepsilon_e}{m_e}}\, d\varepsilon_e}{\int_0^{\infty} Q^*_{1\to 0}\, f(\varepsilon_e) \sqrt{\frac{2\varepsilon_e}{m_e}}\, d\varepsilon_e} = \frac{g^*}{g_o}\, e^{-E_1^*/kT^*} \quad . \tag{c-17}$$

As previously discussed, the electron distribution function may be considered to be Maxwellian

$$f(\varepsilon_e) = 2\left(\frac{\varepsilon_e}{\pi k^3 T_e^3}\right)^{\frac{1}{2}} e^{-\varepsilon_e/kT_e} \quad , \tag{c-18}$$

and then the integral in c-15 can be rearranged so as to put c-17 in the form

$$\frac{n_{Na(*)}}{n_{Na(o)}} = e^{-E_1^*/kT_e} \frac{\int_0^{\infty} Q^*_{0\to 1}(\varepsilon_e)\, e^{-\frac{(\varepsilon_e - E_1^*)}{kT_e}} (kT_e)\, d\left(\frac{\varepsilon_e - E_1}{kT_e}\right)}{\int_0^{\infty} Q^*_{1\to 0}(\varepsilon_e)\, e^{-(\varepsilon_e/kT_e)}\, d\varepsilon_e} \quad . \tag{c-19}$$

Under conditions of thermodynamic equilibrium, $T_e = T_a = T^*$, and it is seen from Eq. c-1 that the ratio of the integrals in c-16 is simply g^*/g_o for any value of T_a. This indicates a specific relationship between the excitation and de-excitation cross sections. Since the atoms are considered essentially stationary in the above analysis, it is apparent that the ratio of the integrals will be g^*/g_o for any value of T_e in direct analogy with the thermodynamic situation mentioned above in which T_a is arbitrary.

Thus, it may be concluded that to the degree of validity of the previous assumptions

$$e^{-(E_1^*/kT^*)} = e^{-(E_1^*/kT_e)}, \qquad \text{(c-20)}$$

and thus $T_e = T^*$. This means that the SLR temperature measurements performed in the experimental tests should be equal to the electron temperature. This would be the case for a plasma having a spatially uniform electron temperature.

This result is not surprising in view of the arguments made earlier that lead to the result that electron-atom encounters dominated the processes of excitation and de-excitation. Equation c-19 expresses this fact in a mathematical form and also demonstrates the fact that the electron collision excitation process is related in a very definite, physical way to the reverse process of de-excitation.

In the actual interpretation of SLR temperatures, some additional factors must be considered. As shown by Bundy and Strong[21], the SLR measurement only gives an average temperature value when the measurement is being made through a media in which there are spatial temperature variations. This averaging process is, unfortunately, not

in a linear fashion. The portions of the gas nearer the spectroscope are weighted more heavily. Thus the SLR temperatures experimentally obtained are modified by the existence of cool boundary layers which surround the hotter regions of the plasma. However, in view of the comparatively small thickness of the boundary layers, these aforementioned effects were neglected in the interpretation of the SLR data.

Another factor which must be considered in ascertaining proper meaning of SLR measurements is the effect of foreign gases in the plasma. As evidenced in Fig. 22, the effect of adding nitrogen was an increase in the effective excitation temperature associated with the sodium D lines.

Similar phenomena have been noted by other investigators, and such processes are often referred to as "sensitized fluorescence".[22]

The proposed mechanism for the experiments described here consists of the following sequence. Electron-nitrogen inelastic collisions produce excited nitrogen atoms. Before these nitrogen atoms de-excite by photon emission, they collide with a sodium atom in the ground state and transfer the electronic excitation to the sodium atom. The excess energy difference between the two excited states then appears as kinetic energy of the recoiling atoms. As a result of the transfer of excitation to the sodium, the population of the electronic level which is related to the sodium D lines is enhanced above the value determined in the absence of nitrogen. This increase in population appears as a higher SLR temperature measurement.

A study of the quantum-mechanical resonance effects associated with the sensitized fluorescence indicates that the possibility of such

events occurring is greatly enhanced if the energy level of the initially excited atom is slightly above but as close as possible to the energy level of the atom receiving the excitation. In the case of nitrogen and sodium, the two pertinent energy levels lie at 2.3 and 2.1 eV, respectively. However, in the case of helium, the first excited state is at 19.6 eV. Thus, a strong effect is expected in the case of nitrogen, and a much weaker effect with helium. Inspection of Figs. 22 and 23 confirms this anticipated result.

The enchancement of the population of the sodium resonance state increases with increasing nitrogen concentration. However, the addition of the nitrogen cools the gas, and eventually the decreasing temperature becomes the predominant effect and the effective excitation temperature of the sodium reaches a maximum and then begins to decrease. This is in accordance with the experimental results shown in Fig. 22.

APPENDIX D

Electron Thermalization Processes

In a discussion of the transition phenomena and the current limited mode of current conduction, reference was made to the process of thermalizing the electrons which had been accelerated by the cathode sheath potential. During the later stages of the transition process, and while operating in the current limited mode, the cathode sheath potential was much larger than kT_w. Thus, the electrons may be treated as though they all possessed the same velocity at the outer edge of the sheath. When the electrons enter the plasma they collide with both charged and neutral particles. A complete and correct solution to the problem would consist of solving the simultaneous Boltzmann equations for all the species present in the plasma. As in ordinary gas dynamic problems, the chief difficulty arises in treating the collision terms. In order to gain some insight into the thermalization phenomena without attempting a general solution of the complete equations, two hypothetical cases will be considered.

In the first case, the electrons will be assumed to collide only with neutral atoms. Electron-electron and electron-ion interactions will be presumed non-existent. In the second case, the electrons will be considered to interact only with other charged particles. Admittedly, the results of these two cases cannot be simply superimposed with the hope of obtaining a description of the actual situation.

Electron-Neutral Collisions

The case of electron-neutral interactions can be treated by the Fermi Age method, which has proved so useful in the study of neutron

thermalization[12]. As shown in Ref. 12, the Fermi Age model is a first approximation to the Boltzmann equation if the slowing down of the energetic particles may be considered as a continuous process. This means that the energy loss per collision must be small compared to the initial energy of the incident particle. With electron-atom elastic collisions, this is indeed the case because of the relative masses of the two particles (see Eq. 13 in the text).

The neutron thermalization problem is given in terms of the following equation:

$$\nabla^2 q(\vec{r}, \tau) = \frac{\partial}{\partial \tau} q(\vec{r}, \tau) , \qquad \text{(d-1)}$$

where $q(\vec{r}, \tau)$ is the "slowing down density" and equals the number of electrons slowing down past a given value of lethargy (energy) per unit time per unit volume in the region around $\vec{r}$. The quantity τ is referred to as the "Fermi Age",

$$\tau = \int_0^u \frac{D(u)}{\xi \sum_t (u)} du , \qquad \text{(d-2)}$$

and the lethargy u is defined by

$$u = \ell n \frac{\epsilon_i}{\epsilon} , \qquad \text{(d-3)}$$

ϵ_i being the initial energy of the electrons at the sheath edge.

The appropriate solution of Eq. d-1 for an infinite line source of high velocity electrons is given by

$$q(r, u) = \frac{q_o \, e^{-r^2/4\tau}}{4\pi \tau (u)} , \qquad \text{(d-4)}$$

where q_o is the electron flux per unit length of source line. In order to utilize Eq. d-4, it is necessary to neglect the finite radius of the

center electrode. A solution to Eq. d-1 could be found for $r_i \neq 0$ and would be found by performing the Laplace inversion shown below.

$$q(r,u) = \frac{1}{2\pi j} \int_{c-j\infty}^{c+j\infty} \frac{q_o}{2\pi s} \frac{K_o(r\sqrt{s})e^{\tau s}ds}{\int_{r_i}^{\infty} K_o(r\sqrt{s})rdr} .$$

Here, K_o is the modified Bessel function of the second kind of zero order. The effort required to carry out the procedures indicated in this last equation is not warranted in view of the drastic assumptions previously made. Hence, the simpler situation given by Eq. d-4 will suffice.

The number of collisions suffered by an electron in slowing down through the lethargy interval du is simply du/ξ. It follows that the rate of energy loss per unit volume per unit time resulting from electrons slowing down through the interval du is then

$$d\dot{\epsilon} = q(\vec{r},u) \frac{du}{\xi} (\overline{\delta\epsilon}) , \qquad (d-5)$$

where the mean energy loss per collision is given by

$$(\overline{\delta\epsilon}) = \frac{(1-\alpha)\epsilon}{2} = \frac{(1-\alpha)}{2} \epsilon_s e^{-u} \qquad (d-6)$$

and

$$\alpha \equiv \left(\frac{1 - m_a/m_e}{1 + m_a/m_e}\right)^2 .$$

Combining Eqs. d-5 and d-6 and integrating over the entire range of lethargy values yields the rate of energy deposited per unit volume due to electron thermalization:

$$\dot{\epsilon} = \int_{u=0}^{u_{max}} q(r,u) \frac{(1-\alpha)}{\xi} (e\phi_s)e^{-u} du . \qquad (d-7)$$

Substituting for $q(r,u)$ from d-4 and assuming $\beta \equiv D/\xi\sum$ is constant and that $u_{max} \to \infty$ yields

$$\dot{\epsilon} = \frac{q_o(1-\alpha)e\phi_s}{4\pi\xi\beta} \int_0^\infty \frac{e^{-(r^2/4\beta u)}e^{-u}du}{u} . \qquad \text{(d-8)}$$

The integral may be approximated by the method of steepest descent[23] for $r^2/4\beta \ll 1$, giving the result

$$\dot{\epsilon} = \sqrt{2\pi}\,\frac{J_L\phi_s}{4\pi\beta}\, e^{-\left(1+\frac{r^2}{4\beta}\right)} , \qquad \text{(d-9)}$$

where $J_L \equiv q_o/e$ and the approximation $\xi \cong (1-\alpha)/2$ has been used. If Eq. d-9 is integrated over the entire volume, the result should equal the rate at which the line source is delivering energy to the system, i.e., $J_L\phi_s$. But integration of $\dot{\epsilon}$ gives

$$\int_0^\infty 2\pi r\dot{\epsilon}\,dr = \frac{\sqrt{2\pi}}{e} J_L\phi_s \simeq 0.923\, J_L\phi_s . \qquad \text{(d-10)}$$

The discrepancy is due to the approximation made in the steepest descent integration. If the proper "normalizing factor" is put in the expression for $\dot{\epsilon}$, Eq. d-9 then reads

$$\dot{\epsilon} = \frac{J_L\phi_s}{4\pi\beta} e^{-r^2/4\beta} , \qquad \text{(d-11)}$$

which has previously been given as Eq. 55 in the discussion of results.

Electron-Electron and Electron-Ion Collisions

The potential associated with charged particle interaction is the Coulomb potential. Because of the long range of these electrostatic forces, the effect of multiple "distant encounters" outweighs the much rarer event in which the electrons' velocity vector is greatly changed.

Spitzer[6] considers the case of a large number of test particles

(electrons in this case) suffering encounters with field particles. The average rate at which test particles are slowed down by interactions with the field particles is computed under the assumption of a Maxwellian velocity distribution of the field particles, and is referred to as a diffusion coefficient or "coefficient of dynamical friction."

$$<\Delta w_{11}> = - A_D\left(\frac{m_1}{2kT_1}\right)\left(1 + \frac{m_e}{m_1}\right) G\left\{\left(\frac{m_1 w^2}{2kT_1}\right)^{\frac{1}{2}}\right\} \qquad \text{(d-12)}$$

where

$$A_D = 8\pi e^4 \ell n \Lambda / m_e^2 \qquad \text{(d-13)}$$

and

$$G(x) = \frac{\frac{2}{\sqrt{\pi}} \int_0^x e^{-g^2} dg - x \frac{d}{dx} \int_0^x e^{-g^2} dg}{2x^2} \qquad \text{(d-14)}$$

with

$$x = (m_1 w^2 / 2kT_1)^{\frac{1}{2}} \quad . \qquad \text{(d-15)}$$

The subscript (1) refers to the field particles (electrons and ions). In the case of x being large, i.e., $m_1 w^2/2 \gg kT_1$, or equivalently, $e\phi_s \gg kT_1$, then $x^2 G(x) = 1/2w^2$, and hence

$$<\Delta w_{11}> = A_D \frac{1}{2w^2}\left(1 + \frac{m_e}{m_1}\right) . \qquad \text{(d-16)}$$

For a typical test particle, one can write

$$\frac{d(w_{11})}{dt} = w_{11} \frac{dw_{11}}{ds} = - \frac{A_D}{2w_{11}^2}\left(1 + \frac{m_e}{m_1}\right) \qquad \text{(d-17)}$$

where s is in the initial direction of w.

Integrating Eq. d-17,

$$\frac{w_{11}^4}{2} = - A_D\left(1 + \frac{m_e}{m_1}\right) + \frac{w_o^4}{2} \quad ,$$

where w_o is the initial electron velocity at $s = 0$. To find an effective slowing down distance for the electrons, w_{11} is arbitrarily set equal to $0.1\, w_o$, and there results

$$s^* \cong \frac{w_o^4}{2A_D\left(1 + \frac{m_e}{m_1}\right)} \quad . \tag{d-18}$$

A_D is independent of whether m_1 is taken as m_e or m_a. Thus, s^* is different by approximately a factor of two if the field particles are considered all ions or all electrons. The larger value of s^* was computed based on $T_1 = 2000^\circ K$ and $n_k/n_a = .004$. With $\phi_s = 10$ volts and 0.1 eV, the respective values of s^* are 0.6 cm and 3×10^{-4} cm. This last value was based on the limiting value of $<\Delta w_{11}>$ for low velocities, and it was also assumed that $e\phi_s = kT_1$.

APPENDIX E

Description of the Apparatus

Flow System

Photographs of the experimental equipment are shown in Figs. 46 and 47. In Fig. 48, a schematic diagram including all essential components is presented.

Electrical power to the arc jet was supplied from a conventional motor-generator unit remotely located. This m-g set supplied approximately 135 volts DC at power levels varying from 3 to 7 kilowatts. Large, uncooled ballast resistors were utilized in controlling the arc current. The arc jet was operated with both the copper anode and cathode water cooled and was vortex-stabilized by tangential injection of the argon through sonic orifices. It was experimentally determined that the arc ran more efficiently and stably with the arc electrons flowing in a direction opposite to the argon flow.

A small flow rate of argon was bubbled through a bath of liquid potassium, and thus a known amount of potassium vapor was entrained depending upon the bath temperature. This secondary argon-potassium flow was then mixed with the main, heated argon stream. The entire flow then passed through a stainless steel mixing chamber (.37" I. D. × 6" long) in which equilibration processes produced a more or less uniform, homogeneous fluid. Finally, the resulting "seeded plasma" passed through an appropriate test section. Sketches of the test sections have previously been shown in Figs. 2, 3, and 4.

After the plasma emerged from the test section, it was drawn into an exhaust tube of 2" I. D. This exhaust system was connected to

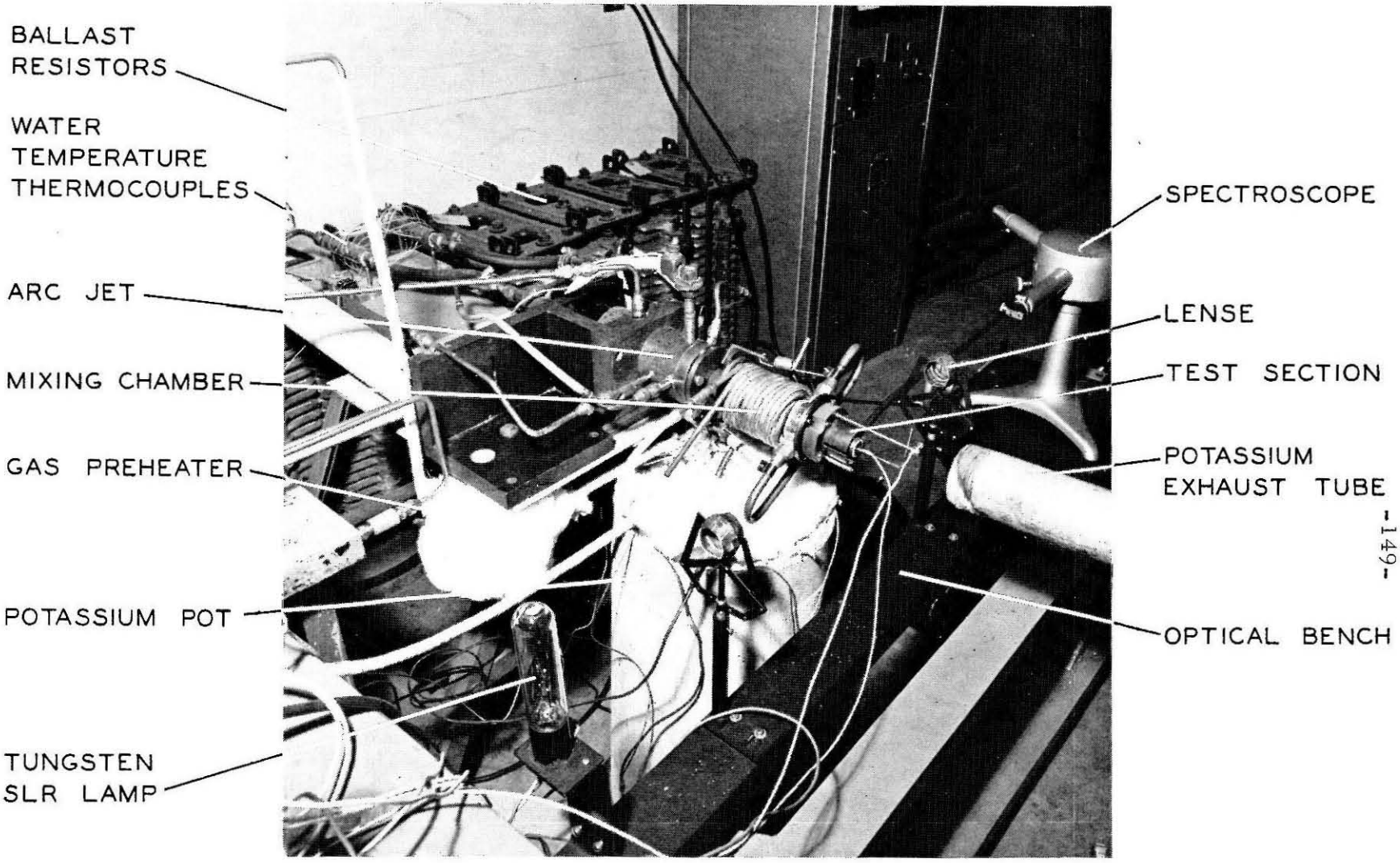

Figure 46. View of Experimental Apparatus.

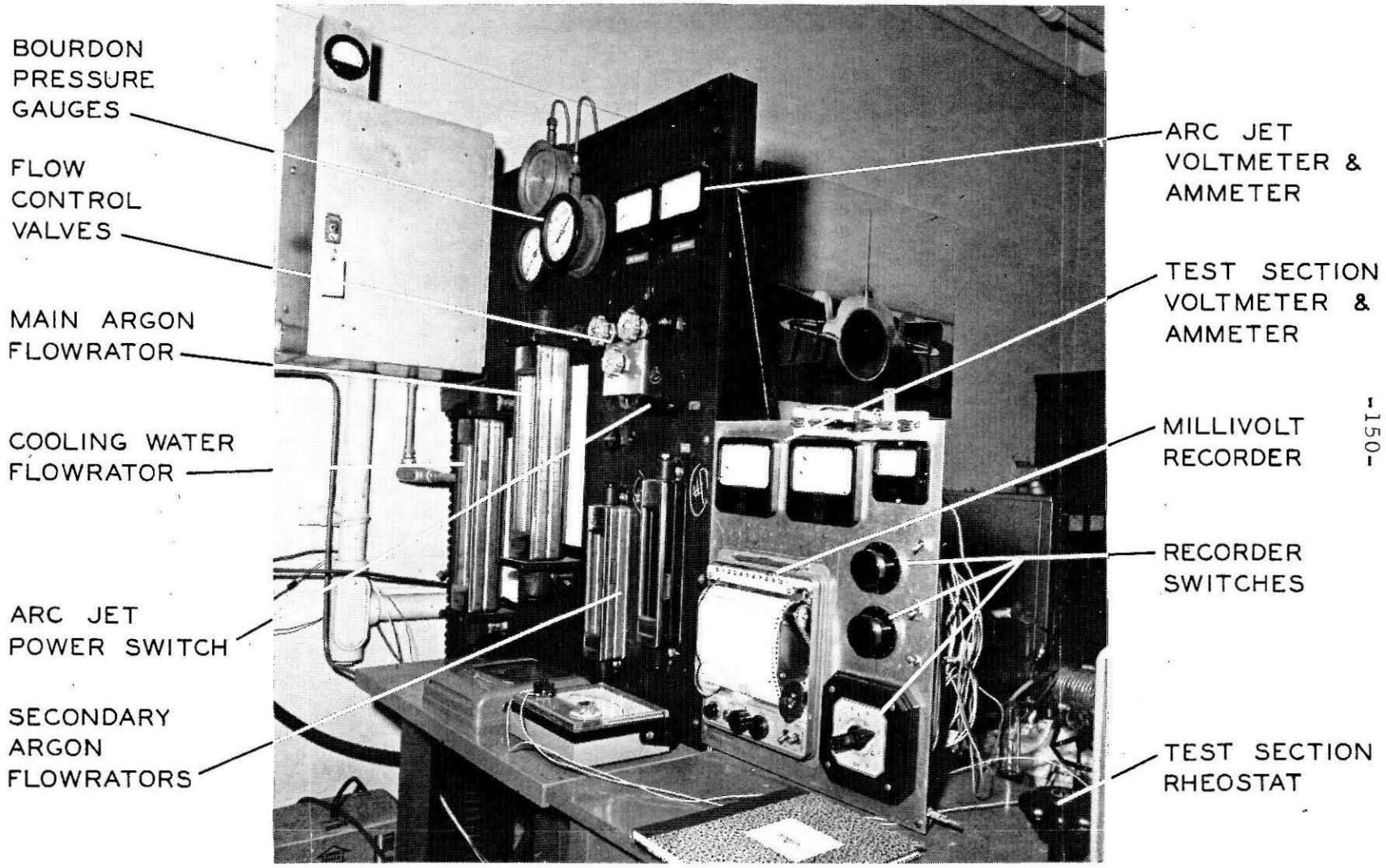

Figure 47. View of General Instrumentation and Control Panel.

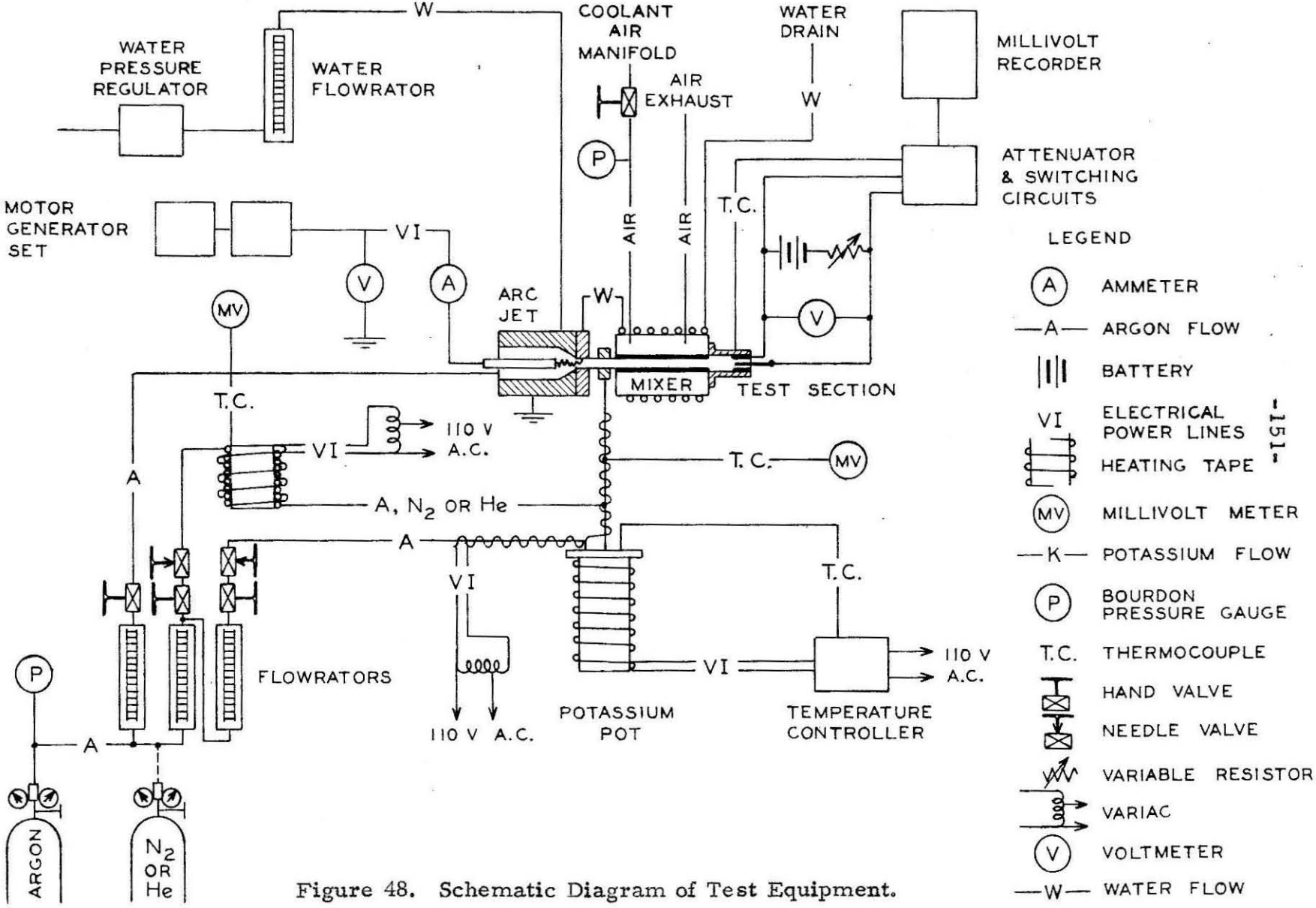

Figure 48. Schematic Diagram of Test Equipment.

a general exhaust system for the building, which served to remove the waste gases from the internal combustinn engine laboratory. At a distance of approximately $2\frac{1}{2}$' downstream from the exhaust tube entrance, a fine water spray was introduced into the stream. This water served both to react with the potassium in the gas stream and also to cool the gas and thus provide for more efficient removal of the exhaust products. With all components of this system working properly, no noticeable amounts of potassium were detected in the atmosphere around the test area.

A special argon heating system was installed for use with the conductivity maxima experiments. The total secondary argon flow which ordinarily passed through the potassium pot was divided into two parts, as shown in Fig. 48. Depending upon the amount of seeding material desired, a given flow rate of argon bubbled through the liquid potassium bath. The remainder of the argon was passed through a separate heating coil which was maintained at the same temperature as the potassium pot. This procedure resulted in a fixed value of the secondary argon flow rate independent of the seed concentration. Thus, a constant plasma temperature at the mixer exit was obtained. A simple calculation indicated that the amount of energy per unit volume associated with ionization of the seed atoms was negligible in comparison with the ordinary thermal energy of the argon atoms. Hence, the procedure described above does indeed produce a uniform temperature independent of the seed concentration.

Two different potassium containers were employed in this facility. The smaller pot was approximately 2" I. D. by $8\frac{1}{2}$" in length.

A maximum depth of $3\frac{1}{2}$ inches of liquid potassium was utilized in this pot. The stay time of the argon in passing through this container was 0.3 seconds under typical operating conditions. It was assumed that this stay time was sufficiently long to insure that the argon leaving the pot was completely saturated with the equilibrium potassium concentration.

A considerably larger pot of 4" I. D. by 16" length was also utilized. This increased size resulted in a stay time of 2.0 seconds. The experimental results obtained when this larger container was installed did not differ appreciably from the results obtained with the smaller pot. In addition, Mr. E. G. Gibson of the California Institute of Technology performed some simple experiments designed to directly measure the seed concentration of the flow passing through the potassium pot. The results of these experiments indicated that the measured seed concentration was within 90 per cent of the predicted value. Thus, both of the aforementioned observations supported the assumption of vapor equilibrium in the potassium pot.

The section of tubing from the potassium pot to the injection manifold was heated to a sufficiently high temperature to prevent condensation of the potassium out of the argon stream. Heating of the injection manifold which surrounded the mixing tube was accomplished by heat transfer from the main heated argon flow. As the injection manifold was usually operated with a visible glow, little evidence of potassium condensation was observed in this section. The walls of the mixing chamber were air cooled to permit them to achieve a sufficiently high running temperature. Thermocouples welded on the outer side of

the mixing tube indicated a temperature between 700 - 1000°C. In view of the above considerations, actual seed concentration of the gas in the test section should be quite accurately computed from the seed concentration at the exit of the potassium pot.

An experimental indication of potassium condensation in various parts of the apparatus was obtained by suddenly terminating flow through the potassium pot and simultaneously observing the rate of increase of the test section voltage as it approached the open circuit value. With the system properly operating, the test section became essentially non-conducting in a matter of a few seconds. This fast response indicated a very "clean" system, i.e., one in which very little potassium was condensed.

Instrumentation

A direct-current, panel-type volt meter (Simpson model 29) was employed to measure the voltage across the arc jet. The arc current was measured by means of a series shunt (150 amps - 50 mv) and indicated on a suitable DC millivolt meter (Simpson model 29).

Eight iron-constantan thermocouples, connected in series, were utilized to measure the temperature rise of the arc jet cooling water. The flow rate of the cooling water was indicated by a conventional flowrator (Fischer and Porter series 10A 2700). A flowrator of this same type was also used to measure the primary argon flow to the arc jet. These meters consisted of a rotating metal float within a tapered tube. The secondary argon flows were measured by a floating ball type rotameter (Fischer and Porter "Tri-Flat" series). Argon pressure upstream of the flowrators was determined by a Bourdon-type pressure

gauge (Ashcroft model 7234). The flowrators were calibrated by measuring the time required to displace a known volume of water.

Power to the potassium heating tapes ("Briskeat" type) was controlled by an automatic temperature regulator (Brown Instruments "Pyr-O-Vane"). A Conax thermocouple with an ungrounded junction and stainless steel sheath was immersed in the liquid potassium. This thermocouple actuated the temperature regulator.

A millivolt recorder (Varian Associates G-11A) was utilized, in conjunction with the external attenuator circuits and a Minneapolis-Honeywell thermocouple switch, to record the test section voltage and current and the various temperatures. The test section voltage and current were also monitored by DC panel meters (Simpson model 29). Thermocouple measurements were monitored by a direct-reading millivolt meter (Hewlett-Packard model 425A).

The sodium line reversal apparatus utilized the following equipment: two double convex lenses with a 20 cm focal length, a Gaertner 474-AV spectroscope, and a tungsten filament lamp (General Electric microscope illuminator 18A). A Superior type variac supplied the electrical power to the lamp, while a Simpson model 29 AC voltmeter measured the lamp voltage. All of the line reversal equipment was mounted on a specially designed and fabricated optical bench. This optical bench permitted rapid and precise adjustment of the optical system in all three directions.

The temperature of the outer electrode of the test section was measured by means of a chromel-alumel thermocouple. Temperature measurement of the inner electrode was accomplished by means of a conventional optical pyrometer (Leeds and Northrup model 8622-C).

REFERENCES

1. Kerrebrock, J. L., "Non-Equilibrium Effects of Conductivity and Electrode Heat Transfer on Ionized Gases," Technical Note No. 4, Guggenheim Jet Propulsion Center, California Institute of Technology. AFOSR 165 (November 1960).

2. Taylor, J. B. and Langmuir, I., "The Evaporation of Atoms, Ions, and Electrons from Caesium Films on Tungsten," Physical Review, Vol. XLIV, No. 6, pp. 423-458 (1933).

3. Killian, T. J., "Thermionic Phenomena Caused by Vapors of Rubidium and Potassium," Physical Review, Vol. XXVII, pp. 578-587 (1926).

4. Cobine, J. D., Gaseous Conductors, Dover, New York (1958), pp. 292-311.

5. Chapman, S. and Cowling, T. G., The Mathematical Theory of Non-Uniform Gases, Cambridge Press, Cambridge, Second Edition (1960).

6. Spitzer, L., Jr., Physics of Fully Ionized Gases, Interscience, New York (1956).

7. Kerrebrock, J. L., private communication.

8. Brown, S. C., Basic Data of Plasma Physics, Technology Press, Massachusetts Institute of Technology, and John Wiley and Sons, New York (1959).

9. Hurwitz, H., Jr., Sutton, G. W., and Tamor, S., "Electron Heating in Magnetohydrodynamic Power Generators," ARS Journal, Vol. 32, No. 8, pp. 1237-1243 (1962)

10. Robben, F. A., "Experimental Studies on Non-Equilibrium Ionization in a MHD Generator," Technical Report R62SD13, General Electric Space Sciences Laboratory (Feb. 1962).

11. Delcroix, J. L., Introduction to the Theory of Ionized Gases, Interscience, New York (1960).

12. Meghreblian, R. V. and Holmes, D. K., Reactor Analyses, McGraw-Hill, New York (1960).

13. Massey, H. W. S. and Burhop, E. H. S., Electronic and Ionic Impact Phenomena, Oxford Press, London (1956).

14. Leighton, R. B., Principles of Modern Physics, McGraw-Hill, New York (1959).

15. Jakob, M., Heat Transfer, Vol. II, John Wiley and Sons, New York (1957), pp. 20-24.

16. Jones, H. A. and Langmuir, I., "The Characteristics of Tungsten Filaments as Functions of Temperature," General Electric Review, Vol. 30, pp. 310, 354, 408 (1927).

17. McAdams, W. H., Heat Transmission, McGraw-Hill, New York (1954), p. 475.

18. Langmuir, I. and Taylor, J. B., "The Conductivity of Tungsten and the Cooling Effects of Leads upon Filaments at Low Temperatures," Physical Review, Vol. L, No. 1, p. 68 (1936).

19. Tolman, R. C., Principles of Statistical Mechanics, Oxford University Press, London (1938), p. 163.

20. Penner, S. S., Quantitative Molecular Spectroscopy and Gas Emissivities, Addison-Wesley, Reading (1959), pp. 17-25.

21. Bundy, F. P. and Strong, H. M., "Measurement of Flame Temperature, Pressure, and Velocity," Vol. IV. High Speed Aerodynamics and Jet Propulsion, Physical Measurements in Gas Dynamics and Combustion, Princeton (1954), pp. 343-364.

22. Mitchell, A. C. G. and Zemansky, M. K., Resonance Radiation and Excited Atoms, The University Press, Cambridge (1934), p. 59 ff.

23. Morse, P. M. and Feshbach, H., Methods of Theoretical Physics, McGraw-Hill, New York (1953), pp. 434-443.